Modeling and Enhancing Transient Stability of Grid-forming Converters

Ali Arjomandi Nezhad

Imperial College London

Department of Electrical and Electronics Engineering

Control and Power Research Group

May 2025

This thesis is submitted in partial fulfilment of requirements

for the degree of Doctor of Philosophy

Dedicated to
my parents

Statement of Originality

I hereby declare that all the work in this thesis is my own. The work of others has been properly acknowledged

Ali Arjomandi Nezhad

May 2025

Declaration of Copyright

The copyright of this thesis rests with the author. Unless otherwise indicated, its contents are licensed under a Creative Commons Attribution-NonCommercial 4.0 International Licence (CC BY-NC).

Under this licence, you may copy and redistribute the material in any medium or format. You may also create and distribute modified versions of the work. This is on the condition that: you credit the author and do not use it, or any derivative works, for a commercial purpose.

When reusing or sharing this work, ensure you make the licence terms clear to others by naming the licence and linking to the licence text. Where a work has been adapted, you should indicate that the work has been changed and describe those changes.

Please seek permission from the copyright holder for uses of this work that are not included in this licence or permitted under UK Copyright Law.

Abstract

Grid-forming (GFM) Inverter-based resources (IBRs) are suggested to be deployed in power grids as a response to the emerging needs in IBR-dominant power systems. Their software-defined dynamic characteristics are constrained by several limitations, such as the limitations in electric current output. GFM IBRs might enter the current-saturation operation mode facing a severe disturbance. Operating in the current-saturation operation mode causes a distinct behaviour from their normal operation mode. This thesis aims at modelling and enhancing the transient stability of GFM IBRs considering the current saturation.

In the modelling phase, the conditions for transitioning between the normal and current-saturation operation modes are identified. Based on these conditions, the large-signal model for the transient stability of GFM IBRs is developed. It is observed that the angle of the saturated current plays a prominent role in shaping the post-disturbance dynamics of GFM IBRs. Then, the circumstances under which the GFM IBR converges to the saturated stable equilibrium point (satSEP), which is an emerging challenge due to the current saturation, are explored. It is also demonstrated that the current saturation causes a decrease in the post-fault deceleration area of the equal area criterion.

In the enhancing phase, two main challenges, which are mentioned in the modelling phase, are compensated: (1) The possibility of convergence to the satSEP is mitigated by tuning the angle of the saturated current to satisfy the sufficient condition for avoiding the convergence, (2) The decreased post-fault deceleration is compensated by adding two corrective signals to the active power controller (APC). These corrective signals are evaluated through a model predictive control (MPC), which aims to minimize the deviations of the APC angle from the stable equilibrium point, subject to a safe post-fault trajectory. The modelling and enhancement measures are verified by several electromagnetic transients (EMT) simulation case studies in Simulink/MATLAB environments.

Acknowledgements

I wish to express my appreciation to Prof. Bikash C. Pal for his continuous support and guidance. I would also like to thank Dr. Yifei Guo for providing me with his expert advice. I would also like to thank Prof. Damiano Varagnolo, Dr. Guangya Yang, and Dr. Dusan Majstorovic for their mentorship during my visits at the Norwegian University of Science and Technology, Technical University of Denmark, and Tajfun HIL company, respectively.

I thank my colleagues and friends at Imperial College London for helping to create a positive and memorable work environment. Many of them shall be mentioned here, but to keep this paragraph short, I thank them collectively. I would also like to thank Reza for being a great friend and neighbour throughout these years. My gratitude also goes to the early-stage researchers of the InnoCyPES project for the memorable moments shared during the training schools.

I want to express my deepest gratitude to my family—my father, Mohammad Reza Arjomandi Nezhad; my mother, Mina Matoo, and my sister, Termeh (Fatemeh) Arjomandi Nezhad—whose unconditional love and support are the most precious gifts in my life.

Finally, I acknowledge the InnoCyPES European Unions Horizon 2020 Research and Innovation Programme under the Marie Skodowska-Curie Grant 956433 for funding my research.

Contents

Statement of Originality ii

Declaration of Copyright iii

Abstract 1

Acknowledgements 2

List of Figures 6

List of Tables 9

1 Introduction 15
- 1.1 Background . . . 16
- 1.2 Literature Review . . . 17
  - 1.2.1 Transient Stability Assessment and Enhancement . . . 17
  - 1.2.2 Grid-forming Converters Transient Stability Assessment . . . 19
  - 1.2.3 Tuning the Angle of the Magnitude-Saturated Current . . . 21
  - 1.2.4 Grid-forming Converters Transient Stability Enhancement . . . 21
  - 1.2.5 Gaps in knowledge . . . 23
- 1.3 Thesis Objectives and Contributions . . . 24
- 1.4 Research Dissemination . . . 25
  - 1.4.1 Publications . . . 25
  - 1.4.2 Presentation . . . 25
- 1.5 Organization of the Thesis . . . 26

2 A Review on Grid Following and Grid-Forming Inverter-based Resources 27
- 2.1 A brief introduction to grid-following and grid-forming IBRs . . . 27
  - 2.1.1 Grid-following IBRs . . . 28
  - 2.1.2 Services required in IBR-dominant power systems . . . 28
  - 2.1.3 Grid-forming IBRs . . . 30
- 2.2 Control structure of grid-following and grid-forming IBRs . . . 31
  - 2.2.1 Preliminary: dq-frame transformation . . . 31

2.2.2 Control structure of grid-following inverter-based resources 34
2.2.3 Control structure of grid-forming inverter-based resources 36
2.3 Current Limitation Mechanisms 38
2.3.1 Current Reference Saturation 39
2.3.2 Virtual Impedance 42

3 Modelling Transient Stability of Grid-Forming Converters Considering Current Saturation 43
3.1 Synchronism and Transient Stability Definition 44
3.2 Synchronism of Grid-Forming Inverter-based Resources 44
3.3 Modelling GFM IBR in the current-saturation operation mode 47
3.3.1 Transiting to the current-saturation mode 49
3.3.2 Conditions for returning to the normal operation mode 54
3.3.3 Sensitivity analyses of the set of returning angles 58
3.4 Effect of Current Saturation on Transient Stability 63
3.5 Circumstances of Converging into Saturated Stable Equilibrium Point . . . 67
3.6 Results and Discussions 70
3.6.1 Effect of the angle of the saturated current 72
3.6.2 Convergence to satSEP through $\mathcal{C}_2$ 74
3.6.3 Shrink in stability DOA due to current saturation 78
3.6.4 Effect of the voltage controller limiter 79
3.6.5 Oscillations between normal and current-saturation modes 81
3.7 Chapter Summary 82

4 Optimal Angle of the Saturated Current for Avoiding Convergence to the Saturated Stable Equilibrium Point 84
4.1 Effect of Voltage Control Loop Error on Output Power 86
4.2 Voltage Transient After Transiting to the Normal Operation Mode 88
4.3 Optimization Formulation 89
4.4 Results and discussions 93
4.5 Chapter Summary 98

5 A Model Predictive Control for Enhancing Transient Stability of Grid-Forming Converter 100
5.1 Benchmark Methods in Transient Stability Enhancement 101
5.2 Structure and Formulation of the Proposed Model Predictive Control 103
5.2.1 Optimization Formulation 105
5.3 Stability Boundary of a GFM IBR equipped with the Proposed MPC . . . 108
5.4 Results and Discussions 109
5.4.1 Tests Under the Strong Grid Condition 110
5.4.2 Sensitivity Analyses 114
5.4.3 Robustness to Parameter Estimation Error 116
5.5 Chapter Summary 116

6 Conclusions and Future Work 117

6.1 Conclusions 117
6.2 Future Work 119

Bibliography **121**

List of Figures

2.1 An elementary series RL branch. 32
2.2 An elementary shunt capacitor branch. 33
2.3 The general control structure of a PLL. 34
2.4 The control structure of a GFL IBR. 35
2.5 The control diagram of the decoupled current control with feedforward terms. 35
2.6 The equivalent block diagram of the current control loop alongside d and q directions. 36
2.7 The general structure of a multi-layer VSG GFM IBR. 37
2.8 The control diagram of the decoupled voltage control with feedforward terms. 38
2.9 The equivalent model of voltage control loop alongside d and q directions. . 38
2.10 A visual comparison of the most popular current reference saturation methods. 40
2.11 The block diagram implementation of the virtual impedance 42

3.1 The GFM IBR's terminal voltage and grid Thevenin voltage phasor diagram in the steady-state normal operation mode. 45
3.2 The active power control closed-loop schematics. 45
3.3 Phasor-Diagram of the voltages in (a) steady-state normal operation mode, (b) a severe voltage drop situation in the absence of current limitation, (c) a large APC angle (δ) situation in the absence of current limitation, and (d) a large APC angle with constant angle current reference saturation. . . 46
3.4 The changes in the equilibrium point of the voltage controller due to minor changes in the voltage reference. 47
3.5 The changes in the equilibrium point of the voltage controller due to a severe voltage sag. 48
3.6 The changes in the equilibrium point of the voltage controller due to a large APC angle. 48
3.7 The variations of the saturation threshold angle with grid Thevenin voltage for different values of the grid total impedance. 50
3.8 The voltage variation with the APC angle (δ) for different angles of the saturated current (β). 51
3.9 Active and reactive power output variations with $\delta + \beta$. 52
3.10 Active and reactive power output variations with the APC angle. 53
3.11 The sets of entering and returning angles if $Z = 0.46$ p.u. and $X/R = \infty$. . 57
3.12 The variation of sets of entering and returning angles for $\beta = -10°$. 59
3.13 The variation of sets of entering and returning angles for $\beta = -30°$. 60
3.14 The variation of sets of entering and returning angles for $\beta = -60°$. 60

3.15 The set of entering and returning angles demonstrated as the solid filled and hatched area for $\beta' = 5°$. 62
3.16 The set of entering and returning angles demonstrated as the solid filled and hatched area for $u_{\max} = I_s^{\max}$, i.e., $\beta' = 45°$. 63
3.17 Power-angle curves in the normal operation mode or the current-saturation mode. 64
3.18 A visual demonstration of the position of the singular point with respect to the power-angle curve. 65
3.19 Deceleration area for the saturated power-angle curve and unsaturated power-angle curve. 67
3.20 An example of convergence to the satSEP through $\mathcal{C}_1$. 68
3.21 An example of convergence to the satSEP through $\mathcal{C}_2$. 70
3.22 Simulation results for the currents in Cases A, B, and C. 73
3.23 Simulation results for the angles in Cases A, B, and C. 74
3.24 Simulation results for the angles in Cases D and E. 75
3.25 The currents in Cases D and E. 76
3.26 Post-fault trajectories of the GFM IBR in Cases D and E where the solid area and hashed area correspond to the set of entering and returning angles, respectively. 76
3.27 Post-disturbance trajectories in Cases F, G, and H. Black line and brown line are the borders of DOAs for a GFM equipped and not equipped with CRS; respectively. 77
3.28 Trajectory of Case G until convergence to the next SEP after passing the positive unstable equilibrium point. 77
3.29 Post-fault active power in Case G. 78
3.30 Post-disturbance current of the GFM IBR in Cases F, G, and H. 78
3.31 Output current in Cases I and J. 79
3.32 APC angle, output power, and the terminal voltage in Cases I and J. 80
3.33 The post-fault APC trajectories in Cases I and J. 81
3.34 (a) The original CACRS (without oscillation mitigation) and (b) oscillation mitigated CACRS proposed in Subsection 3.3.2.1. 82

4.1 Numerically calculated set of angles of saturated current for which $\delta_s^{SE}(\beta) \in \mathcal{R}(\beta) - \mathcal{S}$ (green) and $\delta_s^{SE}(\beta) \notin \mathcal{R}(\beta) - \mathcal{S}$ (blue) for different values of the total impedance. 85
4.2 Numerically calculated set of angles of saturated current for which $\delta_s^{SE}(\beta) \in \mathcal{R}(\beta) - \mathcal{S}$ (green) and $\delta_s^{SE}(\beta) \notin \mathcal{R}(\beta) - \mathcal{S}$ (blue) for different power references. 85
4.3 The GFM IBR's terminal voltage and grid Thevenin voltage phasor diagram in normal operation mode in the presence of the voltage control loop error. 87
4.4 The equivalent block diagram of the APC loop including voltage-error induced power oscillation as disturbance. 87
4.5 The equivalent block diagram of the voltage control loop, neglecting the dynamics of the current control loop [1]. 89
4.6 The variation of the initial transiting voltage error with the angle of the saturated current for different values of grid impedance ($Z_1 < Z_2 < Z_3$). . . 89

4.7 Post-fault trajectories in cases A, B, and C. 93
4.8 The APC angle for which the GFM IBR converges to SEP (green), converges to satSEP (blue), or becomes unstable (red) for different values of β in scenario 1. 94
4.9 Post-fault currents in cases A, B, and C. 95
4.10 Terminal voltage of the GFM IBR after returning to the normal operation mode in cases A and B. 96
4.11 Active power output of the GFM IBR after returning to the normal operation mode in cases A and B. 96
4.12 Post-fault trajectories in cases D, E, and F. 97
4.13 The APC angle for which the GFM IBR converges to SEP (green), converges to satSEP (blue), or becomes unstable (red) for different values of β in scenario 2. 97
4.14 Post-fault currents in cases D, E, and F. 98
4.15 Terminal voltage of the GFM IBR after returning to the normal operation mode in cases D and F. 99

5.1 Fault-on trajectories of a GFM IBR (a) equipped and (b) not equipped with frequency bounding if $X = 0.46$ p.u. The blue line is the border of the DOA. 103
5.2 The general structure of VSG GFM IBRs [2, 3, 4] added with an MPC module to enhance the transient stability. 104
5.3 The numerically calculated boundary of DOA if the CL_0 is implemented for different values of maximum corrective active power reference change. Black dashed lines are post-fault trajectories in the absence of any corrective control in case of connection to a grid with $X = 0.46$ p.u. 109
5.4 APC angle and frequency transient for different control strategies in the case of connection to the strong grid ($Z_g = 0.3$ p.u.). 111
5.5 The optimal values for the corrective control law for the scenario where the GFM IBR is connected to the strong grid. 112
5.6 APC angle and frequency transient for different control strategies in the case of connection to the weak grid ($Z_g = 0.9$ p.u.). 113
5.7 The optimal values for the corrective control law for the weak grid-connected GFM simulation. 114
5.8 Variations of the CCT with the Thevenin's voltage for a GFM IBR connected to a strong grid ($Z_g = 0.3$ p.u.) 115
5.9 Variation of the CCT with the active power reference for a GFM IBR connected to a grid with $Z_g = 0.4$ p.u. 115
5.10 Post-fault APC angles for the proposed MPC with 10 % of impedance error. 116

List of Tables

3.1 The sets of β satisfying (3.21) 56
3.2 The condition for returning to the normal operation mode with a considerable value of $u_{\max}$ 61
3.3 Parameters of the simulated GFM farm. 72
3.4 The list of simulated cases. Fields in bold are the parameters that vary in each comparison set. 72

4.1 Parameters of the simulated GFM farm. 93

5.1 Parameters describing the simulated GFM IBR farm. 110

Nomenclature

α	$\arctan \frac{R}{X}$
β	Angle of the saturated current
β_v	The angle of the saturated current for which the voltage deviation from the reference is minimized upon returning to the normal operation mode
$\beta_{\max}$	The maximum allowable angle of the saturated current
$\beta_{\min}$	The minimum allowable angle of the saturated current
$\Delta\delta_c$	Corrective angle jump
$\Delta\delta_c^{\max}$	Maximum corrective angle jump
ΔP_{ref}	Corrective active power reference change
$\Delta P_{ref}^{\max}$	Maximum corrective active power reference change
ΔV_d^0	The initial voltage error alongside the d-axis upon returning to the normal operation mode
ΔV_q^0	The initial voltage error alongside the q-axis upon returning to the normal operation mode
δ	APC angle $(\theta - \theta_g)$
δ_d^p	The maximum angle for which $V_d^{\text{sat}} \leq V_d$
δ_q^q	The minimum angle for which $0 \leq V_q^{\text{sat}}$
δ_{ZC}^{sat}	The APC angle after which the active power output becomes negative in the current-saturation mode

δ^{SE}	Angle of the stable equilibrium point
$\delta_{\mathrm{s}}^{\mathrm{SE}}$	Angle of the saturated stable equilibrium point
δ_1^{UE}	Angle of the positive unstable equilibrium point
δ_2^{UE}	Angle of the negative unstable equilibrium point
δ_r	The APC angle at which the GFM IBR returns to the normal operation mode
δ_u	The maximum angle of the set $\mathcal{R}$
δ_{sat}	Threshold angle of entering to the current saturation mode
ϵ	The deviation of the angle of the satSEP from $\overline{\mathcal{S}}$
η_1	The deviation of the angle of the satSEP from $\mathcal{R}$ if $-45^\circ \leq \beta \leq 0^\circ$
η_2	The deviation of the angle of the satSEP from $\mathcal{R}$ if $-90^\circ \leq \beta \leq -45^\circ$
$\mathcal{D}$	Set of the decision variables of the Proposed
$\mathcal{G}$	Set of the constraints of the Proposed
$\mathcal{R}$	Set of the returning angles
$\mathcal{S}$	Set of the entering angles
ω	Per unit frequency of APC
ω_0	Reference per unit frequency
ω_n	Nominal frequency
$\omega_{\max}$	Maximum APC frequency
$\omega_{\min}$	Minimum APC frequency
ϕ	Total Impedance angle from PCC ($\arctan \frac{X}{R}$)
ρ_1	Margin for the inclusion of the angle of the satSEP inside $\overline{\mathcal{S}}$
ρ_2	Margin for the inclusion of the angle of the satSEP inside $\mathcal{R}$
θ	Angle of the local reference frame
θ_g	Angle of the common reference frame

a_1	The binary variable which is zero if $-45^\circ \leq \beta \leq 0^\circ$
a_2	The binary variable which is zero if $-90^\circ \leq \beta \leq -45^\circ$
a_3	The binary variable which is zero if $\delta_u \leq \delta_{\text{sat}}$
a_4	The binary variable which is zero if $\delta_{\text{sat}} \leq \delta_u$
C	LC filter's capacitance
D_P	Active power droop coefficient
D_Q	Reactive power droop coefficient
H	Virtual inertia
i	Current injected to the grid
i_d	Current injected to the grid alongside d-axis of local reference frame
i_q	Current injected to the grid alongside q-axis of local reference frame
i_s	Inverter current output
$I_s^{\max}$	Maximum inverter current output
i_{sd}	Inverter current output alongside d-axis of local reference frame
i_{sd}^{ref}	Reference inverter current output alongside d-axis of local reference frame
i_{sq}	Inverter current output alongside q-axis of local reference frame
i_{sq}^{ref}	Reference inverter current output alongside q-axis of local reference frame
K	The big parameter penalizing the deviations of the angle of satSEP from $\mathcal{R} - \mathcal{S}$
K_Q	RPC control gain
L_f	LC filter's inductance
$m_{abc}(t)$	Pulse Width Modulation Reference
$n(k)$	The binary variable associated with the k^{th} discrete step which is 0 if the GFM IBR is in the current-saturation mode and 1 otherwise

P	Active power output
P_0	Active power output reference
P_{sat}	Active power output during the current-saturation mode
P_{unsat}	Active power output during the normal operation mode
Q	Reactive power output
Q_0	Reactive power reference output
R	Total resistance from PCC
R_g	Thevenin grid resistance
R_{tr}	Transformer resistance
S_b	Nominal apparent power
T	MPC optimization horizon
T_d	Discrete time step duration for MPC
u_{d}	Output of the PI controller of the d-axis voltage controller
u_{max}	Maximum output of the PI controller of the voltage controller
u_{q}	Output of the PI controller of the q-axis voltage controller
V	GFM IBR's terminal voltage
V_0	Terminal reference voltage
V_b	Nominal Voltage
V_d	Terminal voltage alongside d-axis of local reference frame
V_d^{ref}	Reference terminal voltage alongside d-axis of local reference frame
V_d^{sat}	Terminal voltage alongside d-axis of local reference frame in the current-saturation mode
V_q	Terminal voltage alongside q-axis of local reference frame
V_q^{sat}	Terminal voltage alongside q-axis of local reference frame in the current-saturation mode

V_{dc}	DC link voltage
V_g	Thevenin grid voltage
X	Total reactance from PCC
X_g	Thevenin grid reactance
X_{tr}	Transformer reactance
y	Shunt impedance of LC filter
Z	Total impedance from PCC
APC	Active Power Controller
DOA	Domain of Attraction
GFL	Grid-following
GFM	Grid-forming
IBR	Inverter-based Resource
MPC	Model Predictive Control
PCC	Point of Common Coupling
PLL	Phase Locked Loop
PWM	Pulse Width Modulation
RPC	Reactive Power Controller
$satSEP$	Saturated Stable Equilibrium Point
SCR	Short Circuit Ratio
SEP	Stable Equilibrium Point
SG	Synchronous Generator
UEP	Unstable Equilibrium Point
VSC	Voltage Source Converter

Chapter 1

Introduction

Due to environmental concerns, governments outlined their proposed solutions to reduce greenhouse gas emissions. The UK government announced its decarbonization strategy to meet the net-zero energy system goal by 2050 [5]. The Danish government also targets carbon neutrality by 2050 [6]. The national low-carbon strategy (SNBC) roadmap in France [7], the climate action plan 2050 by Germany [8], and the national climate agreement in the Netherlands [9] are other examples of governments' policies for eliminating/reducing carbon dioxide emissions. One of the pillar principles of decarbonization is the replacement of fossil fuel-based energy resources with renewable energy resources. A considerable percentage of these renewable energy resources are interfaced with the grid through power electronic inverters. Therefore, inverter-based resources (IBRs) are gradually replacing synchronous generators (SGs), the dominant interface in power systems.

Traditionally, SGs, which act as voltage sources, provide the grid with several services, e.g., frequency control, voltage control, inertia, and stabilizing. However, IBRs have been designed to act as current sources and have a limited contribution to services required by power systems. Therefore, researchers suggested redesigning the control structure of a percentage of installed IBRs to compensate for this requirement. This new control structure is named grid-forming (GFM) and aims at providing the grid with several services, including [10]:

- Voltage control
- Frequency control
- System strength improvement

- Virtual inertia
- Black-start capability

A GFM IBR provides the grid with the mentioned services. Hence, it contributes to the secure operation of power systems with high penetration of IBRs. Since there is limited practical experience with GFM IBRs, their dynamics in response to severe disturbances should be studied in detail to avoid unforeseen operational risks. This thesis, in particular, focuses on the transient angle stability of GFM IBRs, considering the effect of their current limiters. In the following sections, the main challenges and opportunities associated with the transient [angle] stability of grid-forming converters are discussed. Then, a literature review on transient stability analysis methods for traditional power systems is provided. After that, the literature on GFM IBRs' transient stability assessment and enhancement methods is reviewed. This is followed by introducing the main aims and contributions of the thesis. Finally, the structure of the thesis is outlined in this chapter.

1.1 Background

Power systems are always exposed to disturbances. Their stability, in general, is defined as the ability of a power system to settle in an operating equilibrium after being exposed to a disturbance, subject to most system variables bounded in a safe range [11]. It is often classified into three categories of short-term, mid-term, and long-term stability, based on the dynamic response bandwidth of the components and controllers leading to the stability problems. Furthermore, it is classified into the following categories depending on the associated variables and phenomena that play the dominant role in retaining stability [11]:

- Rotor angle stability
- Voltage stability
- Frequency stability
- Resonance stability
- Converter-driven stability

One of the most important categories is rotor angle stability, which is the ability of the system to keep the rotors of synchronous generators synchronous with each other. It further

divides into small-signal stability and transient stability, which correspond to the rotor angle stability when it is exposed to small-signal disturbances and severe disturbances, respectively.

The advent of IBR challenged the formal definition and classification of rotor angle stability. While these resources should retain synchronism with other resources, including SGs and other IBRs, they do not have any synchronously rotating parts. Their synchronous framework is generated inside their controller. Therefore, a more comprehensive framework extends the definition of rotor angle stability to *angle stability*. The term angle stability encompasses the synchronism of power systems that include both SGs and IBRs or either of them.

This thesis, in particular, studies the transient angle stability of GFM IBRs equipped with constant-angle current saturation as their current limiter In the following section, a literature review of the relevant research is presented.

1.2 Literature Review

In this section, the methods for transient stability studies for traditional power systems are reviewed first. Then, GFM IBRs' transient stability assessment and enhancement methods are discussed. Finally, this section is concluded by mentioning the related gaps in knowledge.

1.2.1 Transient Stability Assessment and Enhancement

There is a rich literature on transient stability assessment and enhancement for several decades. The equal area criterion has been used for transient stability assessment of a single SG connected to a transmission line [12]. According to this method, if the post-disturbance deceleration of the rotor angle is more than its acceleration during the disturbance, the SG keeps its synchronism with the grid. Even though this method provides insights into the concept of transient stability, it might lack enough accuracy to check the ability of a multi-machine power system to retain synchronism.

Extended equal area criterion was proposed in [13] to solve the problem for a multi-machine system. It divides the machines into two clusters of critical machine(s) and the remaining of the system. It models each cluster as a machine. Finally, the system is reduced to the equivalent one-machine-equivalent-system. This method is only suitable for SG-based

power systems [14]. Hence, this method is not suitable for modern power systems with high penetration of IBRs.

The time-domain simulation method is a more general approach, which relies on numerical simulation after modelling the dynamics of the system [15]. Although the time-domain simulation is more accurate than other assessment methods, it is computationally expensive for big grids, which contain many interacting resources [16].

Several papers developed Lyapunov-based methods [17], aka direct methods, as a fast domain of attraction (DOA) estimation method. However, the estimated DOA is conservative [16]. An adaptive Lyapunov method was proposed in [18] to extend the estimated border closer to the actual border. An expansion algorithm based on Runge-Kutta was proposed in [19] to improve transient stability boundary estimation. Most of the direct methods in the literature calculate the Lyapunov function based on the synchronous machines' model. Therefore, the same issue mentioned for the extended equal area criterion is a disadvantage of the direct methods. As the model becomes more detailed, a new Lyapunov function should be found. For example, reference [20] found a Lyapunov function suitable for the SG model with bounded control laws. For complex systems containing heterogeneous generation-side technologies, finding a new Lyapunov function that satisfies the Lyapunov conditions while not being too conservative becomes more challenging. For example, reference [21] utilized the gravitational search meta-heuristic algorithm for finding an appropriate Lyapunov function for an AC/DC system containing wind power generation.

Machine Learning-based transient stability assessment methods have been proposed in the literature to be as general as the time-domain simulation while being fast enough [22]. To realize this aim, a Machine Learning-based model is trained with a huge dataset of offline time-domain simulations. Then, the model is used in the online transient stability assessment. The growing number of online wide-area measurement installations made it feasible to use Machine Learning-based methods. However, the accuracy of these methods highly relies on the fidelity of the training dataset. The fidelity of the training dataset is challenged in the following circumstances:

- Network reconfiguration or expansion
- Unforeseen operation scenarios
- Increasing penetration of resources with new technologies

Therefore, a detailed analytical transient stability study is required. This thesis focuses on the transient stability of grid-forming converters equipped with constant-angle current reference saturation.

1.2.2 Grid-forming Converters Transient Stability Assessment

Transient stability of GFM IBRs is defined as their ability to retain their synchronism with the grid after facing a severe disturbance [4]. This is mainly related to the frequency and angle of the local reference frame generated by the active power controller (APC). Therefore, the transient stability of GFM IBRs is indeed the stability of the angle and frequency of their APC around its stable equilibrium point (SEP) [23]. References [24, 25] adopted direct methods for finding the transient stability boundaries. A Lyapunov function for encompassing the effect of changing the control parameters on transient stability was presented in [26]. The angle trajectory of GFM IBRs was modelled with Krylov Bogoliubov Mitropolsky (KBM) asymptotic method in [27]. Authors in [28] derived quantitative stability conditions for GFM IBRs with complex droop control. A method for adding the visualization of the damping coefficient to the traditional equal area visualization was presented in [29]. None of these papers considered the impact of the current limitation on the transient stability of GFM IBRs. IBRs have a limited overcurrent capacity between 1.1 and 1.4 per unit unless they are over-designed [30]. This limitation is easily hit when they face severe disturbances. Therefore, the GFM IBRs enter the current saturation mode, which endangers the transient stability [31].

Current limitation mechanisms cluster into two main groups [32]: *a*) current reference saturation (CRS) and *b*) virtual impedance (VI). The CRS-based methods directly saturate the current reference generated by the voltage controller of the GFM IBR. It causes the deactivation of the current reference generated by the voltage controller. Therefore, the GFM IBR operates as a current source. The main difference between a GFM IBR in the current source mode and a grid-following (GFL) IBR is that GFM IBR still synchronizes itself to the grid through APC. However, a GFL IBR is a current source that synchronizes itself to the grid through a phase-locked loop (PLL). The VI-based methods limit the current by emulating a sufficiently large impedance behind the voltage reference. Therefore, the GFM IBR keeps operating as a voltage source if the current is limited through a VI-based method. However, the current limitation functionality of the VI-based method is usually delayed by a few milliseconds [32, 33]. This delay might impose the risk of overheating to the inverter. Therefore, this thesis limits its scope to CRS. The respected readers are

referred to [34, 35, 36, 37] for the transient stability study of GFM IBRs equipped with the VI-based current limitation mechanisms.

The CRS-based methods have different variants depending on how the angle of the saturated current reference is set when the magnitude of the current reference exceeds its threshold. Some of the most important variants are Circular CRS, d-axis priority CRS, q-axis priority CRS, and constant angle CRS (CACRS). Circular CRS saturates the magnitude of the reference current to the maximum value and keeps the angle of the unsaturated current reference as the angle of the saturated current. The application of this type of current limiter is usually limited to cases where the voltage controller is a virtual admittance [38]. d-axis priority CRS and q-axis priority CRS allow the magnitude reference component alongside the prioritized axis to change up to the limitation, and the other axis is limited to the remaining capacity [39, 40]. CACRS fixes the angle of the magnitude-saturated current to a constant angle from the local reference frame [41].

There is no standard consensus on what type of current limiters method should be implemented for GFM IBRs yet. Therefore, the dynamics of GFM IBRs for all types of current limiters should be studied in detail before deciding on implementing one of those. The flexibility to tune the angle of the saturated current in CACRS provides the opportunity to enhance the stability margins of GFM IBRs. Therefore, this thesis limits its focus on the transient stability study of GFM IBRs equipped with CACRS. Transient stability of GFM IBRs equipped with other current limitation mechanisms is analysed in [31, 38, 42, 43, 44].

The power-angle characteristic of virtual synchronous generator (VSG) GFM IBRs for three types of current limiters, i.e. CACRS, d-axis priority CRS, q-axis priority CRS, was formulated [45]. Authors in [46] showed that when GFM IBRs enter the current saturation mode, their power-angle characteristic significantly changes. Then, they proposed multiple Lyapunov functions for each characteristic to investigate transient stability. Transient stability of VSG GFM IBRs with CACRS current limitation mechanism was assessed using a segmental equal area criterion in [47]. Authors in [48] adopted a Lyapunov-based method for this purpose. References [47, 48, 49] showed that there is a possibility of convergence to a saturated stable equilibrium point (satSEP) in addition to converging to the SEP and instability possibilities. If the GFM IBR converges to the satSEP, it locks into the current-saturation mode. This is an undesired possibility because the GFM IBR does not act as a voltage source for which it is designed. Authors in [49] discussed that if the angle of the satSEP is more than a saturation threshold angle, the GFM IBR might converge to the satSEP. It will be shown in Chapter 3 that another circumstance in which a GFM IBR converges to satSEP exists. In order to explore the circumstances in which GFM

IBRs' post-disturbance trajectory converges into the satSEP, it is necessary to identify the conditions for transition to/from the current-saturation mode. It is discussed in [50] that these conditions can be expressed as the inclusion of the APC angle (the angle between the local reference frame and common reference frame) in some specific sets. These sets are named the *set of entering angles* and the *set of returning angles* in this thesis. Authors in [50] also discussed that these two sets do not always complement each other, and if the APC angle is inside the intersection of these two sets, the GFM IBR oscillates between the normal operation mode and the current-saturation operation mode. Several papers in the literature presented expressions for the set of entering angles, for example, [47]. However, an analytical expression for the set of returning angles has been missed.

1.2.3 Tuning the Angle of the Magnitude-Saturated Current

While there is limited freedom for the selecting of the magnitude of the saturated current, it is possible to modify the angle of the saturated current for enhanced disturbances ride-through and recovery. This angle has a considerable effect on the transient stability of grid-forming converters [48]. A Lyapunov-based method was presented in [51] to tune the angle of the saturated current to increase the chance of transient angle stability during a short-circuit fault. More specifically, this angle is tuned to increase the chance that the APC angle converges into the SEP.

It is also critical to prevent the APC angle from converging to the satSEP after clearing the fault. Authors in [49] claimed that if the angle of the saturated current is more than a lower threshold, the APC angle does not converge to the satSEP. This claim is revisited in Chapter 3. Based on the analyses of Chapter 3, the need for a new tuning algorithm to prevent convergence to satSEP is identified, which will be addressed later in Chapter 4.

1.2.4 Grid-forming Converters Transient Stability Enhancement

In transient stability management, not only are transient stability modelling and assessment important, but also transient stability enhancement is crucial, especially if transient instability is highly likely to occur. Many papers in the literature have attempted to enhance the transient stability of GFM IBRs. Reference [52] proposed a variable virtual inertia for PV-based VSM to enhance the transient stability of the grid. Letter [53] developed a Lyapunov-based method for tuning the APC parameters to comply with the transient stability requirement. An adaptive method for damping coefficient and virtual

inertia parametrization was proposed in [54] to enhance the transient stability of grid-forming converters. Dynamic damping control was proposed in [55] to provide the APC with extra damping when an under-voltage is detected. Similarly, [56] suggested increasing the damping coefficient upon detecting a fault.

Adding an auxiliary inertia term to the APC structure was developed in [57] for enhancing transient stability of VSG GFM IBRs. A transient damping term was introduced to APC in [58] to provide extra damping after a severe disturbance. This method requires a PLL (voltage-synchronized control loop) in addition to the power-synchronized APC. The transient damping term was optimized in [59, 60] for an optimal enhanced transient stability. Authors in [61] proposed that a hybrid synchronization of a GFM IBR containing both APC and PLL can enhance transient stability. This was followed by the adaptive hybrid weighting coefficient for optimal transient stability in [62]. Reference [63] designed a more specific hybrid synchronization method for doubly fed induction generator-based wind generation.

Authors in [4] limited the control signals of the APC to keep the APC state variables inside the DOA. Reversing the sign of power error signal fed to the APC when the APC angle surpasses the angle of unstable equilibrium point (UEP) is proposed in [64] to provide an emergency deceleration. An appropriate coupling between the Reactive Power Controller (RPC) to APC was suggested in [2, 65]. In these methods, the voltage reference increases to enhance transient stability. None of [2, 4, 52, 53, 54, 55, 56, 57, 58, 59, 61, 62, 63, 64, 65] took the effect of current limiters into consideration in the enhancement methods they proposed. Therefore, their enhancement methods might not be effective for GFM IBRs equipped with current limitation mechanisms.

Reference [36] suggested decreasing the active power reference to enhance the transient stability. It considered the VI current limitation mechanism in its modelling. The authors in [66] proposed to optimize the virtual impedance value to enhance transient stability while limiting the output current within its allowed range. Asymmetrical VI current limitation mechanisms were proposed in [67, 68] for enhancing transient stability. As discussed in the previous subsections, VI-based methods are slow in limiting the output current. Therefore, they are not studied in this thesis.

To eliminate the negative impact of the current saturation, reference [31] proposed to use the unsaturated reference current for calculating the virtual unsaturated power as the input of the APC. Reference [69] also suggested that instead of using the actual active power output as the input of the APC, virtual power can be used. This power is a

combination of the active power output and active power reference during the fault-on current saturation mode, and it is a coefficient of the active power during the post-fault current saturation mode. Reference [70] presented a method for changing the active power reference to enhance transient stability. Modifying the reference power during a voltage sag was proposed in [71] to enhance transient stability. A data-driven predictive control that changes the active reference power for optimal transient stability is presented in [72].

References [31, 69, 70, 70, 71, 72] reported different methods to change the power error as an input of the APC. Several methods in literature propose changing the APC more markedly to enhance the transient stability. For example, injecting additional kinetic energy was suggested in [73]. As another marked structural change, the estimated angle was used as the input of the APC instead of the active power for enhancing the stability margin in the current-saturation mode in [74]. In contrast, authors in [51] did not change the structure of APC. Instead, they developed a Lyapunov-based method to optimize the angle of the saturated current to maximize DOA while the APC structure was untouched.

None of the references [31, 51, 69, 70, 71, 72, 73, 74] have examined the possibility of the direct optimal changing of the APC angle as a state variable of the APC controller. To the best of my knowledge, only [75] proposed limiting the APC angle to avoid instability. However, this method needs PLL, which itself introduces the risk of instability in weak grids.

1.2.5 Gaps in knowledge

To the best of my knowledge, the literature lacks an accurate model of GFM IBRs equipped with CACRS facing large-signal disturbances. A mathematical expression for the set of returning angles has not been attempted. Therefore, the GFM IBR may experience unforeseen post-disturbance trajectories. This thesis will show that the angle of the saturated current has a significant role in the post-fault trajectory. If this angle is set incorrectly, the GFM IBR might converge into satSEP. A systematic approach for tuning the angle of the saturated current to avoid convergence to satSEP should also be proposed.

Even though many methods in the literature have been proposed for enhancing the transient stability of GFM IBRs, the full potential of modifying the structure of APC has not been exploited. In contrast to the synchronization of SGs, which are physics-defined, the synchronization of APC is totally software-defined. Therefore, full controllability of APC is achievable by adding proper signals to the APC.

1.3 Thesis Objectives and Contributions

Motivated by the gaps mentioned in the subsection 1.2.5, this thesis aims at following objectives:

- Providing an accurate large-signal model of GFM IBRs equipped with CACRS as their current saturation mechanism. The model determines the condition for transiting to/from the current saturation mode.
- Tuning the angle of the saturated current to avoid the convergence into the satSEP.
- Providing the optimal transient stability enhancement.

To realize the mentioned aims, the following contributions are proposed in this thesis:

- A mathematical expression for the set of returning angles is derived. Based on the inclusion of the APC angle in this set or the set of entering angles or their intersection, the operation mode of the GFM IBR is determined. If the APC angle is out of both of these two sets, it retains its mode. The mode of a GFM IBR determines the power-angle relation. Therefore, this expression is the fundamental step toward any model-based GFM IBRs' transient stability analyses.
- This thesis provides an analytical investigation on how the setting of the angle of the saturated current plays a prominent role in the post-fault transient stability behaviour of GFM IBRs. It is shown that the angle of the saturated current shapes the sets of returning angles, which in turn determines in which mode the GFM IBR operates at a specific APC angle.
- The angle of the saturated current is tuned to prevent locking into the current saturation mode through converging to the satSEP. A mix-integer program is modelled for this purpose.
- A model Predictive Control (MPC) method is proposed to determine the optimal active reference power change and corrective phase jump for achieving the optimal transient stability while maintaining safety conditions such as safe frequency range.

1.4 Research Dissemination

1.4.1 Publications

The following publications have been published/submitted based on the contributions and results of this thesis:

- Ali Arjomandi-Nezhad, Yifei Guo, Bikash C. Pal, and Damiano Varagnolo. "A Model Predictive Approach for Enhancing Transient Stability of Grid-Forming Converters." *IEEE Transactions on Power Systems* (2024).
- Ali Arjomandi-Nezhad, Yifei Guo, Bikash C. Pal, and Guangya Yang. "Modeling Fault Recovery and Transient Stability of Grid-Forming Converters Equipped With Current Reference Limitation." *IEEE Transactions on Energy Conversion*, (2024).
- Ali Arjomandi-Nezhad and Bikash C. Pal. "Stability Assessment Benchmark System Model." *deliverable D3.2 of InnoCyPES project*, available: cordis.europa.eu/project /id/956433/results (2023).
- Ali Arjomandi-Nezhad, and Bikash C. Pal. "Optimal Control of Grid-Forming Converters for Stability Improvement Considering Current Saturation" *Journal of Modern Power Systems and Clean Energy*, under review.

1.4.2 Presentation

As an Early-Stage Researcher funded by the InnoCyPES Marie-Curie program, I am responsible for communicating my research findings to the public. The following tutorial was presented in the project's summer school.

- Ali Arjomandi Nezhad, Eder Baron-Prada, "Tutorial - Fundamentals on IBRs control: grid-forming, grid-following and stability analysis." *InnoCyPES Summer School*, September 2025, Lecce, Italy (Hybrid). (The transient stability part of the tutorial is related to this thesis; the small-signal stability part is presented by Eder Baron-Prada, who is a PhD candidate at ETH Zurich and the Austrian Institute of Technology.)

The following item is presented at CIGRE-UK's Next Generation Network (NGN) annual general meeting in 2024.

- "An Overview of Challenges Imposed by the Current Limitation on Transient Stability of Grid-Forming Converters," *Keynote speech for CIGRE NGN Annual General Meeting*, Birmingham, UK, November 2024.

1.5 Organization of the Thesis

This thesis mainly aims at modeling and enhancing the transient stability of GFM IBRs, considering the impact of current saturation. More specifically, contributions of Section 1.3 are proposed in this thesis. For this aim, the remaining of this thesis is structured as:

- Chapter 2 reviews the structure of GFM IBRs and compares it with GFL IBR, which is the general term for IBRs currently connected to the electricity grid with limited services. Different types of current limitation mechanisms are also reviewed.
- Chapter 3 provides the detailed model for transient stability of GFM IBRs considering CACRS as the current limitation mechanism. The set of returning angles is introduced in this chapter. This is followed by a discussion on the post-fault behaviour of GFM IBR. Then, the circumstances in which the GFM IBR converges to the satSEP are investigated.
- In Chapter 4, the angle of the saturated current is optimized to avoid converging to the satSEP. The static controller proposed in this chapter is a solution to the challenges mentioned in Chapter 3 due to convergence to satSEP.
- Chapter 5 develops a model predictive dynamic controller for enhancing the transient stability of GFM IBRs. The objective function is to minimize the post-disturbance deviation from the SEP. The optimization yields the corrective input signals to the APC that steer the trajectory of the internal APC state variables. The constraints are either to model the dynamics of the GFM IBR or to put safety limitations.
- Finally, the thesis is concluded in Chapter 6. This chapter also provides a few suggestions for future research directions.

Chapter 2

A Review on Grid Following and Grid-Forming Inverter-based Resources

This chapter provides the fundamental background review which is needed to understand the remaining parts of the thesis. At first, a brief introduction to grid-following (GFL) and grid-forming (GFM) IBRs is provided. Then, dq-frame transformation and the model of fundamental passive elements in the dq-frame are reviewed. Then, the control structure of the grid-following converter and its main components, i.e. phase-locked loop (PLL) and current controller, are discussed. This is followed by reviewing the structure of grid-forming converters. Finally, different types of current limiters, which are essential to protect IBRs against overcurrent, are introduced and compared.

2.1 A brief introduction to grid-following and grid-forming IBRs

Insulated-gate bipolar transistor (IGBT)-based inverters, which connect the DC side of renewable energy resources or batteries to the AC grid, operate as voltage sources with voltage magnitudes proportional to their pulse width modulation (PWM) carrier signals [1]. Nevertheless, the exact magnitude and angle of this carrier should be carefully controlled to inject active and reactive power in a controlled way. The angle of the PWM carrier should be synchronized with the grid to which the inverter is connected through an

inductor. A PLL is usually used for this purpose. It estimates the angle and the frequency of the voltage at the connection point. This estimation is a reference for controlling the IBR. Since these IBRs follow the angle of the voltage of the connection point, they are called grid-following IBRs, which is discussed in the following subsection.

2.1.1 Grid-following IBRs

GFL IBRs control the current output to a certain amount to inject a reference active and reactive power to the connecting power grid. Therefore, they are defined as the current source in transient time frames [76]. This definition can be more precise if we mention that GFL IBRs are current sources within the bandwidth of their current control time frames. This bandwidth is very fast as it is not constrained by any physical limitations other than the PWM switching frequency. The current control loop's dynamics should be considerably slower than the PWM switching.

As GFL IBRs replace synchronous generators (SGs), the current sources become more abundant while voltage sources are eliminated. The PLL of GFL IBRs need stiff voltage at the point of connection for synchronism [77]. If PLL's angle estimation error has a considerable effect on the angle of the connection point voltage, the PLL's accurate performance will be challenged. Therefore, the need for more voltage sources to maintain the voltage in an IBR-dominant power system will be evident. Besides, GFL IBRs lack several services that SGs inherently or auxiliarily provide for the grid. One of the most essential inherent services from SGs for the grid is inertia. The kinetic energy stored in the rotor of rotating masses of SGs limits the rate of change of frequency (RoCoF) in adverse situations. The GFL IBRs lack this characteristic. The services needed in an IBR-dominant power system are reviewed in detail in the following subsection.

2.1.2 Services required in IBR-dominant power systems

Traditionally, the required services identification process in an SG-dominant power system is tightly coupled with the characteristics of SGs [76]. This means that services are defined based on what SGs can provide to the grid to supply demand, subject to the limitations of an SG-dominant grid. These limitations can arise from SGs themselves, primary energy resources, power transmission and distribution elements, protection devices, or loads. With the replacement of SGs in favor of IBRs, the following factors contribute to the change in defining the required services [76]:

- The services that were only required for the safe operation of the SGs are less required. However, the services required for the safe operation of other grid elements, such as rotating loads, are still needed. For example, the frequency containment limitations might be less tight; however, voltage control requirement is still needed at the same level. New types of services might be required by the emerging types of generation resources, i.e. IBRs.

- The characteristics of IBRs are functions of their control structure. This is in contrast with SGs, which behave according to their physical nature. Therefore, there is an opportunity to redesign the characteristics of IBRs to provide the required services.

- The services that SGs provided inherently might also be provided by IBRs with a modified control structure, but this provision entails extra costs.

- IBRs are bounded with tight safety conditions such as limited over-current capacity. These conditions should be considered when IBRs' controller is redesigned for providing services.

Therefore, the need for services can be redefined to run the power systems economically while an acceptable level of reliability is ensured. Reliability involves two main concerns [78]: *a*) adequacy, which means the existence of adequate resources to meet demand, and *b*) security, which is the ability to continue a safe operation following a disturbance. Required services can also be categorized based on whether they address adequacy or security needs.

From the adequacy point of view, capacity and energy are two main concerns. There should be enough generation, transmission, and distribution capacity installed in the grid to serve the demand in different scenarios. A portion of the capacity should be dispatchable to handle the variability of renewable generation. Installed capacity is not the only indicator of adequacy. Sufficient primary energy resources are also required to serve customers [76].

From the security aspect, the following services are the most important requirements to ensure the safe operation of the power systems [76, 77]:

- Angle stability and synchronization: Following a disturbance, the internal angles of resources oscillate against each other, or the angle differences keep on increasing. The resources should remain synchronized with each other despite the disturbance through sufficient damping and synchronizing torque. Otherwise, some resources may disconnect from the grid, or the grid may separate into multiple islands. The ability to ride through a phase jump at the point of connection is also located in

this subcategory of services. Some IBRs can even be expected to mitigate this phase jump as an additional service. This mitigation can be achieved by proper injection of power to compensate for the source of the phase jump.

- Frequency regulation: The frequency after a disturbance, e.g. the loss of a big generation unit, should be contained in a safe range. In an IBR-dominant power system, equipping the IBRs with primary frequency control helps to satisfy this requirement. Even though the primary frequency control for IBRs can be fast, the frequency may adversely change before its activation. As a response, the virtual inertia service is also needed to limit this change within the first few milliseconds. Increasing the active power injection in response to an under-frequency event requires an energy buffer in the DC side. This buffer is provided by either equipping the DC side with storage units or operating the renewable resources lower than their maximum power point. These two options increase the investment cost and opportunity cost, respectively. With the elimination of SGs, the safe frequency operation will be also released in the long term.

- Voltage regulation: The voltage of the buses should be contained within its safe limits. This can be provided by volt-var control from IBRs. Voltages should also be far from the nose of the voltage-power curve with a sufficient margin to avoid voltage collapse. Voltage regulation is a local problem in contrast to frequency control, which is a grid-wide problem if the system is synchronized.

- Damping: Both inter-area oscillations and sub-synchronous oscillations pose instability risks to the grid. A sufficient amount of damping is required to ensure the stable operation of power systems.

- Restoration: After major outages, some resources should be able to black-start and also pick up cold loads, which initially demand a high amount of available power and energy. GFL IBRs are not designed for this purpose.

2.1.3 Grid-forming IBRs

Most of the services mentioned in the previous subsection are not provided by GFL IBRs. Therefore, GFM IBRs are proposed in the literature to provide the grid with the services and comply with the requirements. The main services and requirements expected from GFM IBRs are (1) grid frequency and voltage support, (2) fault ride through, (3) providing

small-signal stability damping, (4) stable connection to weak grids, and (5) restoration and black-start capability [79].

A GFM IBR is defined as an IBR whose control structure is designed to keep a constant or nearly constant internal voltage phasor in sub-transient to transient time frames [79]. The reference magnitude, freq and angle of this voltage are usually determined based on volt-var control and frequency control objectives. This reference is either used directly as the voltage of the inverter, i.e., single-loop GFM IBRs [80], or as a reference for the voltage of the connection point. In the latter approach, the current reference is the actuator for the voltage control. Hence, it is called multi-loop GFM IBR [39]. GFM IBR can be categorized into several types depending on the control logic generating the voltage magnitude reference, frequency, and angle. The most popular types are:

- Droop control: There is a frequency droop rule between the active power output and frequency, the same as the traditional governor control for primary frequency control. Similarly, there is a linear droop rule between the reference voltage magnitude and reactive power output [81].
- Virtual synchronous generators (VSG): It emulates the second-order swing equation. Therefore, the GFM IBR provides the grid with inertia service to limit the RoCoF [2].
- Power Synchronization control: This type of GFM IBR is almost the same as the droop control type, with the difference that there is a linear droop rule between active power and angle instead of frequency. It has been initially proposed for GFM IBRs in microgrids [81].

2.2 Control structure of grid-following and grid-forming IBRs

This section reviews the general structure of GFM and GFL IBRs. Since they are mostly controlled in a dq-frame, the following subsection reviews the dq-frame transformation before delving into the structure of GFM and GFL IBRs.

2.2.1 Preliminary: dq-frame transformation

The AC side of transmission-connected IBRs is usually connected to a three-phase AC bus. Therefore, controlling the output variables, i.e. voltage and current, which are also

three-phase AC, is challenging. As a response to this challenge, the three-phase AC signals are projected to a synchronous rotating dq-frame [1], aka local reference frame [82]. The relation between the projected signals and original signals follows:

$$\begin{bmatrix} v_d \\ v_q \\ v_0 \end{bmatrix} = \frac{2}{3} \begin{bmatrix} \cos(\theta(t)) & \cos\left(\theta(t) - \frac{2\pi}{3}\right) & \cos\left(\theta(t) + \frac{2\pi}{3}\right) \\ -\sin(\theta(t)) & -\sin\left(\theta(t) - \frac{2\pi}{3}\right) & -\sin\left(\theta(t) + \frac{2\pi}{3}\right) \\ 0.5 & 0.5 & 0.5 \end{bmatrix} \begin{bmatrix} v_a(t) \\ v_b(t) \\ v_c(t) \end{bmatrix}, \tag{2.1}$$

where $\theta(t)$ is the angle of the transformation. This angle traditionally corresponded to the angle between synchronous generators' rotor and stator's poles [83]. For inverters, there is no rotor or stator. Hence, the IBR's controller is responsible for generating the angle of the dq-frame transformation. To illustrate more on this transformation, consider the balanced three-phase voltage $v_{abc}(t)$ as

$$\begin{bmatrix} v_a(t) \\ v_b(t) \\ v_c(t) \end{bmatrix} = \begin{bmatrix} V_m \cos(\psi(t)) \\ V_m \cos\left(\psi(t) - \frac{2\pi}{3}\right) \\ V_m \cos\left(\psi(t) + \frac{2\pi}{3}\right) \end{bmatrix}. \tag{2.2}$$

The transformed signal is

$$\begin{bmatrix} v_d \\ v_q \\ v_0 \end{bmatrix} = \begin{bmatrix} V_m \cos\left(\psi(t) - \theta(t)\right) \\ V_m \sin\left(\psi(t) - \theta(t)\right) \\ 0 \end{bmatrix}. \tag{2.3}$$

If the angle of the transformation ($\theta(t)$) and the angle of the three-phase voltage change ($\psi(t)$) at the same rate, i.e., they are synchronized. v_d and v_q become DC signals, which are easier to control. The synchronization mechanisms are explained in detail in the next subsections.

To control the electrical output variables of an IBR, the passive elements which form the dynamics of the filters and connecting lines should be modelled in the dq-frame. The most

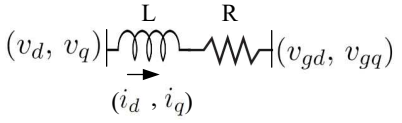


FIGURE 2.1: An elementary series RL branch.

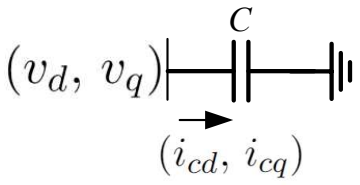


FIGURE 2.2: An elementary shunt capacitor branch.

common passive elements are capacitors and series resistance and inductance, which are either the output filter elements or the equivalent model of connecting transformer and grid Thevenin model. The voltage and current of an RL branch, as shown in Figure 2.1, in the dq-frame are mathematically modelled as

$$v_d = v_{gd} + Ri_d - \omega L i_q + L\frac{di_d}{dt}, \tag{2.4}$$

$$v_q = v_{gq} + Ri_q + \omega L i_d + L\frac{di_q}{dt}, \tag{2.5}$$

where $\omega = \dfrac{d\theta(t)}{dt}$ [1]. Terms $-\omega L i_q$ and $\omega L i_d$ are cross-coupling terms, which couple d and q coordinates' dynamics. The terms $L\dfrac{di_d}{dt}$ and $L\dfrac{di_q}{dt}$ can be neglected if the current projections to the d and q coordinates are constant. This assumption is invalid if the phenomenon is as fast as the current control loop.

The voltage across and current passing through a capacitor is modelled as [1]

$$i_{cd} = -\omega C v_q + C\frac{dv_d}{dt}, \tag{2.6}$$

$$i_{cq} = \omega C v_d + C\frac{dv_q}{dt}. \tag{2.7}$$

Similarly, $-\omega C v_q$ and $\omega C v_d$ are coupling terms. $C\dfrac{dv_d}{dt}$ and $C\dfrac{dv_q}{dt}$ models the dynamics of this passive capacitor. Throughout this thesis, the fast dynamics of passive elements are neglected unless explicitly mentioned. Nevertheless, all simulations are performed using the MATLAB/Simulink Simscape electromagnetic transient (EMT), which considers the fast dynamics of passive elements as well. Please note that in some implementations in

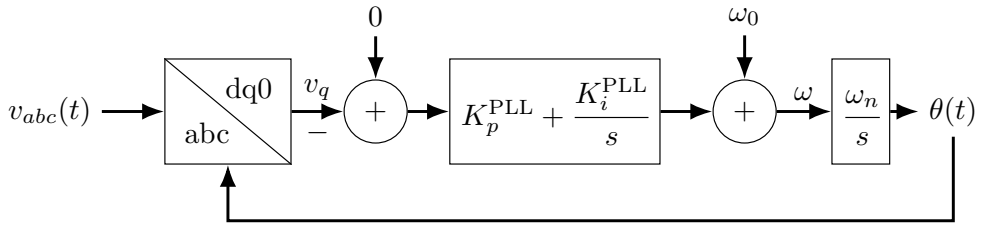


FIGURE 2.3: The general control structure of a PLL.

other references, the q-axis lags the d-axis. In those implementations, the conversion equation and modelling equations are different. In this thesis, the q-axis leads the d-axis.

2.2.2 Control structure of grid-following inverter-based resources

Traditionally, IBRs synchronize themselves to the grid by estimating the angle and frequency of the point of connection through a PLL [1]. This angle is used as the angle of the dq-frame transformation explained in the previous section. According to the equation (2.3), $\theta(t) = \psi(t)$ if $v_q = 0$. Therefore, most PLLs are designed to control v_q to the zero value, as shown in Figure 2.3 [84, 85]. The output of the PLL is used as the angle reference for the IBRs' control system. Since these IBRs are designed to follow the voltage of the connection point, they are called grid-following IBRs [85]. They have been used in industry for years without being called GFL IBRs. Only recently, after the advent of the grid-forming IBR concept, have they been called grid-following to highlight the contrast.

The general structure of a grid-following inverter is shown in Figure 2.4. The references for the current alongside the d and q axes are generated based on active and reactive power references. In some severe events, e.g., three-phase faults, the magnitude of the current reference might exceed the maximum allowed value. Therefore, it is saturated to the maximum value. The current reference saturation mechanisms are explained in more detail later in Subsection 2.3.1. Then, the current controller, which is the inner controller, is responsible for controlling the current to the current reference. The structure of a decoupled current controller with feedforward terms is shown in Figure 2.5 [1]. Decoupling term causes separation of the dynamics in the d and q directions. The equivalent model of the current control loop in both d and q directions is shown in 2.6 [1]. Current controllers' parameters, i.e. K_p^{CC} and K_i^{CC} can be tuned for a fast time constant of a few milliseconds. Therefore, grid-following converters act as current sources for time-frames more than a couple of milliseconds. Thus, they are also called voltage-following current-forming in [85].

As depicted in Figure 2.4, the output of the PLL affects the projection of the current into the dq-frame. The projected current is controlled to follow the reference current in the d and q axis. This, in turn, affects the voltage at the point of connection, which serves as the input of the PLL. Therefore, a closed loop path from the output of the PLL to the output current and, then, to the output voltage and, finally, the input of the PLL exists. If the grid voltage is stiff, the output voltage is less sensitive to the output current. Therefore, the gain from the PLL output to voltage error is small, and the closed-loop synchronization is more stable. However, if this voltage is less stiff, this closed-loop synchronization is less stable. It happens in weak grid conditions [77].

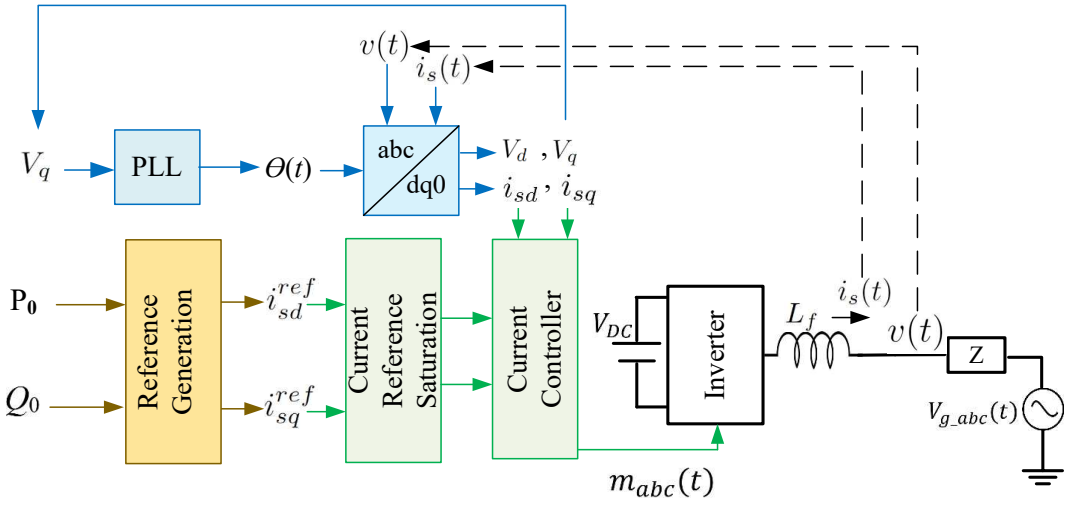


FIGURE 2.4: The control structure of a GFL IBR.

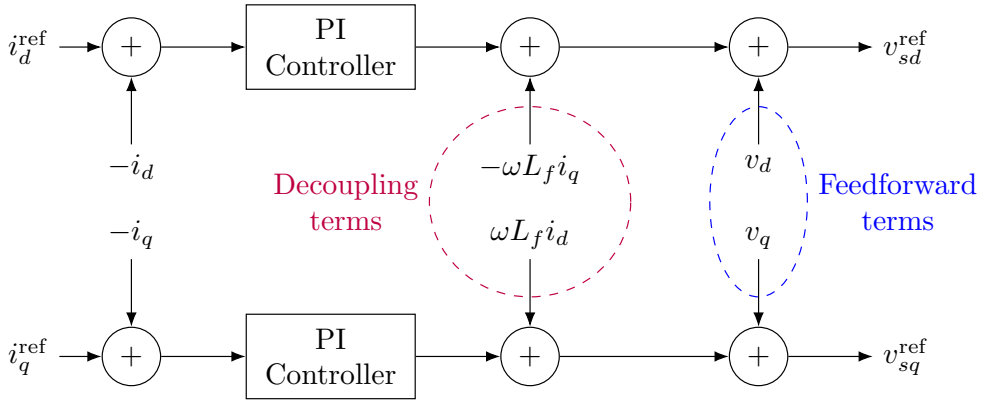


FIGURE 2.5: The control diagram of the decoupled current control with feedforward terms.

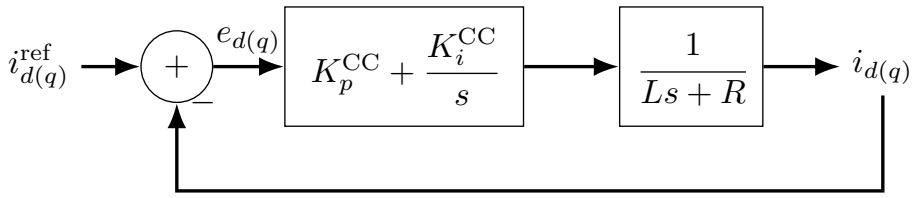


FIGURE 2.6: The equivalent block diagram of the current control loop alongside d and q directions.

Since synchronous generators are being replaced by GFL IBRs, which act as current sources, stiff voltage sources are becoming less available. Thus, the synchronization of the operating GFL IBRs is jeopardized. Besides, the elimination of synchronous generations decreases the total grid inertia. Therefore, the rate of change of frequency is adversely affected by the transition from synchronous generator-based resources to IBRs [86]. Furthermore, GFL IBRs generally lack black-start capabilities. These concerns raise the need for revising the control structure of some IBRs to provide the grid with services such as stiff voltage sources, the ability to connect weak grids, virtual inertia, black start capability, etc.

2.2.3 Control structure of grid-forming inverter-based resources

The essence of redesigning the control structure of some of the IBRs to act as a voltage source and provide the grid with several services has been a motivation for the introduction of the grid-forming converters concept in literature [10]. Grid-forming converters generally control the angle and magnitude of the voltage of the connection point instead of following the angle of this voltage. The references for the angle and frequency of the dq-frame are determined by the active power controller (APC). The magnitude of the terminal voltage reference is generated by the reactive power controller (RPC).

This thesis focuses on VSG GFM IBRs [2]. Nevertheless, the methodology can be extended to other types of GFM IBRs with some modifications for adaptations. The structure of this GFM IBR is shown in Figure 2.7. The GFM IBR is connected to the grid, which is modelled as the Thevenin voltage of V_g and Thevenin impedance Z_g through a transformer with the impedance Z_t and an LC filter. The inductance of the filter is L_f, and the capacitance of the filter is C. Therefore, the total shunt impedance is $y = j\omega C$ if the line shunt capacitance is ignored. The total series impedance from the point of connection is $Z = Z_g + Z_t = R + jX$. The phase angle of this impedance is ϕ. The complement of this angle ($\alpha = 90° - \phi$) is used in several expressions in Chapter 3. The APC and RPC

composite the outer layer control of the GFM control structure. The APC generates the angle of the dq-frame transformation ($\theta(t)$). The difference between this angle and the angle of the Thevenin grid voltage ($\theta_g(t)$) is the APC angle ($\delta = \theta(t) - \theta_g(t)$), which plays the principal role in synchronization. The RPC generates the voltage reference along d-axis direction (V_d^{ref}) based on the voltage-reactive power droop role [2]. The voltage reference along q-axis is zero. Therefore, the inner layer voltage controller is responsible for following the voltage magnitude reference generated by the RPC with the angle and frequency of APC [49]. The voltage controller generates the current reference applicable to the innermost layer, which is the current controller.

This thesis uses the decoupled structure with feedforward terms as the voltage controller according to Figure 2.8 [42]. The feedforward coefficients are assumed to be equal to one in the thesis. However, some references, such as [87], suggested using a coefficient less than one for small-signal stability robustness.

The equivalent model of the voltage control loop is shown in Figrue 2.9 [1]. In this figure, τ^{CC} is the time constant of the innermost current control loop, K_p^{VC} and K_i^{VC} are the voltage PI controller's coefficients.

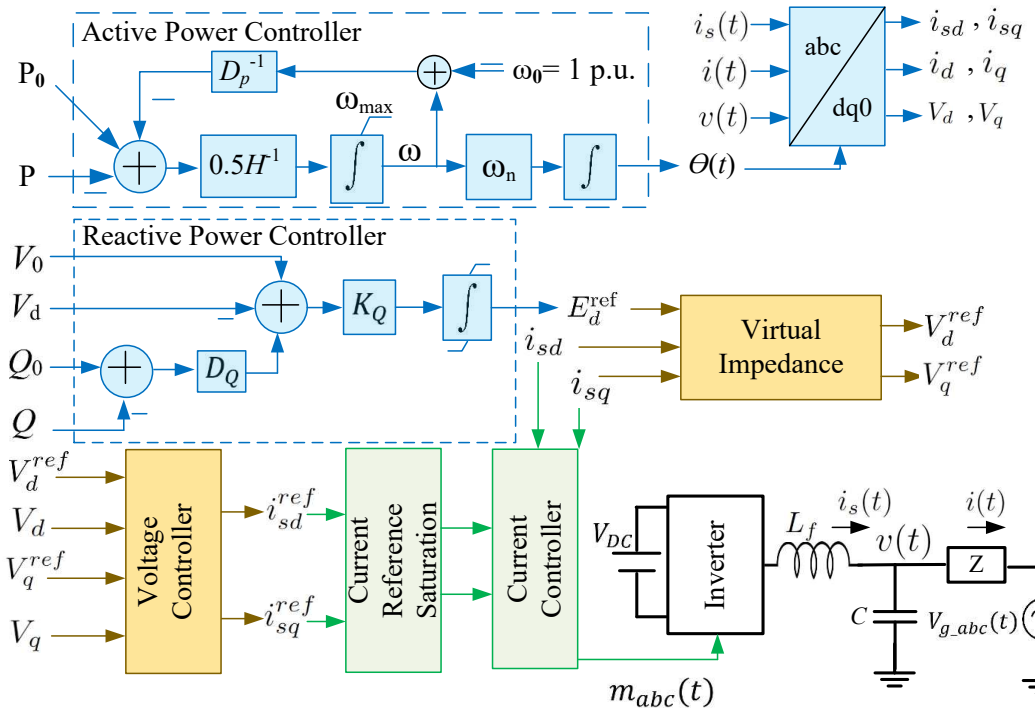


FIGURE 2.7: The general structure of a multi-layer VSG GFM IBR.

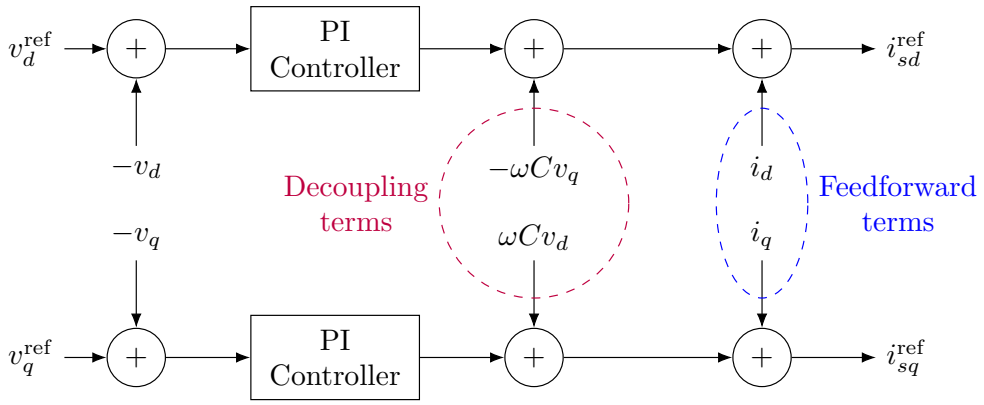


FIGURE 2.8: The control diagram of the decoupled voltage control with feedforward terms.

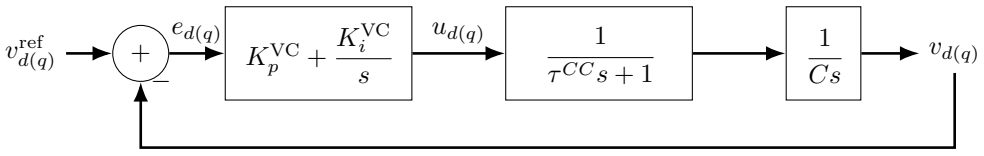


FIGURE 2.9: The equivalent model of voltage control loop alongside d and q directions.

The current reference generated by the voltage controller might exceed the current limitation in some adverse situations that are discussed in more detail in Chapter 3. In these situations, the current reference should be limited. There are generally two categories of current limitation methods: (1) Current reference saturation, which directly limits the reference generated by the voltage controller, and (2) virtual impedance, which limits the current by emulating a sufficiently large impedance between the reference voltage and the output terminal. The position of these two limiters within the GFM control structure is shown in Figure 2.7. A GFM IBR might be equipped with either one or both of these two current limitation mechanisms. Virtual impedance can also be used to enhance small-signal stability and damping oscillations in normal operation mode [88]. The design of a virtual impedance block for small-signal damping provision might be different from that of a virtual impedance block used for the current limitation.

2.3 Current Limitation Mechanisms

This section reviews the detailed structures of the most popular types of current limiters and provides a brief comparison of the benefits and deficiencies of different structures.

2.3.1 Current Reference Saturation

The current reference saturation block directly saturates the current reference generated by the voltage controller in case of an over-current. Therefore, it is as fast as the current controller, and the current is limited to the allowable range promptly. However, it acts as a current source upon current saturation. In this situation, the voltage does not follow the reference (V_d^{ref}, V_q^{ref}). This is not desired as GFM IBRs are expected to operate as voltage sources. In this thesis, this mode of operation is called the current-saturation mode, which is in contrast to the normal operation mode.

The magnitude of the saturated current is the maximum allowable current; however, its angle depends on the specific design. The most popular current reference saturation design types are constant angle current reference saturation (CACRS), circular limiter, d-axis priority, and q-axis priority. These types are explained in more detail in the following subsections.

2.3.1.1 Circular Limiter

A circular limiter limits the current reference to a current with the magnitude of $I_s^{\max}$ and the same angle as the unsaturated current according to [45]

$$\overline{i_{sdq}^{\text{ref}}} = \begin{cases} i_{sdq}^{\text{ref}} & \text{if} \quad |i_{sdq}^{\text{ref}}| \leq I_s^{\max} \\ \dfrac{i_{sdq}^{\text{ref}}}{|i_{sdq}^{\text{ref}}|}.I_s^{\max} & \text{if} \quad |i_{sdq}^{\text{ref}}| \geq I_s^{\max}. \end{cases} \tag{2.8}$$

Figure 2.10 provides a visual demonstration of different current reference saturation methods. In this figure, current I_1^{sat} is the circular saturated current if the reference generated by the voltage controller is I_s. This figure depicts that the circular limiter scales down the current in the same direction. This type of current limiter is usually applicable to GFM IBRs with virtual admittance as their voltage control mechanism [38].

2.3.1.2 Constant Angle Current Reference Saturation

When a GFM IBR equipped with CACRS operates in the current-saturation operation mode, the current is fixed in a constant angle from the d-axis (β). This current limitation

method is mathematically formulated as [49]

$$\overline{i_{sdq}^{\text{ref}}} = \begin{cases} i_{sdq}^{\text{ref}} & \text{if} \quad |i_{sdq}^{\text{ref}}| \leq I_s^{\max} \\ (I_s^{\max}\cos\beta, I_s^{\max}\sin\beta) & \text{if} \quad |i_{sdq}^{\text{ref}}| \geq I_s^{\max}. \end{cases} \tag{2.9}$$

I_4^{sat} in Figure 2.10 is the saturated current if it is saturated through CACRS. The angle of saturated current (β) can be tuned for technical requirements such as voltage support and maintaining stability when the GFM IBR faces a severe disturbance. Since the current reference before and after the saturation is discontinuous, there is the possibility of oscillating between normal operation mode and current-saturation operation mode due to the current reference jumps. The operation of a GFM IBR equipped with CACRS is analysed in detail in Chapter 3.

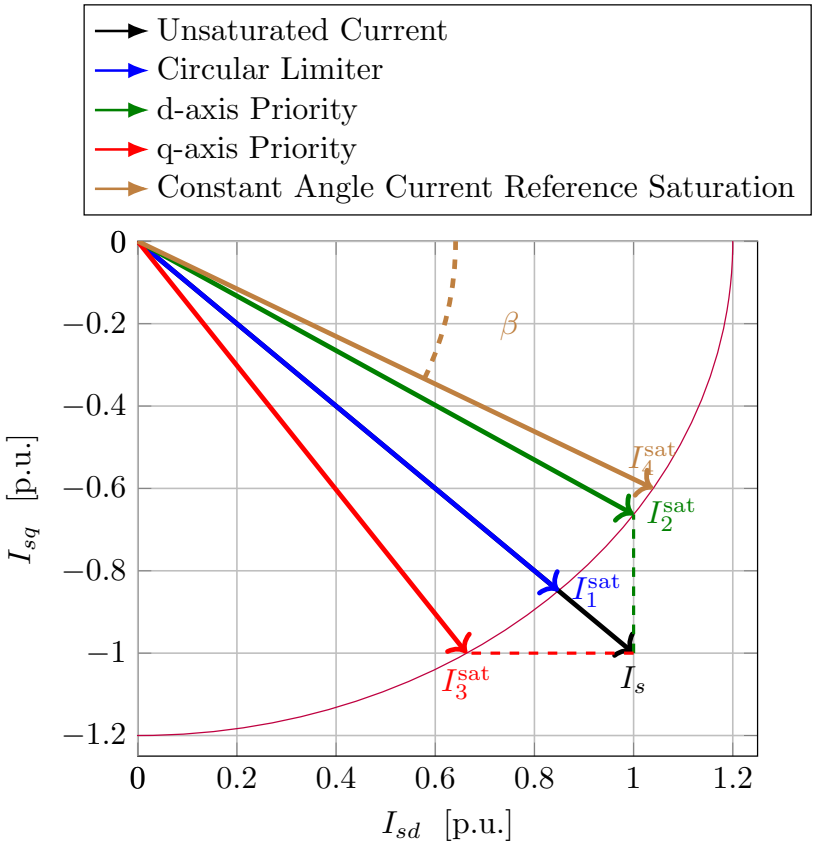


FIGURE 2.10: A visual comparison of the most popular current reference saturation methods.

2.3.1.3 d-axis Priority

In this type of current reference saturation, the d-axis component of the current reference generated by the voltage controller can change between $-I_s^{\max}$ and $I_s^{\max}$. The other component can change within the remaining current injection capability [45]. Mathematically, it is asserted as

$$\overline{i_{sd}^{\text{ref}}} = \max(|i_{sd}^{\text{ref}}|, I_s^{\max}).\mathbf{sign}(i_{sd}^{\text{ref}}), \tag{2.10}$$

$$\overline{i_{sq}^{\text{ref}}} = \max(|i_{sq}^{\text{ref}}|, \sqrt{(I_s^{\max})^2 - (\overline{i_{sd}^{\text{ref}}})^2}).\mathbf{sign}(i_{sq}^{\text{ref}}). \tag{2.11}$$

I_2^{sat} in Figure 2.10 is the saturated current if it is saturated through d-priority current reference saturation.

As depicted in Figure 2.8, i_{sd}^{ref} and i_{sq}^{ref} are the actuators for controlling the voltage in d and q directions, respectively. Therefore, if the current saturation mechanism is d-priority current saturation, adjusting V_d to V_d^{ref} is prioritized. Only when the current reference alongside d axis reaches the limitation, V_d cannot track V_d^{ref}. As a result, three possible operation modes are

- Normal operation mode
- The current is saturated alongside the q-axis direction, but it is not saturated in the d-axis direction. Therefore, V_d tracks V_d^{ref}, but V_q does not follow V_q^{ref} (usually zero).
- The current is saturated in both axes.

2.3.1.4 q-axis Priority

The current saturation mechanism for the q-axis priority method is the same as the d-axis priority method, with the difference that the current in the q-axis is prioritised. Therefore, the controller prioritises keeping V_q follow V_q^{ref} (usually zero). The relation between the saturated and unsaturated reference current follows [45]

$$\overline{i_{sq}^{\text{ref}}} = \max(|i_{sq}^{\text{ref}}|, I_s^{\max}).\mathbf{sign}(i_{sq}^{\text{ref}}) \tag{2.12}$$

$$\overline{i_{sd}^{\text{ref}}} = \max(|i_{sd}^{\text{ref}}|, \sqrt{(I_s^{\max})^2 - (\overline{i_{sq}^{\text{ref}}})^2}).\mathbf{sign}(i_{sd}^{\text{ref}}) \tag{2.13}$$

I_3^{sat} in Figure 2.10 is the saturated current if it is saturated through q-priority current reference saturation.

2.3.2 Virtual Impedance

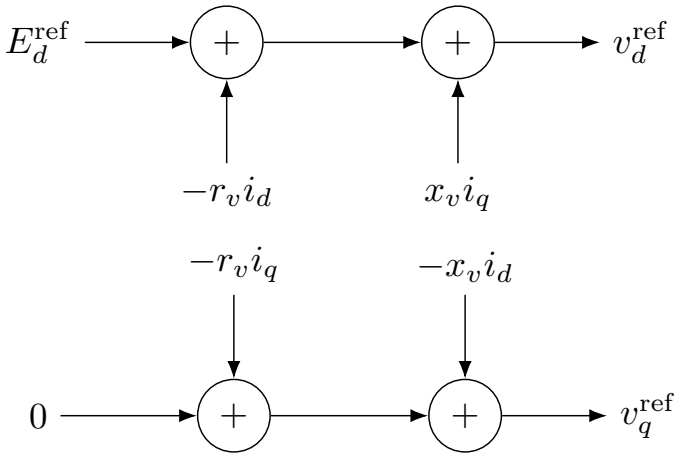


FIGURE 2.11: The block diagram implementation of the virtual impedance

In this method, an impedance is emulated behind the point of connection of GFM IBRs [35]. To do so, the voltage reference generated by the RPC is subtracted by the virtual impedance terms according to Figure 2.11. Then, this subtracted voltage reference is given to the voltage controller. The value of the virtual impedance is usually zero before over-current detection. Upon the over-current detection, this virtual impedance gets a non-zero value to limit the current [35]. A GFM IBR keeps operating as a voltage source if the implemented current limiter is a virtual impedance. Nevertheless, the activation of the current limitation functionality of the virtual impedance is delayed by the voltage controller's bandwidth because it is cascaded with the voltage controller. However, a GFM IBR with a virtual impedance current limiter must be able to withstand over-current for a few milliseconds.

Chapter 3

Modelling Transient Stability of Grid-Forming Converters Considering Current Saturation

This Chapter models the transient stability behaviour of grid-forming converters equipped with constant angle current reference saturation (CACRS). To realize this aim, the causes of entering the current-saturation mode are first identified. Exact expressions for the situations in which a GFM IBR enters the current-saturation mode and returns to normal operation mode are provided. It is observed that these two situations might overlap. In these cases, the GFM IBR oscillates between normal operation mode and current-saturation mode. In other words, as soon as the current reference decreases below the threshold and the GFM IBR enters the normal operation mode, the current reference magnitude increases again above the threshold. Therefore, the GFM IBR oscillates between these two modes.

After deriving an exact model for entering and returning from the current-saturation mode, the effect of current saturation on the transient stability of GFM IBR is investigated. It will be inferred that not only does the current saturation cause a decrease in the deceleration area, but it also introduces a saturated stable equilibrium point (satSEP) to the set of singular points. The circumstances in which a GFM IBR converges to the satSEP are also explored in this chapter. To summarize, the main contribution of this chapter is to provide a detailed model of the transient stability of GFM IBRs equipped with CACRS. In addition, the effect of the angle of the saturated current on this behaviour is analyzed. This analysis is a prerequisite for the angle tuning in Chapter 4.

3.1 Synchronism and Transient Stability Definition

The active power flow from different buses in a power transmission network is highly correlated with angle differences between the buses. Therefore, if the angles of these buses oscillate against each other or they operate at different frequencies, huge power oscillations between parts of the network will be observed. Hence, it is necessary that the angle differences between the voltages of buses remain constant values. This essence is called synchronism.

A power grid is always subjected to disturbances, which puts synchronism at risk. These disturbances are usually small. The ability of the system to retain synchronism after being subjected to small disturbances is called small-signal stability [89]. Linear computational techniques are sufficient for the small-signal stability analyses. The system is also occasionally subjected to large disturbances, e.g. short-circuit faults and sudden phase jumps. In these cases, the angles deviate considerably from the synchronism equilibrium. The ability to retain synchronism after facing severe disturbances is called transient stability [89]. Since the large-signal behaviours of the resources are highly nonlinear, linear control theory techniques are not sufficient for transient stability analysis.

Traditionally, power systems were dominated by synchronous generators. In those grids, the angles of the rotors of the synchronous generators were the key variables for maintaining synchronism. Therefore, transient stability was equal to the transient rotor angle stability in case of large disturbances [11]. With the advent of IBRs, the internal angles of IBRs generated by either a phase-locked loop (PLL) or an active power controller (APC) also play an important role in synchronism. Therefore, the rotor angle stability concept is extended to the angle stability.

3.2 Synchronism of Grid-Forming Inverter-based Resources

A GFM IBR synchronises itself to the grid through the APC. Therefore, the stability of the APC angle is the condition for the synchronism of the GFM IBR. In this thesis, it is assumed that the rest of the network can be modelled as a Thevenin equivalent. This assumption decreases computational complexity with the cost of neglecting the interactions between converters. Even though this assumption is not exact, it is a valid starting point for modelling the dynamics of GFM IBR before modelling all interactions in detail, as will be suggested as future work in Chapter 6. The difference between the angle of the local

reference frame, generated by APC, and the common reference frame, which is the angle of the Thevenin voltage, is called APC angle δ. Figure 3.2 shows the equivalent dynamics of the active power control loop. Any change in δ causes a change in the active power output, which is the feedback of the APC loop.

In steady-state, the terminal voltage is regulated on the d-axis of the local reference frame as shown in Figure 3.1. The active power flowing from the IBR's terminal to the grid is calculated as

$$P = \frac{(V_d^{\text{ref}})^2}{Z}\sin\alpha + \frac{V_g V_d^{\text{ref}}}{Z}\sin(\delta - \alpha), \tag{3.1}$$

where $\alpha = \arctan\dfrac{R}{X}$. If the grid is inductive, $\alpha = 0°$, and if the grid is resistive, $\alpha = 90°$. This relation is the same as the power-angle curve in traditional SG-based power systems. Therefore, the SG-based transient stability assessment methods can be applied in this case. However, the power-angle relation changes upon switching from the normal operation mode to the current-saturation mode. This relation, which is demonstrated as $P - \delta$ relation in Figure 3.2, plays a pivotal role in shaping the transient stability behavior of GFM IBRs.

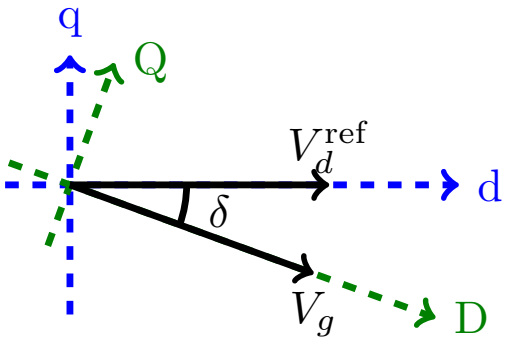


FIGURE 3.1: The GFM IBR's terminal voltage and grid Thevenin voltage phasor diagram in the steady-state normal operation mode.

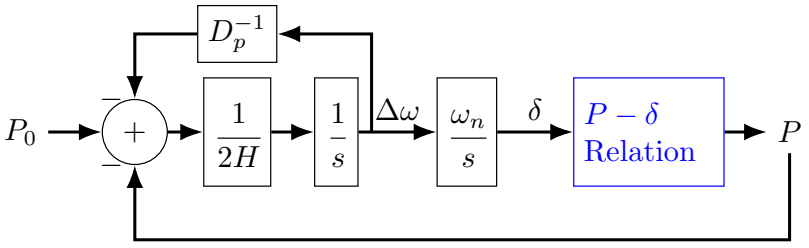


FIGURE 3.2: The active power control closed-loop schematics.

When the GFM IBR is in the current-saturation mode, this relation does not follow (3.1) anymore. Instead, it follows (3.11), which is discussed in subsection 3.3.1. The $P-\delta$ block in Figure 3.2 changes its relation upon transition to the current-saturation mode. Hence, the current saturation significantly affects the transient stability. The prerequisite to understanding the effect of current saturation on transient stability is understanding the causes of current saturation. Besides, the situations in which a GFM IBR enters or returns from the current-saturation operation mode should be identified. Ideally, these situations are expressed as a function of δ so that the power-angle relation can be expressed as a piecewise function. The multi-layer complex control structure of the GFM IBR challenges achieving this aim. The following subsections aim to realize this aim.

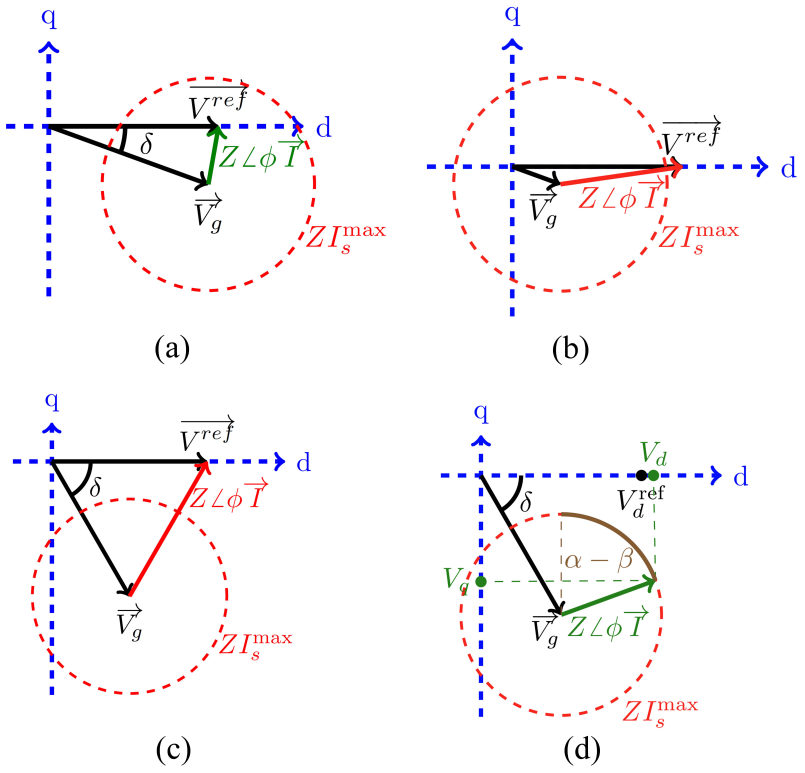


FIGURE 3.3: Phasor-Diagram of the voltages in (a) steady-state normal operation mode, (b) a severe voltage drop situation in the absence of current limitation, (c) a large APC angle (δ) situation in the absence of current limitation, and (d) a large APC angle with constant angle current reference saturation.

3.3 Modelling GFM IBR in the current-saturation operation mode

In the steady-state normal operation mode, the GFM IBR's terminal voltage is $V_d^{\text{ref}}\angle 0$, and the Thevenin voltage of the grid is $V_g\angle -\delta$. As a result, the current injected into the grid is

$$I = \frac{V_d^{\text{ref}}\angle 0 - V_g\angle -\delta}{Z\angle\phi}. \tag{3.2}$$

Neglecting the filter's capacitor, the inverter's current is the same as the current injected into the grid. In normal operation, this current is less than the maximum allowed inverter current, as shown in Figure 3.3(a). However, a deep voltage sag (like a three-phase fault) or a big APC angle (δ) causes overcurrent, as depicted in Figure 3.3(b) and (c). Therefore, the GFM IBR transitions to the current-saturation mode.

In the current-saturation mode, the saturated reference is fed to the current controller instead of the reference generated by the voltage controller. Therefore, the voltage control aim is not met, and the voltage is not regulated to $(V_d, V_q) = (V_d^{\text{ref}}, 0)$ as demonstrated in Figure 3.3(d). From a physical interpretation point of view, a deep voltage sag corresponds to a large reactive power injection from the GFM IBR to the grid, while a large APC causes a large active power flow from the GFM IBR to the grid. Both of these cases endure inverter overcurrent.

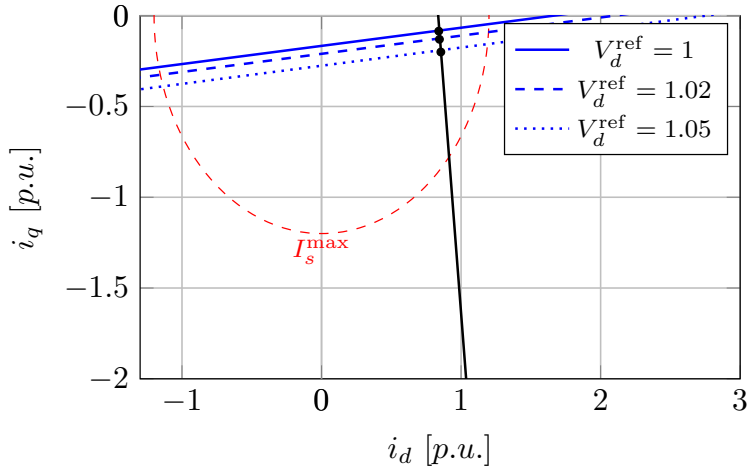


FIGURE 3.4: The changes in the equilibrium point of the voltage controller due to minor changes in the voltage reference.

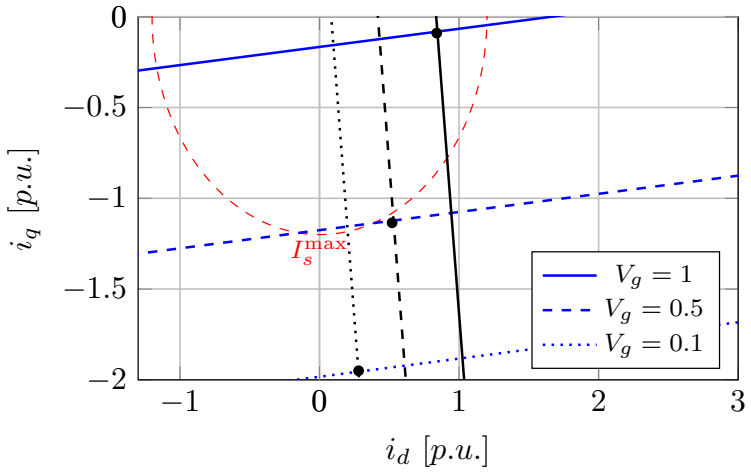


FIGURE 3.5: The changes in the equilibrium point of the voltage controller due to a severe voltage sag.

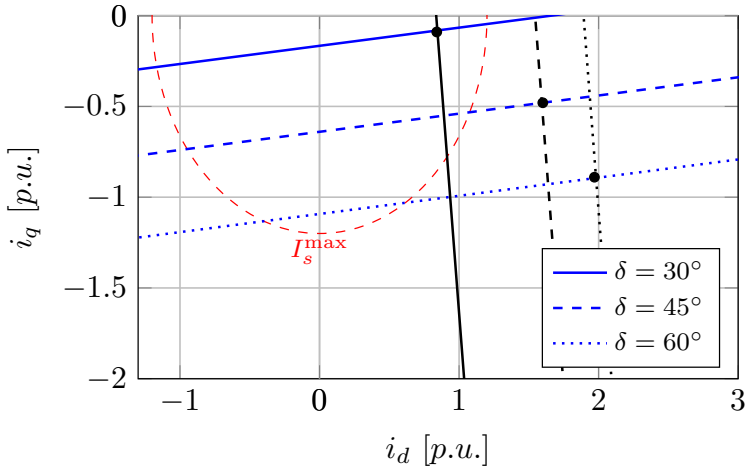


FIGURE 3.6: The changes in the equilibrium point of the voltage controller due to a large APC angle.

To elaborate more on the causes of entering the current-saturation mode from the voltage controller point of view, consider the following equations from Chapter 2:

$$v_d = v_{gd} + Ri_d - \omega L i_q, \tag{3.3}$$

$$v_q = v_{gq} + Ri_q + \omega L i_d. \tag{3.4}$$

The values of i_d and i_q for which $(V_d, V_q) = (V_d^{\text{ref}}, 0)$ is the equilibrium point of the voltage controller. This equilibrium point is the intersection of the lines corresponding to equations (3.3) and (3.4). Figure 3.4 demonstrates how this intersection changes with

minor changes of V_d^{ref}. This intersection is the equilibrium point the voltage controller settles after a brief transient. In case of a severe grid voltage drop, this intersection moves away, as shown in Figure 3.5. The new intersection might be out of the area allowed for the current magnitude. In this situation, the equilibrium of the voltage controller is in the overcurrent area, and the current-saturation mode is activated. Similarly, a large APC angle can also shift this intersection away, depicted in Figure 3.6.

3.3.1 Transiting to the current-saturation mode

A GFM IBR transits from the normal mode to the current-saturation mode if its reference current output exceeds the maximum allowable current $I_s^{\max}$. Since the current controller is fast, it is assumed that the current output is identical to the current reference. In this condition, the current output in the normal operation mode follows (3.2) when the voltage controller settles in its equilibrium point after a brief transient. Since the filter capacitance is small, it can be neglected in calculating the situation in which the GFM IBR enters the current saturation mode. Neglecting this capacitance, the inequality (3.2) is rewritten as [47]:

$$\cos\delta \leq \frac{1}{2}\left(\frac{V_d^{\text{ref}}}{V_g} + \frac{V_g}{V_d^{\text{ref}}} - \frac{(ZI_s^{\max})^2}{V_g V_d^{\text{ref}}}\right), \tag{3.5}$$

where V_d^{ref} is the reference voltage alongside d-axis, V_g is the grid voltage, Z is the grid total impedance, and $I_s^{\max}$ is the maximum allowable output current. If the APC angle exceeds the voltage-dependent threshold in (3.5), the GFM IBR enters the current-saturation mode. This threshold is called the saturation threshold angle in this thesis, and it is computed as

$$\delta_{\text{sat}} := \arccos\left(\frac{1}{2}\left(\frac{V_d^{\text{ref}}}{V_g} + \frac{V_g}{V_d^{\text{ref}}} - \frac{(ZI_s^{\max})^2}{V_g V_d^{\text{ref}}}\right)\right). \tag{3.6}$$

The relation between the saturation threshold angle and grid Thevenin voltage varies for different values of grid total impedance (grid Thevenin impedance plus transformer impedance) according to Figure 3.7. The more the impedance of the grid is, the larger δ_{sat}

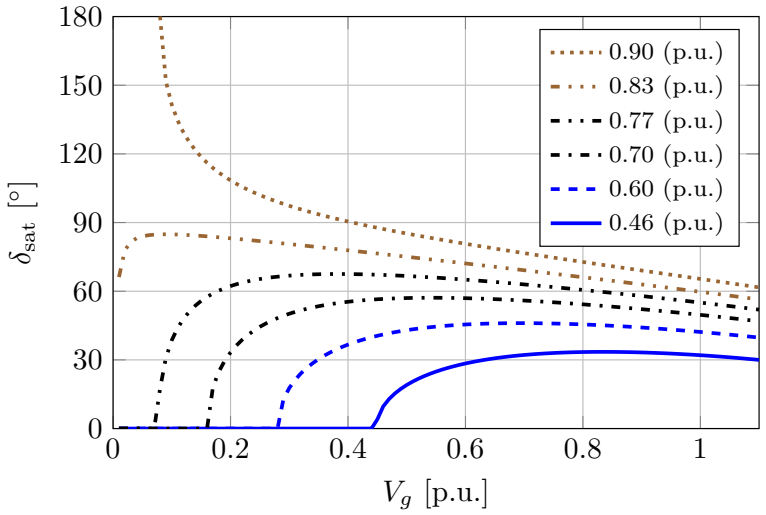


FIGURE 3.7: The variations of the saturation threshold angle with grid Thevenin voltage for different values of the grid total impedance.

is. If the filter capacitance is not neglectable and the grid is inductive, δ_{sat} is calculated as

$$\delta_{\text{sat}} = \arccos\left(\frac{1}{1 - XC\omega_n\omega}\left(\frac{1}{2}\left(\frac{V_g}{V} + \frac{V}{V_g}\right) - \frac{(ZI_s^{\max})^2}{2V_g.V} + \frac{VC^2\omega_n^2\omega^2Z^2}{2V_g} - Z\frac{V}{V_g}C\omega_n\omega\sin\phi\right)\right), \tag{3.7}$$

where C is the filter capacitance, ω_n is the grid nominal angular frequency, and ϕ is the phase angle angle of the grid impedance. The set of APC angles at which the GFM IBR enters the current-saturation mode is defined as the set of entering angles ($\mathcal{S}$) and is expressed as

$$\mathcal{S} = [-180^\circ,\ -\delta_{\text{sat}}] \cup [\delta_{\text{sat}},\ 180^\circ]. \tag{3.8}$$

The set $\mathcal{S}$ is periodic with the same pattern as (3.8) after 180° and before −180°. In (3.8), the part of $\mathcal{S}$ inside $[-180^\circ, 180^\circ]$ is asserted in order to capture extreme events like large negative phase jumps. Besides, for battery connected GFM IBRs, there are scenarios of absorbing active power from the grid, in which APC angle (δ) is negative. Therefore, the operation of GFM IBRs with negative APC angles should be also modelled.

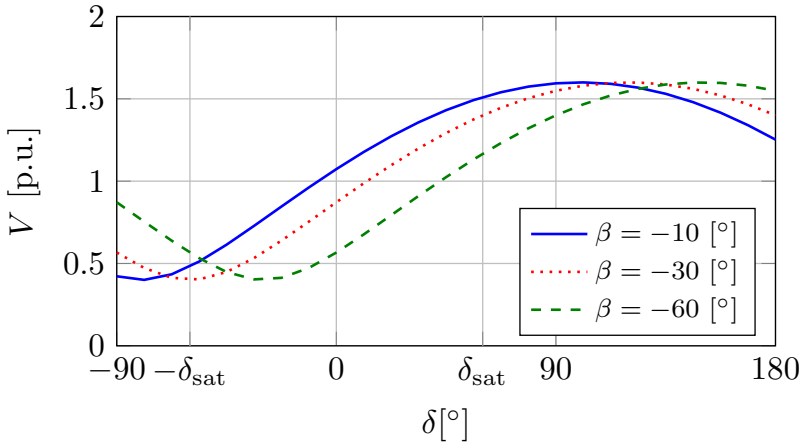


FIGURE 3.8: The voltage variation with the APC angle (δ) for different angles of the saturated current (β).

In the current-saturation mode, the voltage is no longer $(V_d^{\text{ref}}, 0)$. In this situation, the output voltage is

$$V_d^{\text{sat}} = V_g \cos\delta + ZI_s^{\max} \sin(\alpha - \beta), \tag{3.9}$$

$$V_q^{\text{sat}} = -V_g \sin\delta + ZI_s^{\max} \cos(\alpha - \beta). \tag{3.10}$$

It should be noted that in this situation, the voltage controller is deactivated. The output voltage reaches the value of (3.9) and (3.10) once the current controller settles to its steady-state value after a negligible duration of transient.

Since the terminal voltage is no longer on the d-axis of the local reference frame, the APC angle δ, which is the angle between the terminal voltage and the grid's Thevenin voltage in steady-state normal operation, does not have any direct physical meaning in the current-saturation mode. However, the values of voltage alongside d and q directions are functions of δ according to (3.9) and (3.10). These two values also affect the output active power and reactive power. Thus, δ affects electrical variables of the GFM IBR. δ is also a function of the electrical variables because it is the output of the APC, which gets the active power as its input. In this regard, δ highly depends on active power output in the current-saturation mode, which follows

$$P_{\text{sat}} = R(I_s^{\max})^2 + V_g I_s^{\max} \cos(\delta + \beta). \tag{3.11}$$

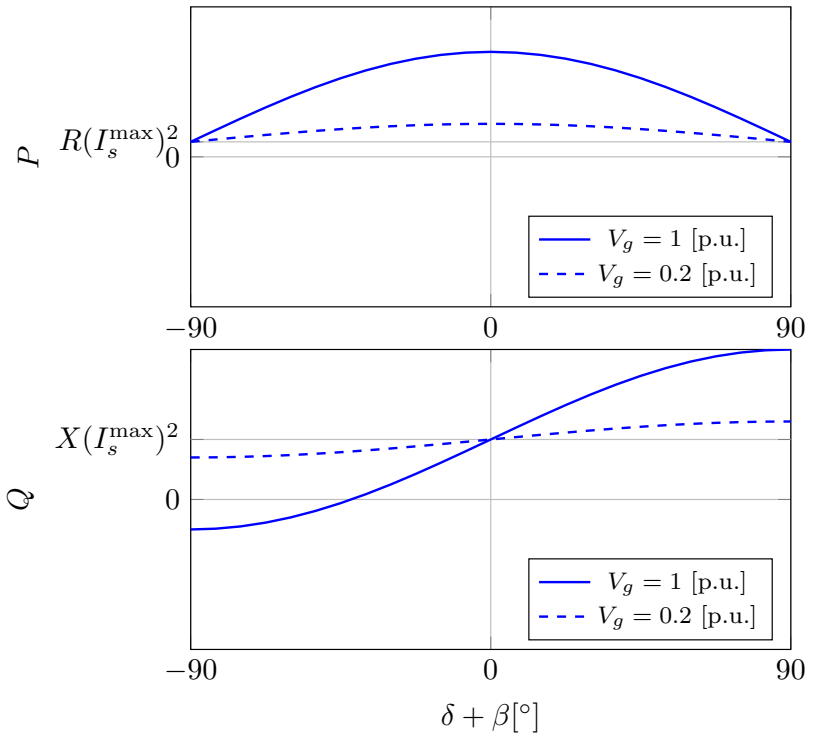


FIGURE 3.9: Active and reactive power output variations with $\delta + \beta$.

Similarly, the reactive power in the current-saturation mode is

$$Q_{\text{sat}} = X(I_s^{\max})^2 + V_g I_s^{\max} \sin(\delta + \beta). \tag{3.12}$$

According to these equations, P_{sat} and Q_{sat} depend on both δ and β. Therefore, the selection of the angle of the saturated current β forms the transient behaviour of GFM IBRs during the current-saturation mode. The magnitude of this voltage depends on both δ and β. Figure 3.8 visualize the variation of the voltage with the APC angle for three different values of β if $I_s^{\max} = 1.2$ [p.u.] and $Z = 0.5$ [p.u.]. It shows there is an adverse over-voltage or an under-voltage for some APC angles. The exact δ range in which these adverse situations happen is a function of β. Notice that for some APC angles in this figure, the GFM IBR might be in the normal operation mode and does not follow the power-angle curve. However, for the sake of comprehensiveness, the complete curve is shown in Figure 3.8. The range of APC angles for which the GFM IBR is in normal operation mode or current-saturation operation mode is explained in Subsection 3.3.2 in detail.

Figure 3.9 shows the variation of active and reactive power with $\beta + \delta$. This figure shows

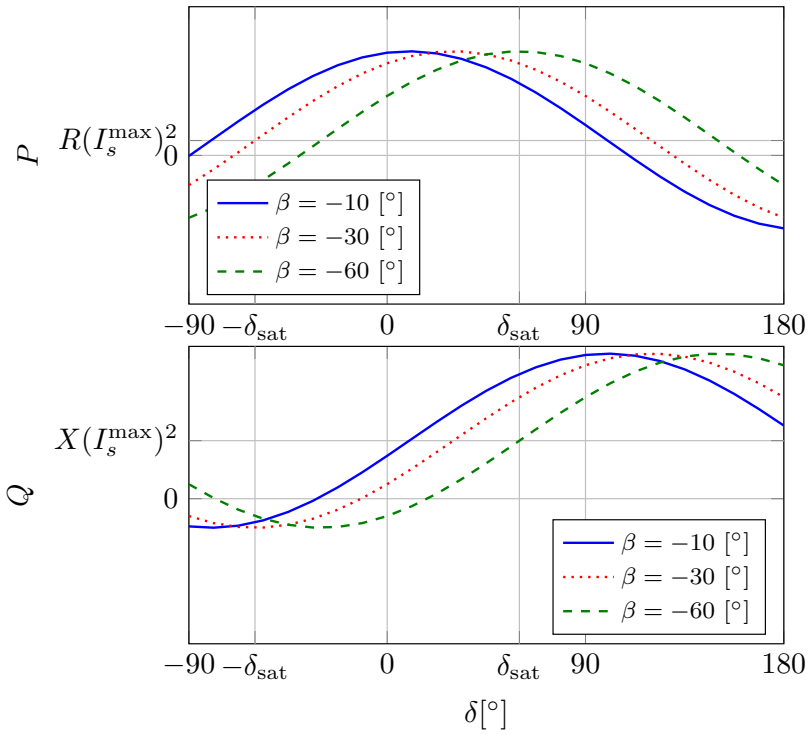


FIGURE 3.10: Active and reactive power output variations with the APC angle.

that if the grid is in its nominal voltage, P and Q have considerable variations with δ around $R(I_s^{max})^2$ and $X(I_s^{max})^2$, respectively. However, if the grid is in a voltage sag situation, active and reactive powers are around $R(I_s^{max})^2$ and $X(I_s^{max})^2$. $R(I_s^{max})^2$ and $X(I_s^{max})^2$ are the active and reactive power consumption of the transformer and the Thevenin impedance of the grid (passive elements). However, since the angle between the Thevenin voltage phasor of the grid and the current output is $\delta + \beta$, the apparent power injecting to the Thevenin voltage phasor is calculated as $V_g I_s^{max} \cos(\delta + \beta) + jV_g I_s^{max} \sin(\delta + \beta)$. The summation of the power injected into the Thevenin voltage phasor and the power consumed by the passive total grid impedance is the power output of the GFM IBR. When there is a deep voltage sag, only the power consumed by the passive Thevenin impedance and transformer is injected from the GFM IBR. In nominal grid voltage, the power injecting into the Thevenin voltage impedance can be significantly larger than that of injecting into passive Thevenin impedance and transformer elements.

Figure. 3.10 shows the variations of power with the APC angle for different selections of β. It shows that the peak of the power-angle curve can be shifted by shifting the β. It highlights the significant effect of selecting the β on the transient stability of grid-forming

converters in the current-saturation mode. Section 3.4 explains this dependency in more detail.

3.3.2 Conditions for returning to the normal operation mode

In the previous sections, the model of a GFM IBR in the current-saturation mode and the situations in which the GFM IBR transitions to the current-saturation mode are explained in detail. However, the necessary conditions for returning to the normal operation mode were not investigated. This section aims to determine these conditions.

The GFM IBR returns to the normal operation mode if the current reference generated by the voltage controller is less than the maximum allowed current. The output current is a function of the APC angle in the post-disturbance current-saturation operation of GFM IBR. Therefore, the condition for returning to the normal operation mode can be restated as the set of angles for which the GFM IBR returns to the normal operation mode. This set, which is called the set of returning angles in this thesis, is defined as

$$\mathcal{R} := \left\{ -180^\circ \leq \delta \leq 180^\circ \mid \left(i_{sd}^{\text{ref}}\right)^2 + \left(i_{sq}^{\text{ref}}\right)^2 \leq (I_s^{\max})^2 \right\}. \tag{3.13}$$

According to Figure 2.8

$$i_{sd}^{\text{ref}} = u_d - yV_q + i_d, \tag{3.14}$$

$$i_{sq}^{\text{ref}} = u_q + yV_d + i_q, \tag{3.15}$$

where u_d and u_q are the outputs of the PI controllers of the voltage control loop as shown in Figure 2.7, y is the shunt capacitance of the filter capacitor, and i_d and i_q are the grid-side current alongside d and q axes. Ignoring the filter's capacitance, the grid-side current is the same as the saturated current, which is $(I_s^{\max}\cos\beta, I_s^{\max}\sin\beta)$. Besides, $y \approx 0$. Therefore,

$$i_{sd}^{\text{ref}} \approx u_d + I_s^{\max}\cos\beta, \tag{3.16}$$

$$i_{sq}^{\text{ref}} \approx u_q + I_s^{\max}\sin\beta. \tag{3.17}$$

Using (3.16) and (3.17), the inequality constraint of (3.13) is rewritten as

$$(u_d + I_s^{\max}\cos\beta)^2 + (u_q + I_s^{\max}\sin\beta)^2 \leq (I_s^{\max})^2. \tag{3.18}$$

This inequality can be further simplified as

$$2u_d I_s^{\max}\cos\beta + 2u_q I_s^{\max}\sin\beta + u_d^2 + u_q^2 \leq 0. \tag{3.19}$$

u_d and u_q, which are the outputs of the voltage control loop's PI controllers, are bounded between $-u_{\max}$ and $u_{\max}$ [42, 43]. Inside these PI controllers, an anti-windup method is implemented to prevent the integrator component from windup [42, 43]. The values of u_d and u_q depend on the voltage error alongside d and q axes. In the current-saturation mode, the voltage control objective is not satisfied, as mentioned in the previous sections. Therefore, voltage errors are non-zero (either positive or negative). When these PI controllers are exposed to a sustained non-zero voltage error, they saturate on either $u_{\max}$ or $-u_{\max}$ depending on the sign of the voltage error. Hence, (3.19) is rewritten as

$$2u_{\max}\,\mathrm{sign}(u_d) I_s^{\max}\cos\beta + 2u_{\max}\,\mathrm{sign}(u_q) I_s^{\max}\sin\beta \leq -2u_{\max}^2, \tag{3.20}$$

which is equivalent to

$$\mathrm{sign}(u_d)\cos\beta + \mathrm{sign}(u_q)\sin\beta \leq -\frac{u_{\max}}{I_s^{\max}}. \tag{3.21}$$

Since $u_{\max} \ll I_s^{\max}$, the right-hand side of this inequality can be considered zero[1]. The left-hand side depends on both β and the signs of u_d and u_q. As explained earlier in this paragraph, u_d and u_q are saturated on either $-u_{\max}$ or $u_{\max}$ depending on the signs of voltage error. Voltage in the current-saturation mode depends on both δ and β according to (3.9) and (3.10). Based on these equations, the signs of u_d and u_q are

$$\mathrm{sign}(u_d) = \mathrm{sign}(V_d^{\mathrm{ref}} - V_d) = \begin{cases} -1 & \text{if } \delta \in [-\delta_d^p(\beta), \delta_d^p(\beta)] \\ 1 & \text{if Otherwise} \end{cases}, \tag{3.22}$$

$$\mathrm{sign}(u_q) = \mathrm{sign}(0 - V_q) = \begin{cases} 1 & \text{if } \delta \in [\delta_q^p(\beta), 180 - \delta_q^p(\beta)] \\ -1 & \text{if Otherwise} \end{cases}, \tag{3.23}$$

[1] Later in this chapter, the calculation of the set of returning angles is extended for a larger value of $u_{\max}$.

where

$$\delta_d^p(\beta) = \arccos\left(\frac{V_d^{\text{ref}} - ZI_s^{\max}\sin(\alpha-\beta)}{V_g}\right), \tag{3.24}$$

$$\delta_q^p(\beta) = \arcsin\left(\frac{ZI_s^{\max}\cos(\alpha-\beta)}{V_g}\right). \tag{3.25}$$

$\delta_d^p(\beta)$ is the maximum APC angle such that $V_d^{\text{ref}} \leq V_d$ for the given β, and $\delta_q^p(\beta)$ is the minimum APC angle such that $V_q \leq 0$ for that given β.

The ranges of β for which the inequality (3.21) holds is summarized in Table 3.1. It is inferred that if $-45° \leq \beta \leq 0°$, $\text{sign}(u_d) \leq 0$ is the sufficient condition, and if $-90° \leq \beta \leq -45°$, $0 \leq \text{sign}(u_q)$ is the sufficient condition for returning to the normal operation mode. Based on (3.22) and (3.23), the set of returning angle is

$$\mathcal{R}(\beta) = \begin{cases} [-\delta_d^p(\beta),\ \delta_d^p(\beta)], & \text{if } \beta \in [-45°, 0°] \\ [\delta_q^p(\beta),\ 180° - \delta_q^p(\beta)], & \text{if } \beta \in [-90°, -45°]. \end{cases} \tag{3.26}$$

Equation (3.26) states that the set of returning angles is a function of β. This set is not necessarily the complement of the set of entering angles $\mathcal{S}$. This is because the transition between the normal mode and the current-saturation mode is discontinuous for CACRS. Thus, the electrical and control variables might significantly jump after the transition. Therefore, it might exhibit non-complementary behavior in these two modes. An APC angle might be inside one of the following four sets with respect to the inclusion in $\mathcal{R}(\beta)$ or $\mathcal{S}$:

- $\delta \in \mathcal{S} - \mathcal{R}(\beta)$: The GFM IBR operates in the current-saturation mode. It is shown as the unfilled hatched area in Figure 3.11, which visualizes sets of entering and returning angles.

	$\text{sign}(u_d) > 0$	$\text{sign}(u_d) < 0$
$\text{sign}(u_q) > 0$	$-90° \leq \beta \leq -45°$	$-90° \leq \beta \leq 0°$
$\text{sign}(u_q) < 0$	$\emptyset$	$-45° \leq \beta \leq 0°$

TABLE 3.1: The sets of β satisfying (3.21)

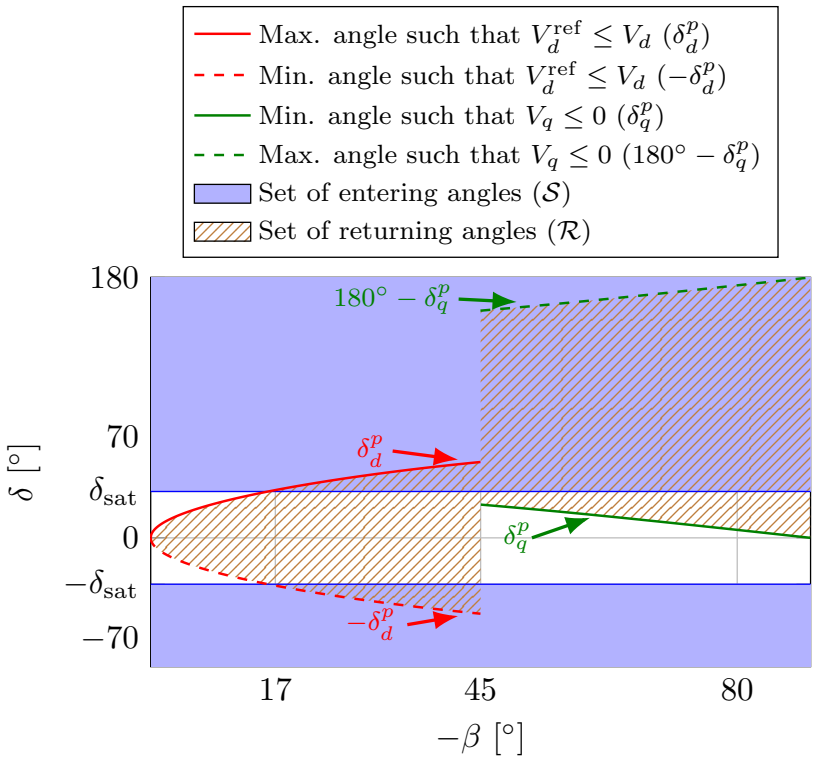


FIGURE 3.11: The sets of entering and returning angles if $Z = 0.46$ p.u. and $X/R = \infty$.

- $\delta \in \mathcal{R}(\beta) - \mathcal{S}$: The GFM IBR operates in the normal operation mode. It is demonstrated as the unhatched solid-filled area in Figure 3.11.
- $\delta \in \overline{\mathcal{R}(\beta) \cup \mathcal{S}}$: The GFM IBR continues operating the mode it is operating without changing to another mode. It is demonstrated as the unhatched unfilled area in Figure 3.11.
- $\delta \in \mathcal{R}(\beta) \cap \mathcal{S}$: The GFM IBR oscillates between the normal operation and current-saturation modes. This set is visualized as the intersection of the solid-filled and hatched area. These mode-oscillations have also been reported in [50] without presenting a mathematical model for the situations in which it happens. The mode-oscillations can be mitigated by the forced saturation, as explained in the following subsection.

3.3.2.1 Mitigating the mode-oscillations using the forced saturation

Mode-oscillations happens when $\delta \in \mathcal{R} \cap \mathcal{S}$. In this situation, as soon as the GFM IBR enters the current-saturation operation mode, the current reference generated by the voltage

controller decreases to a value below the limitation, and the GFM IBR returns to normal operation mode. Then, immediately, the current reference exceeds the limitation, and the GFM IBR re-enters the current-saturation mode. This situation is not preferred because the electrical variables of the GFM IBR also oscillate. Therefore, the GFM IBR should be forced to either of the modes in order to avoid oscillations. Since it is not possible to operate it in the normal operation mode while the current reference exceeds the limitation, it is forced to operate in the current-saturation mode until the conditions for remaining in the normal operation mode are met. To do this, the GFM IBR is forced to stay in the current-saturation mode if $\delta \in \mathcal{S}$. To force the GFM IBR in current saturation mode, the current reference to the current controller is kept as the current saturated reference even though the magnitude of the output of the voltage controller might become temporarily less than $I_s^{\max}$.

An estimation of δ is required for this purpose. The APC angle is estimated as $\tilde{\delta} = -\arctan(\frac{\tilde{v_{gd}}}{\tilde{v_{gq}}})$, where $\tilde{v_{gd}}$ and $\tilde{v_{gd}}$ are estimated according to (3.3) and (3.4) as

$$\tilde{v_{gd}} = v_d - Ri_d + \omega L i_q, \tag{3.27}$$

$$\tilde{v_{gq}} = v_q - Ri_q - \omega L i_d, \tag{3.28}$$

The APC angle is in $\mathcal{S}$ if $\cos\tilde{\delta} \leq \cos\delta_{\text{sat}}$. This equation can be used to determine the condition in which the saturation should be forced. It should be noted that the estimated $\tilde{\delta}$ might have some error. This error might be in the positive or negative direction. Therefore, the forced saturation might either be unable to prevent some oscillations or unnecessarily force staying in the current-saturation mode. To put a conservative margin or to prohibit the unnecessary forced saturation, this inequality changes to $\cos\tilde{\delta} \leq k_m \cos\delta_{\text{sat}}$. If $1 < k_m$, the mitigation is more conservative, meaning forcing staying in the current-saturation mode more than the estimated required forced saturation. If $k_m < 1$, the mitigation is less conservative to avoid unnecessary forced saturation. In this case, brief mode-oscillations are expected.

3.3.3 Sensitivity analyses of the set of returning angles

In the previous section, a closed-form expression for the set of returning angles was derived. This set varies for different values of grid impedance and also larger values of $u_{\max}$. In

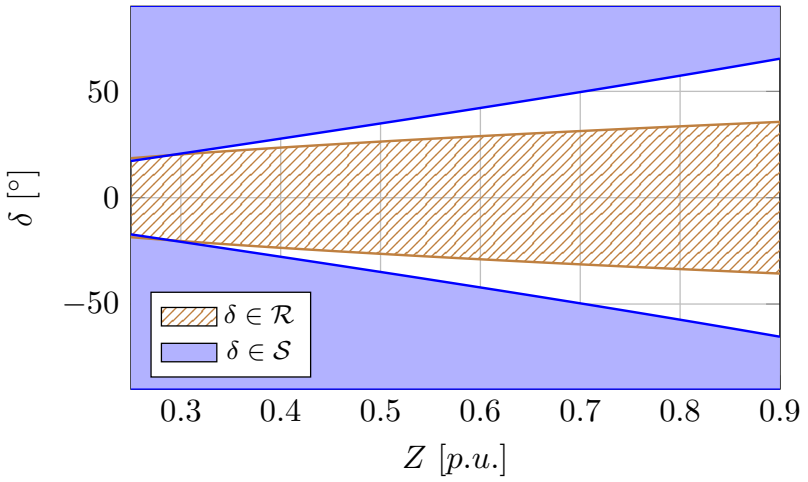


FIGURE 3.12: The variation of sets of entering and returning angles for $\beta = -10°$.

this section, the sensitivity of the set of returning angles to these two parameters is also investigated.

3.3.3.1 Sensitivity to the grid impedance

To examine the effect of grid total impedance on the set of returning angles in nominal grid voltage, this set is calculated for different values of grid impedance and different angles of the saturated current. For $\beta = -10°$ and $\beta = -30°$, the set of returning angles expands for a bigger grid impedance as shown in Figures 3.12 and 3.13. For larger values of the grid total impedance (weak grid connection), the saturation threshold angle becomes larger, and the set of entering angles becomes smaller. Figures 3.12 and 3.13 demonstrate the separation between the sets of entering and returning angles is more significant for weak grids. Therefore, oscillations between the normal and current saturation are less likely to happen if the grid's total impedance is larger.

The inter-dependency between the set of returning angles and the set of entering angles exhibits a different characteristic if $-90° < \beta < -45°$. According to figures 3.14, the set of returning angles for $\beta = -60°$ shrinks for the higher value of the grid impedance. The separation between these two sets is more significant for a larger impedance similar to those of figures 3.12 and 3.13. However, the shrink of the set of returning angles endangers the recovery to the normal operation mode.

To understand the cause of these two contradicting characteristics of the set of returning angles for β more and less than $-45°$, the respected reader is referred to Subsection 3.3.2.

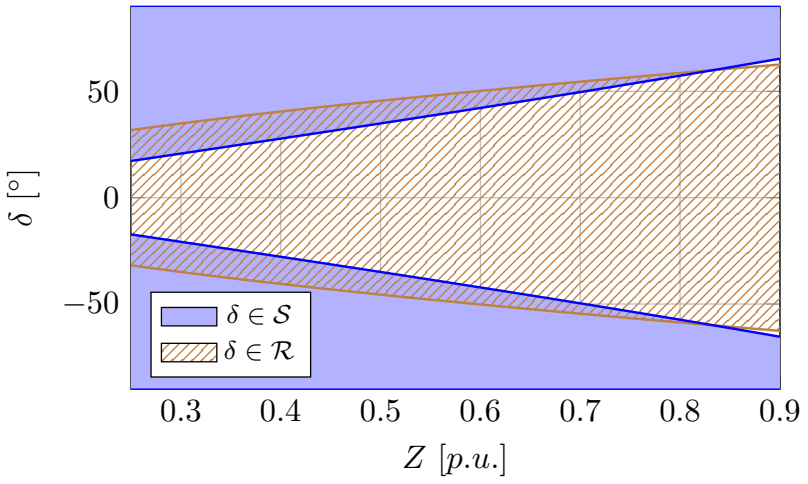


FIGURE 3.13: The variation of sets of entering and returning angles for $\beta = -30°$.

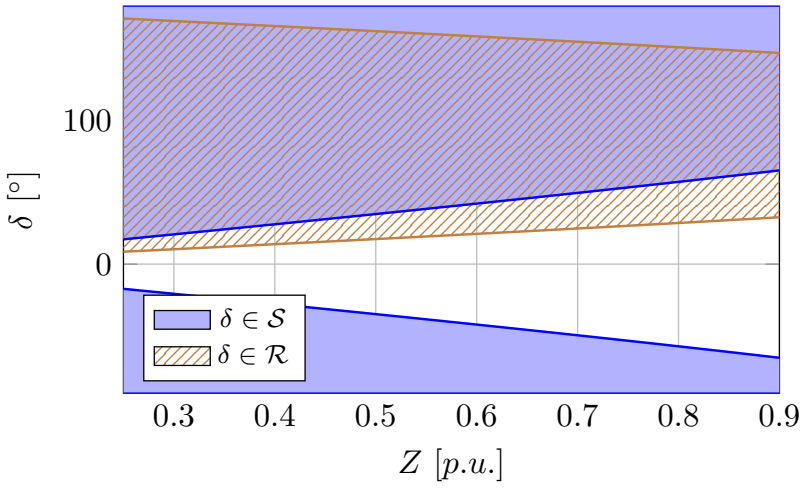


FIGURE 3.14: The variation of sets of entering and returning angles for $\beta = -60°$.

In that subsection, it was mentioned that the set of returning angles is the set of APC angles for which $V_d^{\text{ref}} \leq V_d$ and $V_q \leq 0$ for $-45° \leq \beta \leq 0°$ and $-90° \leq \beta \leq -45°$; respectively. According to (3.9) and (3.10), these two inequality are

$$V_d^{\text{ref}} \leq V_g \cos\delta + ZI_s^{\max} \sin(\alpha - \beta), \tag{3.29}$$

$$-V_g \sin\delta + ZI_s^{\max} \cos(\alpha - \beta) \leq 0. \tag{3.30}$$

These two inequalities can be rewritten as

$$\frac{V_d^{\text{ref}} - ZI_s^{\max}\sin(\alpha-\beta)}{V_g} \leq \cos\delta, \tag{3.31}$$

$$\frac{ZI_s^{\max}\cos(\alpha-\beta)}{V_g} \leq \sin\delta. \tag{3.32}$$

It is evident from (3.31) that the range of δ satisfying the condition for returning to the normal operation mode expands with an increase in Z if $-45^\circ \leq \beta \leq 0^\circ$. However, (3.32) reveals a shrink in this condition with the increase of Z if $-90^\circ \leq \beta \leq -45^\circ$.

3.3.3.2 Sensitivity to the upper limit of voltage PI controller

The set of returning angles, in the previous sections, was calculated based on the assumption that $u_{\max} \ll I_s^{\max}$, and assuming $u_{\max} \approx 0$. In this section, the effect of increasing the value of $u_{\max}$ is investigated. In this case, the inequality of (3.21) for different signs of u_d and u_q is asserted in Table 3.2. The sets of β satisfying the condition of each cells are

$$\mathcal{B}_{11} = [-90^\circ, -45^\circ - \arcsin(\frac{u_{\max}}{\sqrt{2}I_s^{\max}})], \tag{3.33}$$

$$\mathcal{B}_{12} = [-90^\circ, 0^\circ], \tag{3.34}$$

$$\mathcal{B}_{21} = \emptyset, \tag{3.35}$$

$$\mathcal{B}_{22} = [-45^\circ + \arcsin(\frac{u_{\max}}{\sqrt{2}I_s^{\max}}), 0^\circ]. \tag{3.36}$$

Therefore, if $-90^\circ \leq \beta \leq -45^\circ - \arcsin(\frac{u_{\max}}{\sqrt{2}I_s^{\max}})$, then β is in both $\mathcal{B}_{11}$ and $\mathcal{B}_{12}$. Hence, $\delta_q^p(\beta) \leq \delta \leq 180^\circ - \delta_q^p(\beta)$ is the necessary and sufficient condition for returning to the

	$u_d > 0$ (i.e., $\delta \leq -\delta_d^p(\beta)$ or $\delta_d^p(\beta) \leq \delta$)	$u_d < 0$ (i.e., $-\delta_d^p(\beta) \leq \delta \leq \delta_d^p(\beta)$)
$u_q > 0$ (i.e., $\delta_q^p(\beta) \leq \delta \leq 180^\circ - \delta_q^p(\beta)$)	$\cos\beta + \sin\beta \leq -\frac{u_{\max}}{I_s^{\max}}$ $\mathcal{B}_{11}$	$-\cos\beta + \sin\beta \leq -\frac{u_{\max}}{I_s^{\max}}$ $\mathcal{B}_{12}$
$u_q < 0$ (i.e., $\delta \leq \delta_q^p(\beta)$ or $180^\circ - \delta_q^p(\beta) \leq \delta$)	$\cos\beta - \sin\beta \leq -\frac{u_{\max}}{I_s^{\max}}$ $\mathcal{B}_{21}$	$-\cos\beta - \sin\beta \leq -\frac{u_{\max}}{I_s^{\max}}$ $\mathcal{B}_{22}$

TABLE 3.2: The condition for returning to the normal operation mode with a considerable value of $u_{\max}$

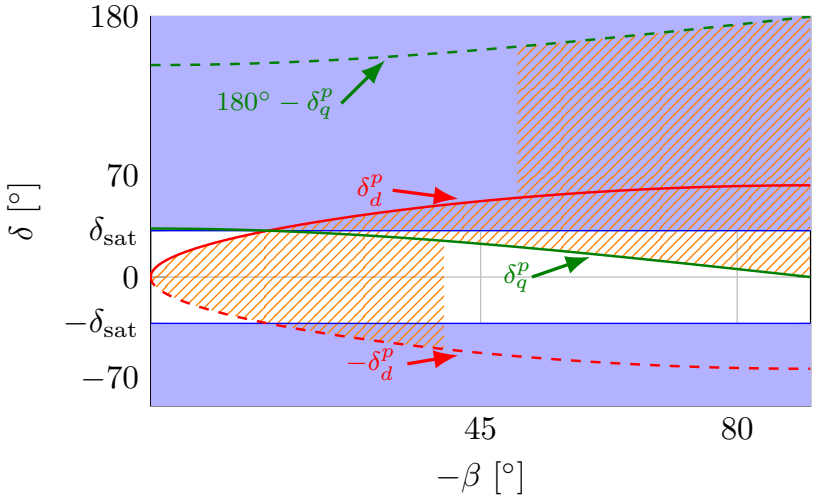


FIGURE 3.15: The set of entering and returning angles demonstrated as the solid filled and hatched area for $\beta' = 5°$.

normal operation mode according to the table 3.2. If $-45° - \arcsin(\frac{u_{\max}}{\sqrt{2}I_s^{\max}}) \leq \beta \leq -45° + \arcsin(\frac{u_{\max}}{\sqrt{2}I_s^{\max}})$, then β is only in $\mathcal{B}_{21}$. Thus, both $\delta_q^p(\beta) \leq \delta \leq 180° - \delta_q^p(\beta)$ and $-\delta_d^p(\beta) \leq \delta \leq \delta_d^p(\beta)$ should be satisfied for returning to the normal operation mode. If $\beta \in [-45° - \arcsin(\frac{u_{\max}}{\sqrt{2}I_s^{\max}}), 0°]$ then β is in both $\mathcal{B}_{22}$ and $\mathcal{B}_{12}$. Thus, $-\delta_d^p(\beta) \leq \delta \leq \delta_d^p(\beta)$ is the condition for returning to the normal operation mode. This can be summarized as:

$$\mathcal{R}(\beta) = \begin{cases} [-\delta_d^p(\beta),\ \delta_d^p(\beta)], & \text{for } \beta \in [-45° + \beta', 0°] \\ [\delta_q^p(\beta), 180° - \delta_q^p(\beta)] \cap [-\delta_d^p(\beta), \delta_d^p(\beta)], & \text{for } \beta \in [-45° - \beta', -45° + \beta'] \\ [\delta_q^p(\beta),\ 180° - \delta_q^p(\beta)], & \text{for } \beta \in [-90°, -45° - \beta']. \end{cases} \quad (3.37)$$

, where $\beta' = \arcsin(\frac{u_{\max}}{\sqrt{2}I_s^{\max}})$.

As $u_{\max}$ increases from zero to $I_s^{\max}$, β' changes from zero to 45°. Therefore, the range of β that is inside the second row of (3.37) becomes bigger. The second row is a tight condition for returning to the normal operation mode. Therefore, the condition for returning to normal operation mode becomes harder to achieve for bigger values of $u_{\max}$. In other words, the interval $[-45° - \beta', -45° + \beta']$ is the set of angles of the saturated current for which both $V_d^{\text{ref}} \leq V_d$ and $V_q \leq 0$ are necessary and sufficient conditions to return to normal operation mode. For the bigger values of β, $V_d^{\text{ref}} \leq V_d$ is the sufficient and necessary condition for returning, and for smaller values of β, $V_q \leq 0$ is the condition for returning to the normal operation mode.

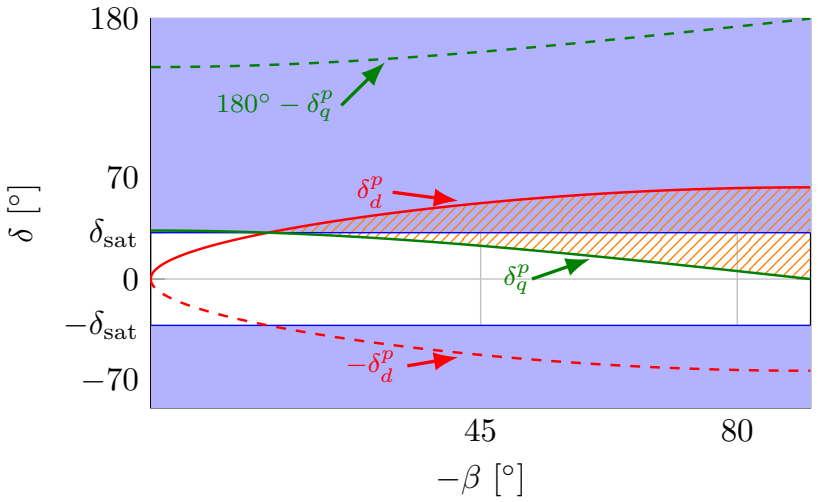


FIGURE 3.16: The set of entering and returning angles demonstrated as the solid filled and hatched area for $u_{\max} = I_s^{\max}$, i.e., $\beta' = 45°$.

Figures 3.15 and 3.16 show the set of returning angles for $\beta' = 5°$ and $\beta' = 45°$; respectively, if $Z = 0.46$ [p.u]. It is observed that the set of returning angles is much tighter in case of a bigger β'. From one point of view, it helps to reduce oscillation between the normal operation and current-saturation operation mode. However, the condition for returning to normal operation mode becomes harder to achieve, which endangers the recovery to the normal operation mode to act as a voltage source. If $u_{\max}$ is too big, the set of returning angles might even become empty for some small values of β. In this case, the GFM IBR will definitely converge to the saturated stable equilibrium point (satSEP), which will be introduced in the next section.

3.4 Effect of Current Saturation on Transient Stability

In the previous sections, the situations in which a GFM IBR enters the current-saturation mode and returns to the normal operation mode have been investigated. It is observed that the power-angle relation changes to (3.11) in the current-saturation operation mode. This relation is in the APC loop according to Figure 3.2. Therefore, the change in the power-angle curve considerably affects the transient stability. Figure 3.17 visualized the power-angle curves for the normal operation mode and current-saturation mode. The power-angle relation is either curves depending on whether $\delta \in \mathcal{S}$ or $\delta \in \mathcal{R}$ as discussed in detail in the section 3.3.2. Neglecting the positive effect of damping, the swing equation,

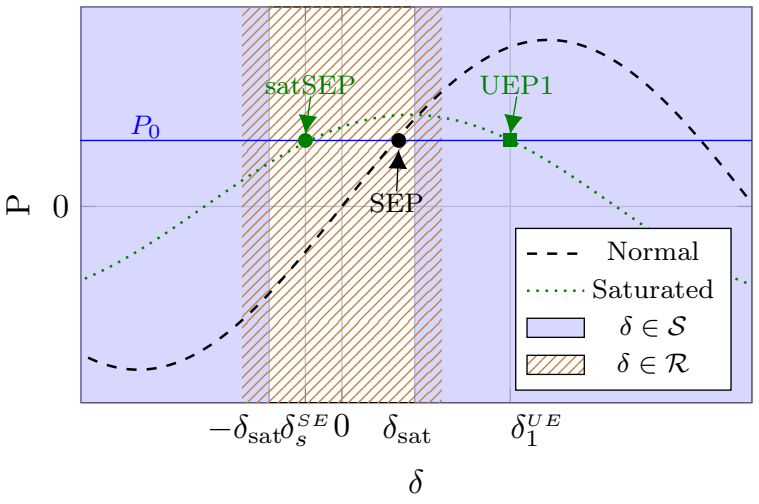


FIGURE 3.17: Power-angle curves in the normal operation mode or the current-saturation mode.

which GFM IBR follows, is [12]

$$P_0 - P(\delta) = 2H\frac{d\omega}{dt}, \tag{3.38}$$

$$\frac{d\delta}{dt} = \omega_n\left(\omega - \omega_0\right). \tag{3.39}$$

Any APC angle that $P(\delta) = P_0$ is an equilibrium point. The swing equation is linearized around an equilibrium point (δ_e) as

$$\frac{d}{dt}\begin{bmatrix}\Delta\delta\\ \Delta\omega\end{bmatrix} = \begin{bmatrix}0 & \omega_n\\ -\dfrac{1}{2H}\left.\dfrac{dP(\delta)}{d\delta}\right|_{\delta_e} & 0\end{bmatrix}\begin{bmatrix}\Delta\delta\\ \Delta\omega\end{bmatrix}. \tag{3.40}$$

The eigenvalues λ follows

$$\lambda^2 = -\frac{\omega_n}{2H}\left.\frac{dP(\delta)}{d\delta}\right|_{\delta_e}. \tag{3.41}$$

If $\left.\dfrac{dP(\delta)}{d\delta}\right|_{\delta_e} < 0$, one of the eigenvalues will be positive, which makes the GFM IBR around δ_e unstable. On the other hand, the eigenvalues are imaginary values when $\left.\dfrac{dP(\delta)}{d\delta}\right|_{\delta_e} > 0$

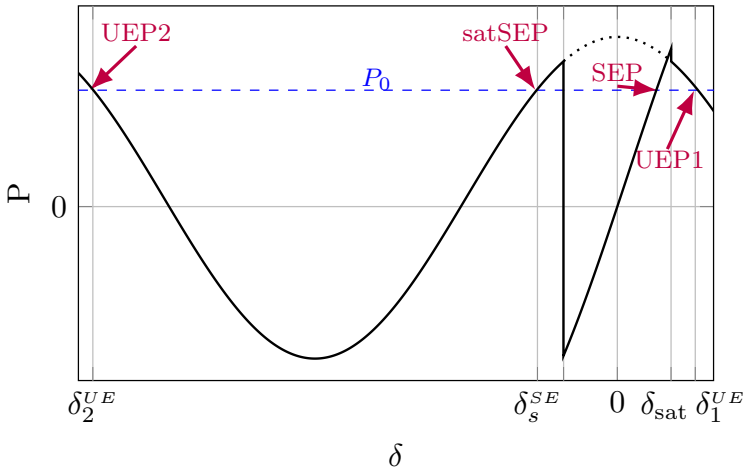


FIGURE 3.18: A visual demonstration of the position of the singular point with respect to the power-angle curve.

positive. Considering the positive effect of damping, the eigenvalues in this case would be complex with negative real parts. Thus, the GFM IBR is stable around δ_e.

The intersections of the power-angle curves with the power reference form the equilibrium points (singular points) sets. If the curve is increasing ($\frac{dP(\delta)}{d\delta}\Big|_{\delta_e} > 0$) at these points, they are stable equilibrium points; otherwise, they are unstable equilibrium points. Figure 3.18 depicts four singular points. In contrast with Figure 3.17, this figure covers a broader range of angles, and also the complexity of $\mathcal{R}$ and $\mathcal{S}$ are not shown in the figure for the sake of ease of understanding. δ_{sat} is the minimum absolute value in the set of entering angles ($\mathcal{S}$). The equilibrium points are as listed:

- Stable equilibrium point (SEP): This is the intersection of the active power reference and the power-angle curve in normal operation mode where the curve is increasing. Convergence to this equilibrium point is desired. It is calculated as

$$\delta^{SE} = \alpha + \arcsin\left(\frac{Z}{V_g V_d^{\text{ref}}}\left(P_0 - \frac{(V_d^{\text{ref}})^2}{Z}\sin\alpha\right)\right), \tag{3.42}$$

  where $\alpha = \arctan\frac{R}{X}$. $\alpha = 0°$ if the grid is inductive.

- Saturated stable equilibrium point (satSEP): This singular point is the intersection of the power reference and the power-angle curve in the current-saturation mode where the curve is increasing. Convergence to this singular point is not desired

because the GFM IBR locks into the current-saturation mode, and the GFM IBR cannot satisfy the voltage control objectives. It is calculated as

$$\delta_s^{SE}(\beta) = -\beta - \arccos\left(\frac{P_0 - R(I_s^{\max})^2}{V_g I_s^{\max}}\right). \tag{3.43}$$

- Unstable equilibrium point 1 (UEP1): This singular point is the intersection of the reference power and the power-angle curve in the current-saturation mode where the curve is decreasing. The GFM IBR becomes unstable if its post-disturbance trajectory passes this angle with a frequency more than the nominal frequency.

$$\delta_1^{UE}(\beta) = -\beta + \arccos\left(\frac{P_0 - R(I_s^{\max})^2}{V_g I_s^{\max}}\right). \tag{3.44}$$

- Unstable equilibrium point 2 (UEP2): According to Figure 3.18, the power-angle curve in the current-saturation mode has two unstable intersections with the reference power (power-angle curve decreasing in the intersection point). One of them is always negative and is located on the left side of the curve. The unstable singular point on the left side of the curve is UEP2. If the GFM IBR's post-fault APC angle trajectory decrease below this equilibrium point, it becomes unstable. The angle of this singular point is calculated as

$$\delta_2^{UE}(\beta) = \delta_1^{UE}(\beta) - 360^\circ. \tag{3.45}$$

  Since the angle of UEP2 is far from the steady-state APC angle, passing this equivalent point is unexpected unless in some adverse situations, such as an adverse connection point phase jump. However, this equilibrium point is mentioned here for the sake of comprehensiveness.

The unstable intersection of the power-angle curve in the normal operation mode is always a large angle. Therefore, it is unlikely that this set is out of the set of entering angles. Therefore, this singular point is not considered in the set of singular points. These equilibrium points repeat themselves every 360°, which is the repeat period of trigonometric functions.

Figure 3.19 shows that if constant angle current reference saturation is implemented, the value of the angle of the unstable equilibrium for the saturated curve (δ_{Sat}^{UE}) is less than those of in unsaturated (δ_{Norm}^{UE}). Besides, the area of deceleration decreases from $A_1 + A_2$

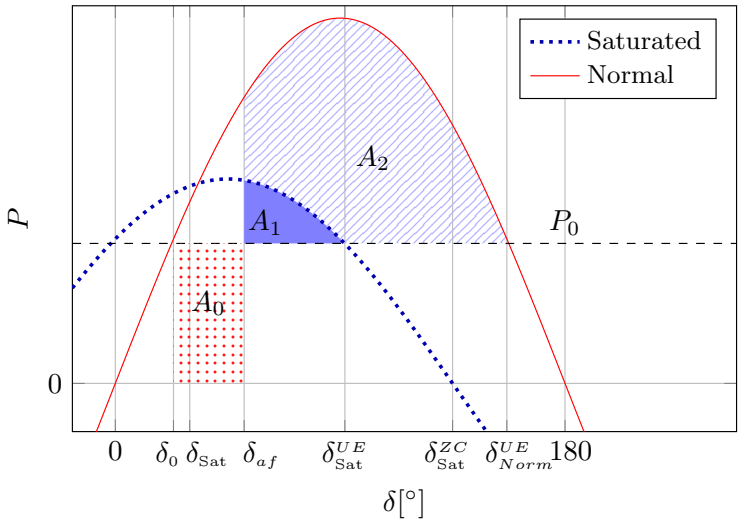


FIGURE 3.19: Deceleration area for the saturated power-angle curve and unsaturated power-angle curve.

to A_1, demonstrated in Figure 3.19. Therefore, the stability margin decreases. A similar conclusion for the circular current limiter is also derived in [31]. The proposed solution for this problem is outlined in Chapter 5.

The other problem is the existence of satSEP and the possibility of converging into it. The next subsection discusses this problem in more detail.

3.5 Circumstances of Converging into Saturated Stable Equilibrium Point

This section explores the circumstances in which a GFM IBR converges to the satSEP. Reference [49] was one of the earliest attempts for this aim. According to [49], if the angle of the satSEP is more than the saturation threshold angle, the GFM IBR might converge into satSEP. In this section, this circumstance is named $\mathcal{C}_1$. It will also be shown in this section that converging to satSEP might be caused by another circumstance as well, namely $\mathcal{C}_2$.

Circumstance $\mathcal{C}_1$ can be broken into two conditions: $\mathcal{C}_{11}$) The angle of satSEP is in the set of entering angles, $\mathcal{C}_{12}$) The post-fault angle and frequency are inside the domain of

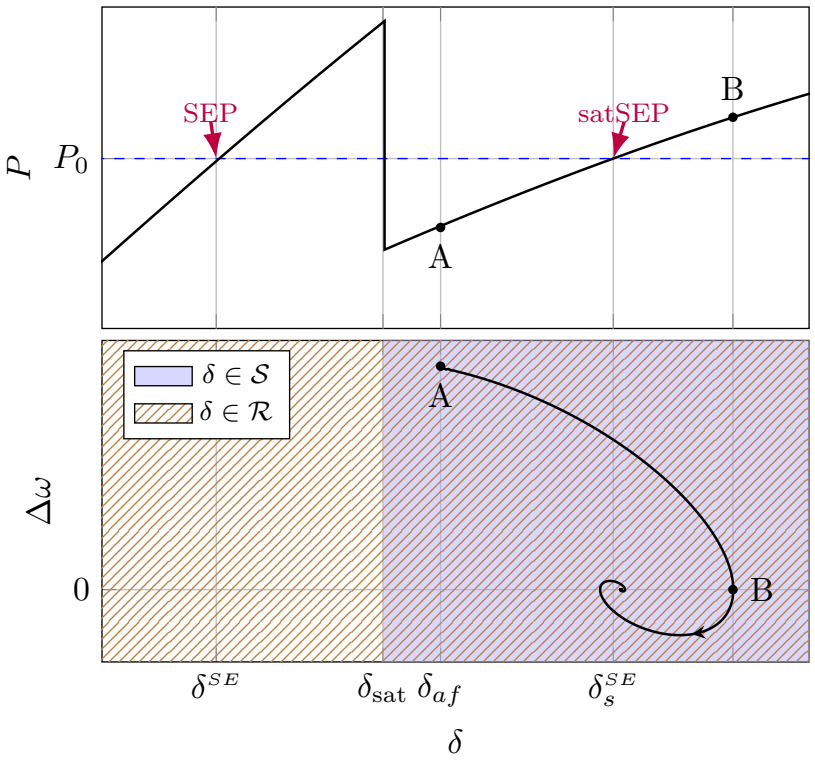


FIGURE 3.20: An example of convergence to the satSEP through $\mathcal{C}_1$.

attraction of satSEP. This circumstance is mathematically asserted as

$$\mathcal{C}_1 : \begin{cases} \delta_s^{SE}(\beta) \in \mathcal{S} & (\mathcal{C}_{11}) \\ (\delta(t_0), \omega(t_0)) \in \text{DOA}(\delta_s^{SE}(\beta), \omega_0) & (\mathcal{C}_{12}) \end{cases} \tag{3.46}$$

where $\mathcal{C}_{11}$ is the static condition, and $\mathcal{C}_{12}$ is the dynamic conditions. In this equation, the variables $\delta_s^{SE}(\beta)$, $\delta(t_0)$, and $\omega(t_0)$, which are the angle of satSEP, and APC angle and frequency right after clearing the fault, are static variables. Inclusion of the static $(\delta_s^{SE}(\beta), \omega_0)$ inside the domain of attraction of the satSEP is a dynamic condition that can be assessed by solving the post-fault trajectory differential equation. Figure 3.20 demonstrate the post-fault trajectory of a GFM IBR that converges to satSEP through $\mathcal{C}_1$. The GFM IBR is on point A right after clearing the fault. Since $P < P0$, the GFM IBR accelerates until reaching the point B. At this point it decelerates until converging to satSEP, which is a stable equilibrium point.

$\mathcal{C}_{11}$ states that the satSEP is included in the set of entering angles, which means that if the GFM IBR's APC angle equals this angle, the GFM IBR will be in the current-saturation mode. On the other hand, if the $\delta_s^{SE}(\beta) \in \mathcal{R}(\beta) - \mathcal{S}$, the GFM IBR operates

at normal operation mode when $\delta = \delta_s^{SE}(\beta)$. As a result, convergence to the satSEP is impossible. However, no certain consequence can be stated about the situation in which $\delta_s^{SE}(\beta) \notin \mathcal{R}(\beta) \cup \mathcal{S}$. In this situation, if the GFM IBR is in current-saturation mode while it is approaching $\delta_s^{SE}(\beta)$, it might converge to satSEP. However, if the GFM IBR is in normal operation mode while passing $\delta_s^{SE}(\beta)$, this angle would not be an equilibrium point for the GFM IBR. Indeed, the transient stability response of the GFM IBR in this situation depends on whether it is in the current-saturation mode or the normal operation mode when it is approaching the angle satSEP. If it approaches the satSEP while it is in the current-saturation mode, the GFM IBR converges to the satSEP.

When $\delta_s^{SE}(\beta) \in \mathcal{S}$, the GFM IBR might converge to satSEP through $\mathcal{C}_1$ explained in the previous paragraphs. On the other hand, $\delta_s^{SE}(\beta) \in \mathcal{R} - \mathcal{S}$, the satSEP is no longer an equilibrium point for the GFM IBR. However, there is no certain outcome for the cases in which $\delta_s^{SE}(\beta) \notin \mathcal{R} \cup \mathcal{S}$ can be foreseen. This work explores the circumstances in which $\delta_s^{SE}(\beta) \notin \mathcal{R} \cup \mathcal{S}$, and the GFM IBR converges into the satSEP. This circumstance happens if the GFM IBR does not return to the normal operation mode during its post-fault trajectory, which is mathematically stated as $\mathcal{C}_{22}$ in (3.47). It should not also become unstable, which means the angle should be contained within the interval $[\delta_2^{UE}(\beta), \delta_1^{UE}(\beta)]$, stated as the condition $\mathcal{C}_{23}$ in (3.47). Therefore, this circumstance, named $\mathcal{C}_2$ here, is summarized as

$$\mathcal{C}_2 : \begin{cases} \delta_s^{SE}(\beta) \notin \mathcal{R}(\beta) \cup \mathcal{S} & (\mathcal{C}_{21}) \\ \delta(t) \notin \mathcal{R}(\beta) - \mathcal{S}, \forall t & (\mathcal{C}_{22}) \\ \delta_2^{UE}(\beta) < \delta(t) < \delta_1^{UE}(\beta), \forall t & (\mathcal{C}_{23}) \end{cases} \tag{3.47}$$

where $\mathcal{C}_{21}$ is the static condition, and $\mathcal{C}_{22}$ and $\mathcal{C}_{23}$ are the dynamic conditions. In this thesis the general description for $\mathcal{C}_{22}$ and $\mathcal{C}_{23}$ is introduced; however, providing the exact differential equations solution for checking $\mathcal{C}_{22}$ and $\mathcal{C}_{23}$ is beyond the scope of this thesis. An example of convergence to satSEP through $\mathcal{C}_2$ is demonstrated in Figure 3.21. The GEM IBR is on point D right after clearing the fault. The APC angle at this point is out of both $\mathcal{R}$ and $\mathcal{S}$. Since the GFM IBR is already in the current-saturation mode, it stays in the current-saturation mode. In this situation, the GFM IBR follows the dotted power-angle curve. The GFM IBR does not enter the set of returning angles while it is converging to satSEP.

The sufficient condition to avoid converging to satSEP is that $\delta_s^{SE}(\beta) \in \mathcal{R}(\beta) - \mathcal{S}$. In this situation, both static conditions $\mathcal{C}_{11}$ and $\mathcal{C}_{21}$ are dismissed. Therefore, both circumstances $\mathcal{C}_1$ and $\mathcal{C}_2$ are dismissed as a result. Notice that this condition is not the necessary condition

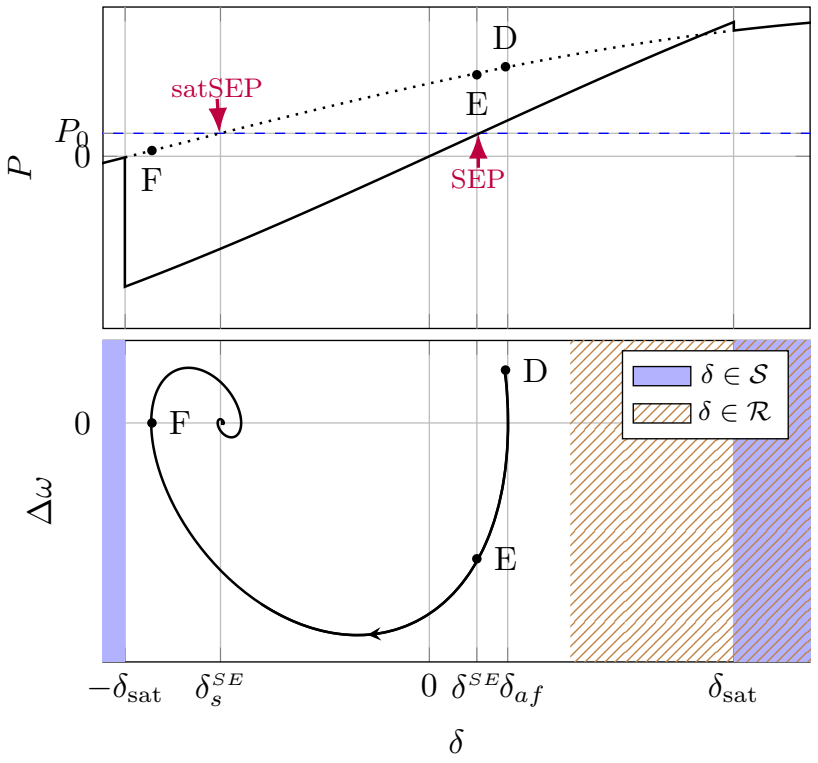


FIGURE 3.21: An example of convergence to the satSEP through $\mathcal{C}_2$.

for avoidance. In other words, there might be numerous cases in which this condition is not satisfied, but the GFM IBR does not converge to the satSEP. An example of these cases is provided in Subsection 3.6.2 in case studies. Adjusting the angle of the saturated current to satisfy the condition is proposed in Chapter 4.

3.6 Results and Discussions

This section examines the analyses and expressions of the previous sections of this chapter through EMT simulations in Simulink/MATLAB [90] environment. The examined system is the system of Figure 2.7 with the parameters and scenarios of Table. 3.3. The system is exposed to different ranges of short and long durations of fault to be examined against a diverse range of scenarios. This system is not equipped with a virtual impedance, and the effect of the reactive power controller is not simulated. Therefore, V_d^{ref} is the constant value of 1 [p.u.]. The rationale behind neglecting existence of any virtual impedance is to fully investigate the effect of CACRS before combining it with a virtual impedance as a future research. Since V_d^{ref} is usually bounded within a tight limit, assuming $V_d^{\text{ref}} = 1$ [p.u.]

is a valid approximation though not being exact. The simulation uses a detailed EMT model containing all inner loop models in the Simulink/MATLAB Simscape environment. The results of the simulations are compared against the mathematical model derived in this chapter for the sake of verification.

The GFM IBRs are parallel in the same bus, with an equivalent share of active and reactive loading and identical parameters. Therefore, they are modeled as an equivalent GFM IBR according to [3]. The GFM IBR farm is connected to a grid with the Thevenin impedance of 0.3 p.u. and X/R ratio of 20 through a transformer with the impedance of 0.16 p.u. (totally, the connection impedance of $Z = 0.46$ p.u.). Ten cases, listed in Table 3.4 are simulated to examine the transient stability behavior in different operation points, disturbance magnitudes, and different GFM IBR parameter settings. In these cases, the simulated system is exposed to three-phase short-circuit fault disturbances. These disturbances are modeled as voltage drops of 0.95 p.u. with the duration shown in Table 3.4 until reaching the post-fault angle δ_{af}.

These cases are clustered into four groups:

- Cases A, B, and C are compared to each other to examine how the selection of β affects the transient stability (Subsection 3.6.1).
- Cases D and E are compared to each other to showcase the risk of converging into the satSEP if $\delta_{af} \notin \mathcal{R}(\beta) \cup \mathcal{S}$. $\beta = -60°$ is for both cases, but δ_{af} is different (Subsection 3.6.2).
- Cases F, G, and H are compared to show the shrink in the domain of attraction due to the current limitation. The GFM IBR's parameters are the same for both F and G cases. Case F is exposed to a longer duration of the fault compared to case G. In Case H, no current limitation mechanism is implemented, and it is exposed to a longer duration of the fault compared to Cases F and G. In reality, Case H cannot be implemented because of the inverter's current limitation. However, it is simulated in Subsection 3.6.3 to confirm the analyses of Section 3.4 about the transient stability margin decrement due to the current limitation.
- Cases I and J are compared together. The GFM IBR is identical for both of these two cases. However, $u_{\max}$ is different. For case J, $u_{\max}$ is so large that β located in $[-45° - \beta', -45° + \beta']$. In this situation, the condition for returning to normal operation becomes tighter (Subsection 3.6.4).

Param.	*Values*	*Units*	*Descriptions*
S_b	310	MVA	Nominal apparent power
V_b	400	V	Nominal Voltage
V_{dc}	1200	V	DC link voltage
n	816	-	Number of identical parallel GFM IBRs
f_n	60	Hz	Nominal frequency
D_p	0.03	p.u.	Active droop coefficient
H	2	p.u.	Virtual inertia
$\Delta\omega_{\max}$	0.0066	p.u.	Maximum frequency deviation
V_d^{ref}	1	p.u.	Voltage reference magnitude
I_s^{max}	1.2	p.u.	Maximum allowed current
X_{tr}	0.16	p.u.	Total reactance of transformer windings

TABLE 3.3: Parameters of the simulated GFM farm.

Case	P_0	*Fault duration [ms]*	δ_0[°]	δ_{af}[°]	β[°]	$\mathcal{R}$[°]	$u_{\max}$ [p.u.]	β'[°]
A	270 MW (0.87 p.u.)	100	23.38	34.93	**-6**	**[-23.14, 23.14]**	0.063	2.55
B	270 MW	100	23.38	34.93	**-30**	**[-45.2, 45.2]**	0.063	2.55
C	270 MW	100	23.38	34.93	**-90**	**[-1.3,181.3]**	0.063	2.55
D	62 MW (0.2 p.u.)	**600**	5.23	**44.76**	-60	[14.84, 165.16]	0.063	2.55
E	62 MW	**100**	5.23	**7.93**	-60	[14.84, 165.16]	0.063	2.55
F	270 MW (0.87 p.u.)	**290**	23.38	**62.01**	-30	[-45.2, 45.2]	0.063	2.55
G	270 MW	**330**	23.38	**67.71**	-30	[-45.2, 45.2]	0.063	2.55
H	270 MW	**400**	23.38	**76.10**	**No current saturation implemented**			
I	62 MW	40	5.23	5.65	-30	**[-45.2, 45.2]**	**0.063**	**2.55**
J	62 MW	40	5.23	5.65	-30	**[27.8, 45.2]**	**0.6**	**25.10**

TABLE 3.4: The list of simulated cases. Fields in bold are the parameters that vary in each comparison set.

The total impedance is the same for these cases. Hence, $\mathcal{S} = [-180°, -32.0455°] \cup [32.0455°, 180°]$ for all cases except Case H, for which no current limitation method is implemented. Detailed analyses of the cases are discussed in the following.

3.6.1 Effect of the angle of the saturated current

Figure 3.22 confirms that the current saturation mechanism is successful in limiting the inverter's output current to 1.2 p.u. for the Cases A, B, and C. Cases A and B converge to the stable equilibrium point; however, Case C converges to the saturated stable equilibrium point. Case B exhibits the faster convergence to the stable equilibrium point than Case A, as shown in Figure 3.23(i). In Case C, $\delta_s^{SE}(\beta_{\text{C}}) = 44.52° \in \mathcal{S}$, and the post-fault angle is inside the satSEP's DOA. Therefore, the GFM IBR converges to satSEP through

$\mathcal{C}_1$ explained in Subsection 3.5. In this case, the GFM IBR does not return to normal operation mode, and the voltage control objectives are missed, as shown in Figure 3.23(iii).

In Case A, $\mathcal{R}(\beta_{\mathrm{A}}) = [-23.14°, 23.14°]$ according to (3.26), and $\mathcal{S} = [-180°, -32.0455°] \cup [32.0455°, 180°]$ similar to other cases. The post-fault angle $\delta_{af} = 34.93°$ (at $t = 0.15$ s) is inside $\mathcal{S} - \mathcal{R}(\beta_A)$. Hence, the GFM IBR remains in the current-saturation mode until the APC angle enters $\mathcal{R}(\beta_A)$. Though the GFM IBR exist $\mathcal{S}$ at $t = 0.435$ s, shown as the point a_1 in Figure 3.22 and Figure 3.23, it remains in the current-saturation mode as it has not entered $\mathcal{R}(\beta_A)$ yet. In this situation, the GFM IBR enters $\overline{\mathcal{R}(\beta_{\mathrm{B}}) \cup \mathcal{S}}$, in which it retains its mode, i.e., the current-saturation mode. It returns to normal operation mode after entering to $\mathcal{R}(\beta_{\mathrm{A}}) - \mathcal{S}$ at $t_{a_2} = 0.517$ s, depicted as the point a_2 in Figure 3.22 and Figure 3.23. At this point, the APC angle becomes less than 23.14°. It re-enters $\overline{\mathcal{R}(\beta_{\mathrm{B}}) \cup \mathcal{S}}$ at $t_{a_3} = 0.742$ s, shown as a_3 in Figure 3.22 and Figure 3.23. It continues operating in its normal operation mode. It never again re-enters $\mathcal{S}$ during its post-fault transient. Thus, it remains in the normal operation mode, and it converges to the SEP.

In Case B, the set of returning angles $\mathcal{R}(\beta_{\mathrm{B}}) = [-45.20°, 45.20°]$. Therefore, mode oscillations are expected while $\delta \in \mathcal{R}(\beta_{\mathrm{B}}) \cap \mathcal{S} = [32.0455°, 45.20°]$, which contains the post-fault

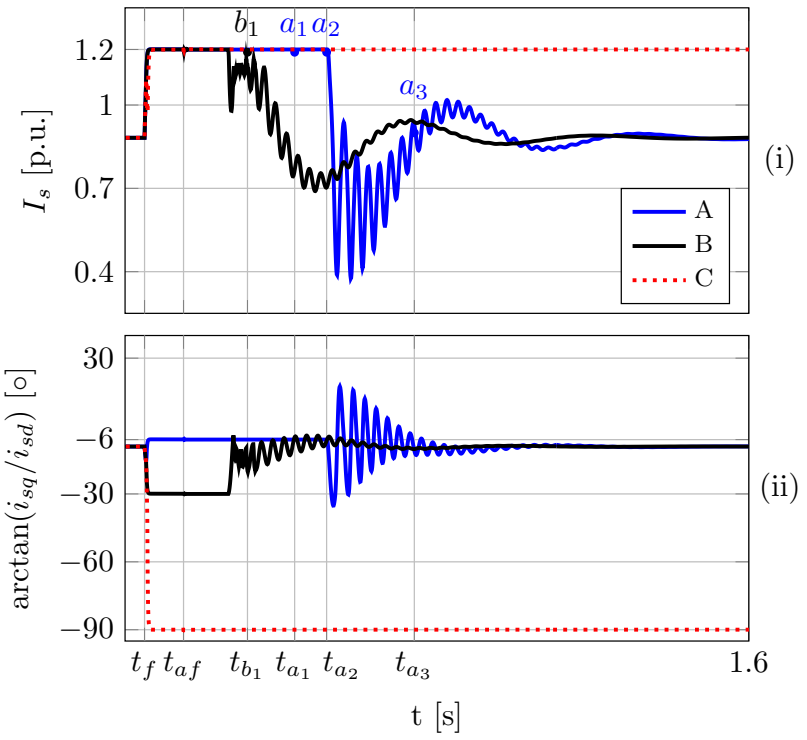


FIGURE 3.22: Simulation results for the currents in Cases A, B, and C.

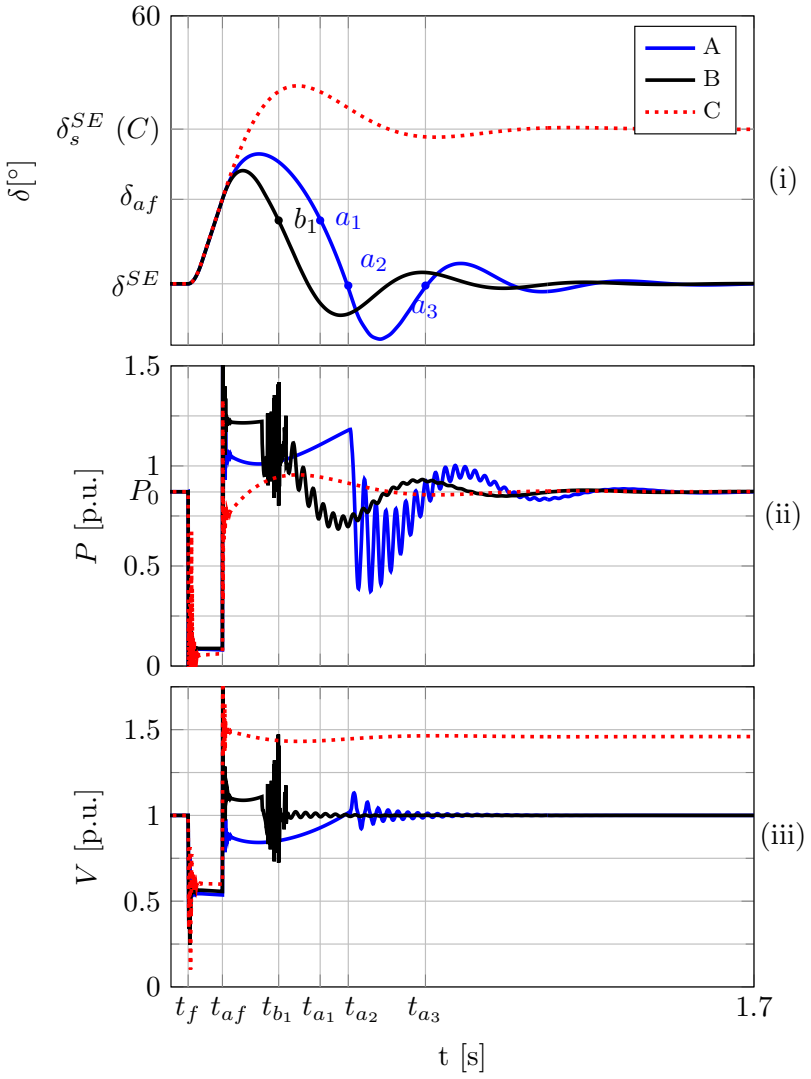


FIGURE 3.23: Simulation results for the angles in Cases A, B, and C.

angle $\delta_{af} = 34.93°$. The oscillations are reduced by forced saturation with $k_m = 0.95$ explained in Subsection 3.3.2.1. The GFM IBR returns to normal operation mode, and the voltage control functionality activates from $t_{b_1} = 0.314$ s, shown as the point b_1 in Figure 3.22 and Figure 3.23. At this point, the GFM IBR enters $\mathcal{R}(\beta_B) - \mathcal{S}$.

3.6.2 Convergence to satSEP through $\mathcal{C}_2$

For cases D and E, the set of returning angles is $[14.83°, 165.1604°]$. The post-fault APC angle is 44.76° for Case C, which is within $\mathcal{S} \cap \mathcal{R}$ (oscillations are mitigated with $k_m = 0.95$ according to Subsection 3.3.2.1). The GFM IBR returns to the normal operation mode

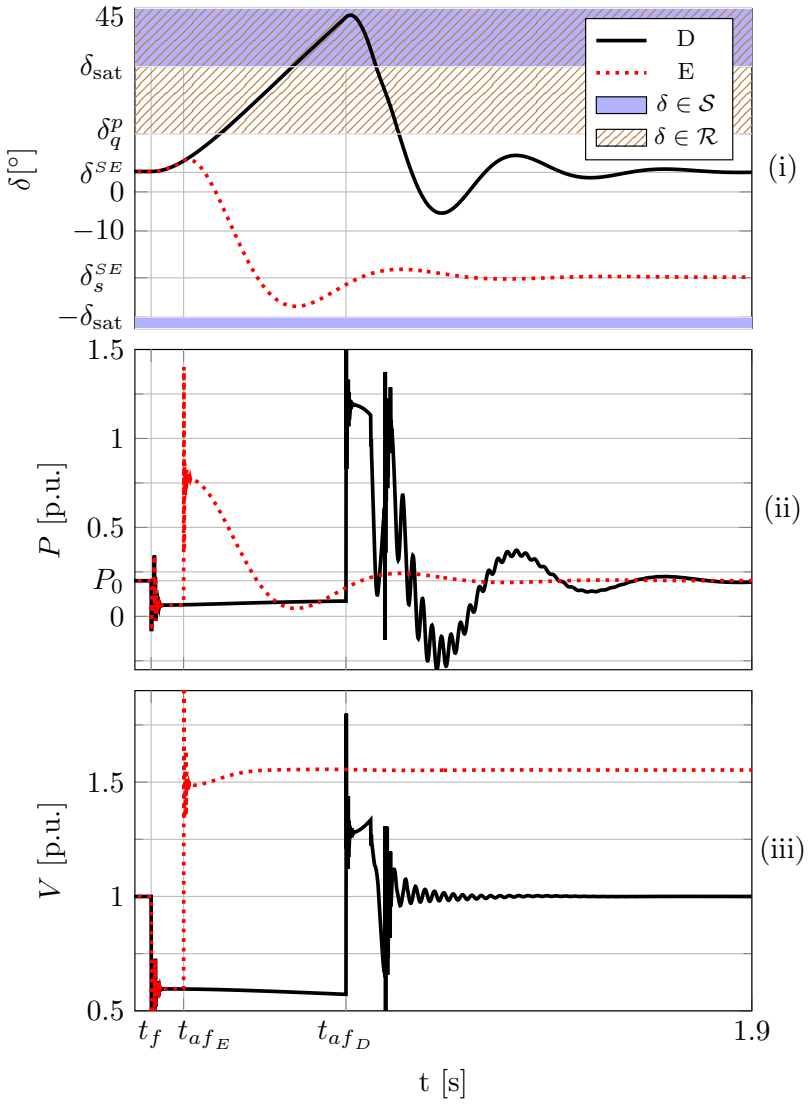


FIGURE 3.24: Simulation results for the angles in Cases D and E.

after a brief oscillation and, then, converges to the SEP as shown in Figure 3.24. However, in Case E, the post-fault angle is $\delta_{af} = 7.93° \in \overline{\mathcal{R}(\beta_{\text{E}}) \cup \mathcal{S}}$. Therefore, it continues operating in the current-saturation mode, in which it was during the fault disturbance. Since the power output in the current-saturation mode is more than the power reference at this APC angle, the APC angle decreases until it settles at the satSEP $\delta_s^{SE} = -22.00°$, which is out of $\mathcal{S}$, as shown in Figure 3.24. Figure 3.24 depict that in both Cases D and E, the active power output equals the power reference in the steady-state. However, the voltage regulation objective is not met in Case E in contrast to Case D. Figure 3.25 also depicts that Case E locks into the current-saturation mode. The disturbance in Case E is smaller than the disturbance in Case D. However, the consequence of Case E is undesired

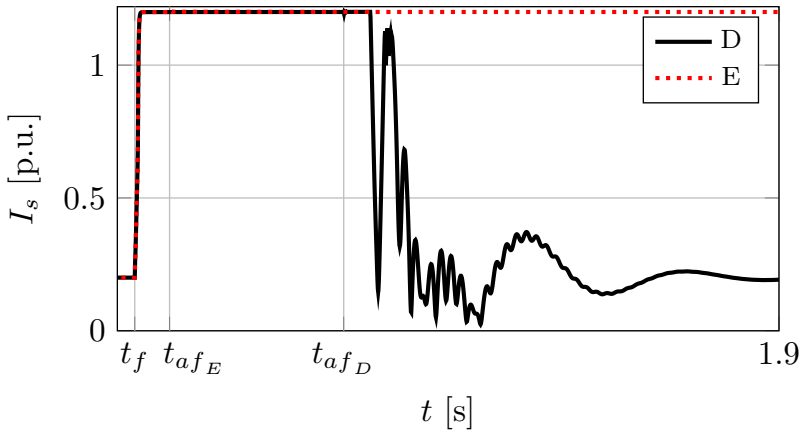


FIGURE 3.25: The currents in Cases D and E.

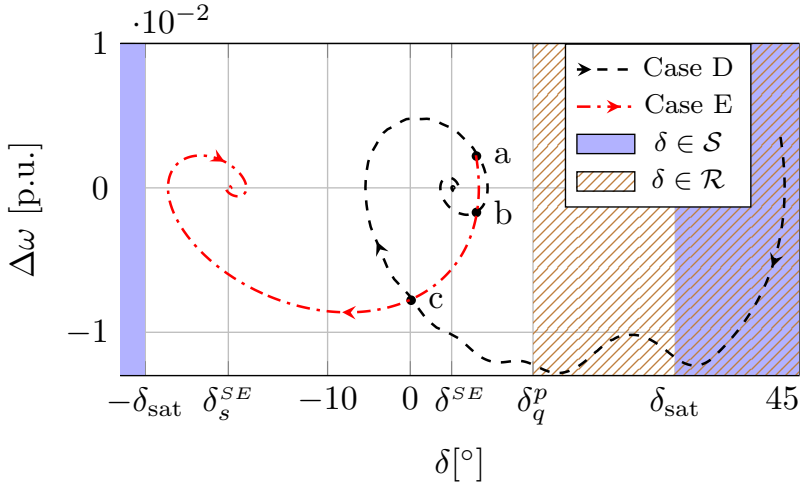


FIGURE 3.26: Post-fault trajectories of the GFM IBR in Cases D and E where the solid area and hashed area correspond to the set of entering and returning angles, respectively.

in contrast to Case D, which is asymptotically stable and converges to the SEP. Hence, it is observed that if the GFM IBR operates in a light loading, a wrong selection of β might lead to locking into the current-saturation mode after short disturbances. Case D is an example that the sufficient condition for avoiding convergence to the satSEP ($\delta_s^{SE}(\beta) \in \mathcal{R} - \mathcal{S}$) is not satisfied, but the GFM IBR does not converge to the satSEP.

Notice that in both Cases C and E, the GFM IBR settles at the satSEP; however, different factors contribute to convergence into the satSEP in these cases. The angle of satSEP $\delta_s^{SE} \in \mathcal{S}$ in Case C (condition $\mathcal{C}_{11}$ in Section 3.5). However, it is out of $\mathcal{S}$ in Case E. Therefore, the circumstance $\mathcal{C}_1$ cannot be the cause of locking into the current-saturation mode. The GFM IBR locks into the current-saturation mode because of the circumstance

$\mathcal{C}_2$. Figure 3.26 further clarifies why circumstance $\mathcal{C}_2$ is the cause of the convergence to the satSEP in Case E. According to this figure, $\delta_s^{SE} \notin \mathcal{S} \cup \mathcal{R}(\beta_E)$, which is condition $\mathcal{C}_{21}$. During the whole post-fault trajectory, the GFM IBR does not enter $\mathcal{R}(\beta_E)$ (condition $\mathcal{C}_{22}$). The GFM IBR does not pass any unstable equilibrium point (condition $\mathcal{C}_{23}$).

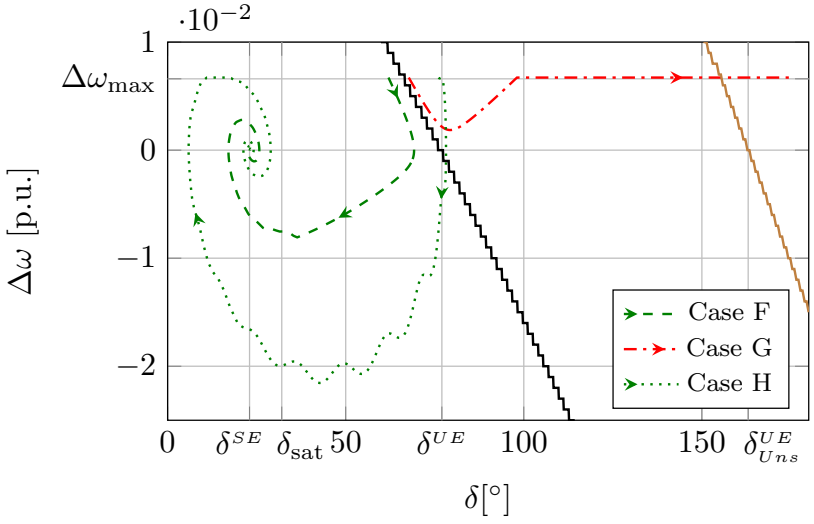


FIGURE 3.27: Post-disturbance trajectories in Cases F, G, and H. Black line and brown line are the borders of DOAs for a GFM equipped and not equipped with CRS; respectively.

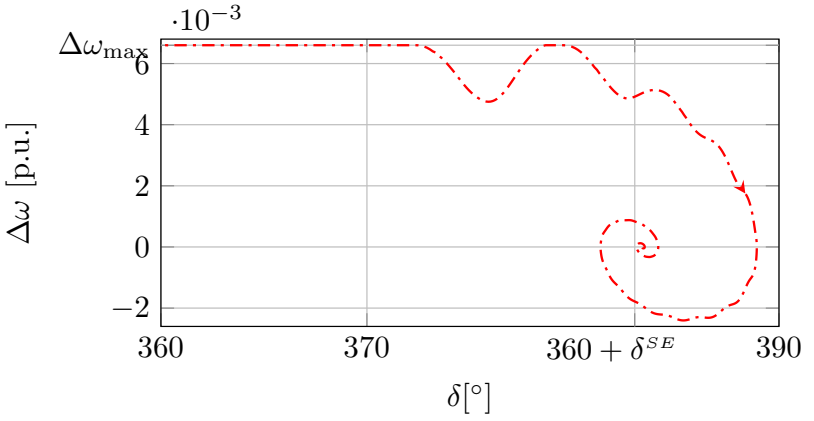


FIGURE 3.28: Trajectory of Case G until convergence to the next SEP after passing the positive unstable equilibrium point.

3.6.3 Shrink in stability DOA due to current saturation

The simulations of cases F and G confirm that the computationally calculated black line is the border of the transient stability domain of attraction according to Figure 3.27. In case F, the post-fault $(\delta_{af_F}, \Delta\omega_{af_F})$ are inside the DOA. As a result the GFM IBR is stable. For case G, the post-fault $(\delta_{af_G}, \Delta\omega_{af_G})$ is out of the DOA border, and the GFM IBR is unstable. Figure 3.28 depicts that the GFM IBR converges to the next SEP $(360° + \delta^{SE}, 0)$ after passing the positive unstable equilibrium point in Case G. Even though theoretically, it is a stable case, this situation is not desired because the GFM IBR absorbs a huge amount of active power from the grid until it reaches the next SEP. Figure 3.29 shows that the GMF IBR absorbs energy from the grid from point g_1 around $t_{g_1} = 0.974$ s until point g_2 around $t_{g_2} = 2.219$ s.

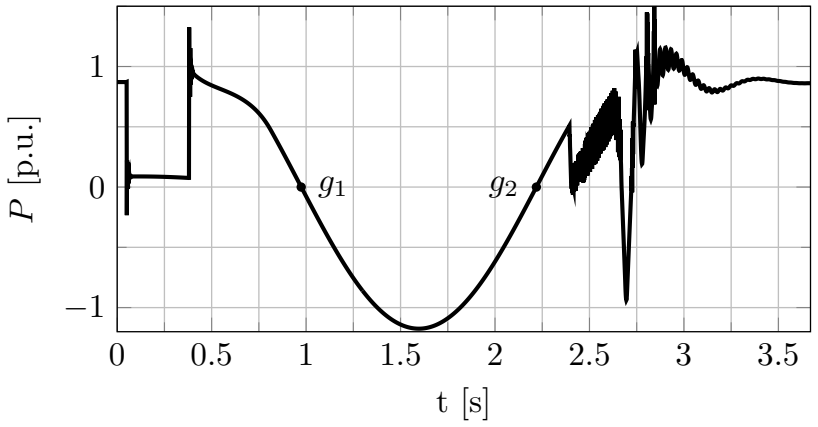


FIGURE 3.29: Post-fault active power in Case G.

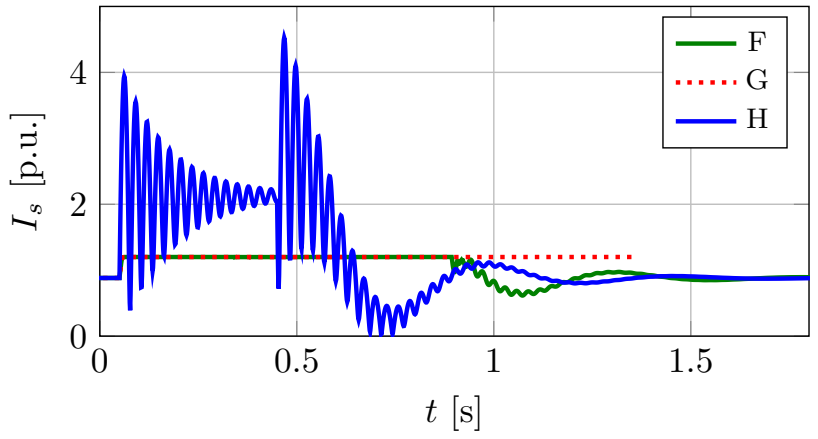


FIGURE 3.30: Post-disturbance current of the GFM IBR in Cases F, G, and H.

The border of DOA in the saturated cases (black line) is closer to the SEP than the border of unsaturated cases, i.e., the brown line in Figure 3.27. These borders are calculated numerically using the swing equation for estimating the post-fault trajectories. Case H reveals that even though the post-fault angle in case H is larger than case G, the GFM IBR converges to SEP in the absence of a current limitation mechanism. On the other hand, Figure 3.30 shows that a significant overcurrent occurs in case H. Therefore, the lack of a current limitation mechanism might cause serious damage to the inverter, although the current limitation shrinks the DOA.

3.6.4 Effect of the voltage controller limiter

In the previous paragraphs, the effect of current saturation and the angle of the current saturation on the post-fault transient stability were examined through simulations. In this paragraph, the effect of $u_{\max}$ value on the transient stability is examined. For this purpose, Cases I and J are compared. As listed in Table 3.4, $u_{\max}$ for these two cases are 0.063 and 0.6, respectively. Therefore, $\beta' = \arcsin \frac{u_{\max}}{\sqrt{2} I_s^{\max}}$ for these two cases are

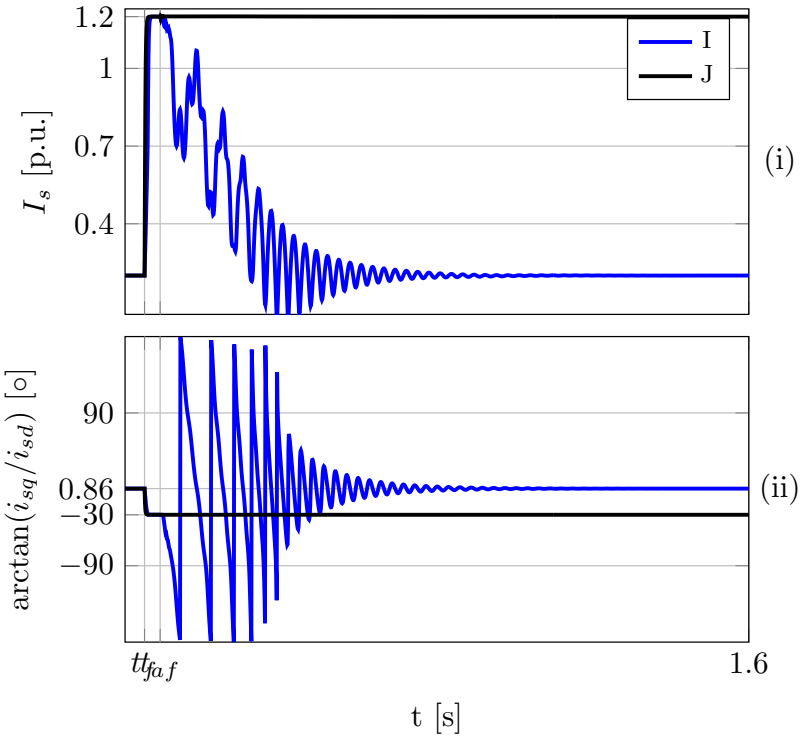


FIGURE 3.31: Output current in Cases I and J.

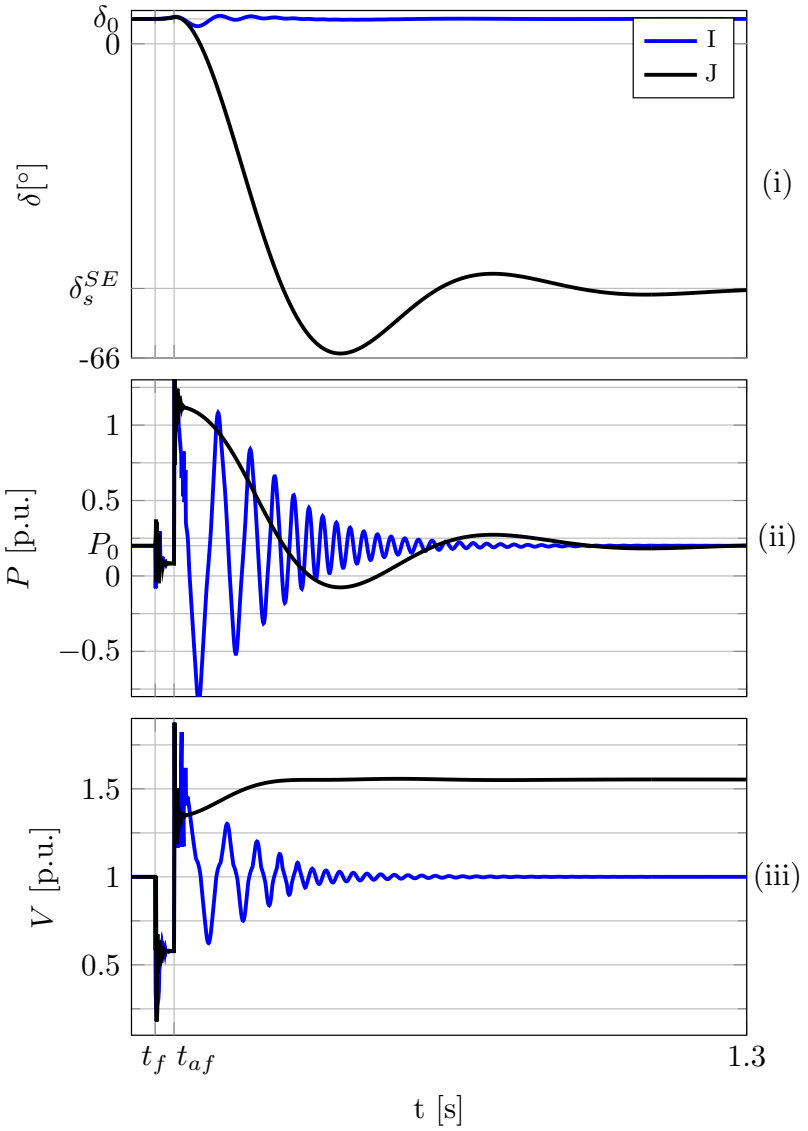


FIGURE 3.32: APC angle, output power, and the terminal voltage in Cases I and J.

2.55° and 25.1°, respectively. According to (3.37), $\mathcal{R}(\beta = -30°)$ for these two cases are $[-\delta_d^p(\beta),\ \delta_d^p(\beta)] = [-45.2°, 45.2°]$ and $[\delta_q^p(\beta), 180° - \delta_q^p(\beta)] \cap [-\delta_d^p(\beta), \delta_d^p(\beta)] = [27.8°, 45.2°]$.

In case I, the post-fault angle $\delta_{af} = 5.64°$ is inside the set of returning angle. Therefore, it returns to the normal operation mode immediately after the fault, as shown in Figure 3.31. Figure 3.32 shows that the angle converges to the SEP with a very brief transient. There are more voltage and power oscillations until converging to the set point because of the voltage control's transient. Figure 3.33 also confirms that the GFM IBR in Case I is stable and converges to the SEP.

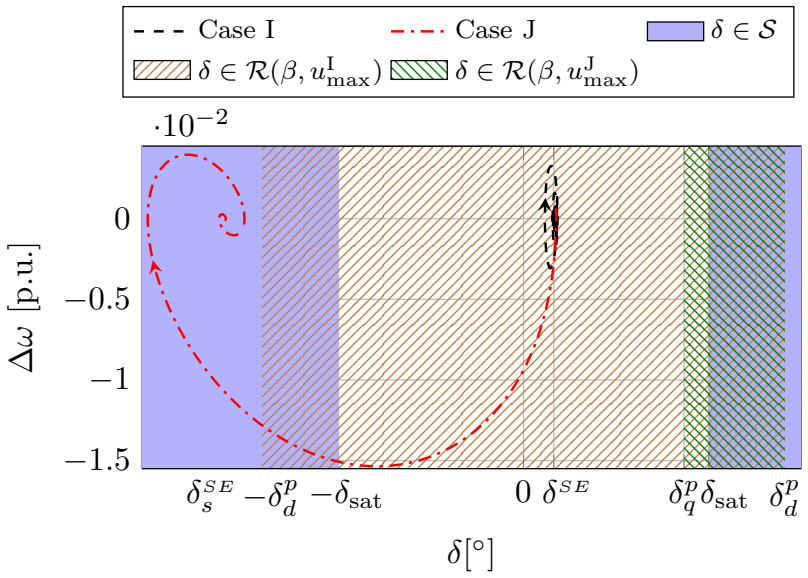


FIGURE 3.33: The post-fault APC trajectories in Cases I and J.

For Case J, the post-fault angle $\delta_{af} = 5.64°$ is out of the set of returning angles as shown in Figure 3.33. Therefore, the GFM IBR stays in the current-saturation mode until it converges to the satSEP demonstrated in Figure 3.32 (i). The GFM IBR injects the reference power to the grid upon reaching the satSEP as demonstrated in Figure 3.32 (ii). However, since it is operating in the current-saturation mode, the voltage controller is disabled. Therefore, the voltage control objectives are not met. Figure 3.32 (iii) shows that the voltage output is more than 1.5 [p.u.], which is not desired at all. Therefore, this case is not a safe case. It is observed that even though the short-circuit fault is brief in Case J, undesired consequences occurred due to the wrong tuning of $u_{\max}$.

3.6.5 Oscillations between normal and current-saturation modes

In all of the cases simulated in the previous subsections, the oscillations have been mitigated with $K_m = 0.95$ according to Subsection 3.3.2.1. In this section, two identical cases, one of which oscillation is mitigated and the other is not, are simulated. The fault occurs at $t = 0.1$ s and is cleared at $t = 0.175$ s. Figure 3.34(a) demonstrates huge oscillations until around $t = 0.8$ s. On the other hand, if the oscillations are mitigated with $K_m = 0.95$, there are brief oscillations around $t = 4$ s as shown in Figure 3.34(b).

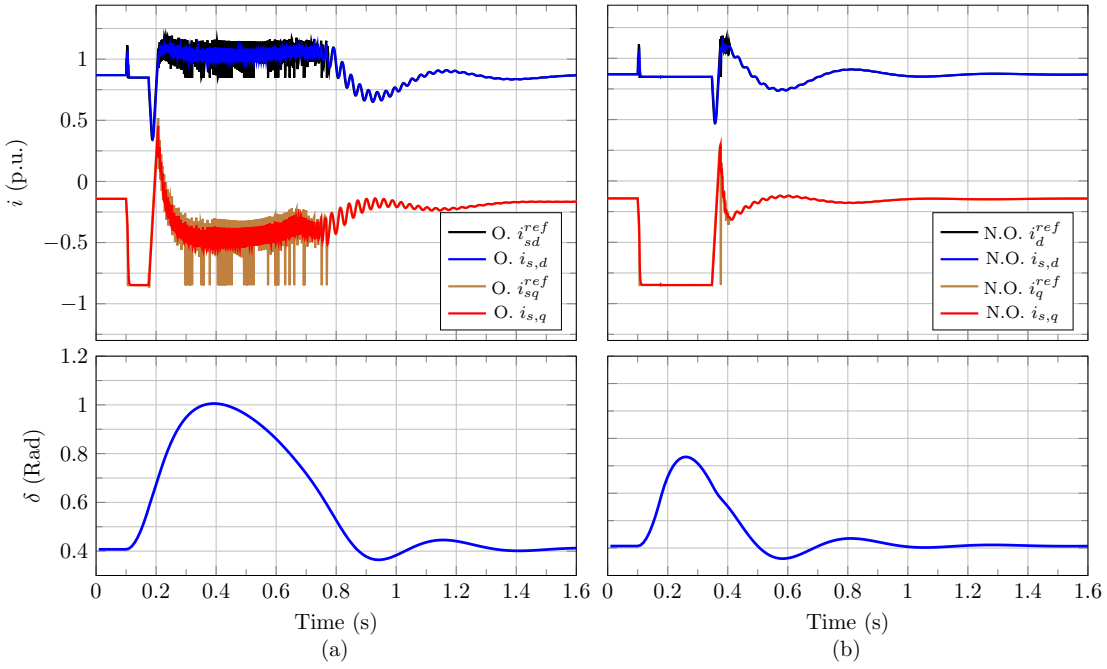


FIGURE 3.34: (a) The original CACRS (without oscillation mitigation) and (b) oscillation mitigated CACRS proposed in Subsection 3.3.2.1.

3.7 Chapter Summary

In this Chapter, the detailed large-signal stability model of GFM IBRs equipped with the constant angle current reference saturation is derived. For this purpose, an exact model of the situations in which the GFM IBR enters or returns from the current-saturation mode is derived. It is proven that if the APC angle belongs to a set called the set of returning angles, the GFM IBR returns to normal operation mode. This set is mainly a function of the angle of the saturated current and the maximum limit of the output of the PI controller of the voltage control loop in addition to the Thevenin impedance of the grid at the point of connection. Therefore, the angle of the saturated current significantly affects the post-fault transient stability behaviour. It is observed that the set of entering angles and the set of returning angles are not complementary, which imposes several challenges, i.e., failing to recover to normal operation mode or oscillating between the normal and current-saturation mode. The set of returning angles not only depends on the angle of the saturation current but also it depends on some details of the voltage controller designs, e.g., the maximum output of the PI controller of the voltage control loop. Therefore, the transient stability analyses cannot be reduced to the study of the dynamics of the active power control loop.

It is discussed that in addition to a stable equilibrium point in normal operation mode, a saturated stable equilibrium point exists. The situations in which a GFM IBR converges to the saturated stable equilibrium point are explored. It is observed that if the angle of the saturated current and the limit of the PI controller of the voltage control loop are not well-tuned, there will be a high risk of converging to the saturated stable equilibrium point. These mathematical derivations are verified through simulations. Simulations show that a faster fault clearance does not necessarily improve the chance of transient stability. It has been observed that if the angle of the saturated current is poorly tuned, there are scenarios in which GFM IBR converges to satSEP for the shorter durations of the fault. Tuning the angle of the saturated current to avoid convergence to the satSEP is proposed in Chapter 4. It is also discussed in this section that the current saturation causes a decrease in post-fault deceleration and, in consequence, a shrinkage in the transient stability domain of attraction. A model predictive control is formulated in Chapter 5 to enhance the transient stability of grid-forming converters.

Chapter 4

Optimal Angle of the Saturated Current for Avoiding Convergence to the Saturated Stable Equilibrium Point

Operating in the current saturation mode imposes several challenges to grid-forming (GFM) inverter-based resources (IBRs), including transient stability and fault recovery ability. It has been discussed in Chapter 3 that a saturated stable equilibrium point (satSEP) is added to the set of singular points due to the current saturation. Converging into the satSEP is an undesired post-disturbance possibility because the grid-forming does not return to its normal operation mode in the steady state. Therefore, the GFM IBR does not act as a voltage source for which it is designed. Hence, it is of high importance to identify and mitigate the situations in which the GFM IBR converges to satSEP.

The post-fault trajectory significantly depends on the angle of the saturated current (β). Depending on the value of this angle, the GFM IBR might converge to SEP or satSEP or become unstable. There might be a set of the angles of the saturated current for which the possibility of convergence into the satSEP is avoided. This chapter aims at unfolding a systematic approach for tuning the β to avoid convergence into the satSEP.

It has been discussed in Chapter 3 that the inclusion of the angle of the satSEP ($\delta_s^{SE}(\beta)$) inside $\mathcal{R}(\beta) - \mathcal{S}$ is a sufficient condition for avoiding the convergence to the satSEP. The set of β for which this condition is satisfied is called the set of avoidance angles in this

thesis and is defined as

$$\mathcal{B} := \left\{ -90^\circ \leq \beta \leq 0^\circ \mid \delta_s^{SE}(\beta) \in \mathcal{R}(\beta) - \mathcal{S} \right\}. \tag{4.1}$$

The convergence to the satSEP is avoided if $\beta \in \mathcal{B}$. If this condition is satisfied, static conditions $\mathcal{C}_{11}$ and $\mathcal{C}_{21}$ for the circumstances $\mathcal{C}_1$ and $\mathcal{C}_2$ are dismissed. There might be some adversary operation points that these two static conditions, i.e., $\mathcal{C}_{11}$ and $\mathcal{C}_{21}$, are inevitable.

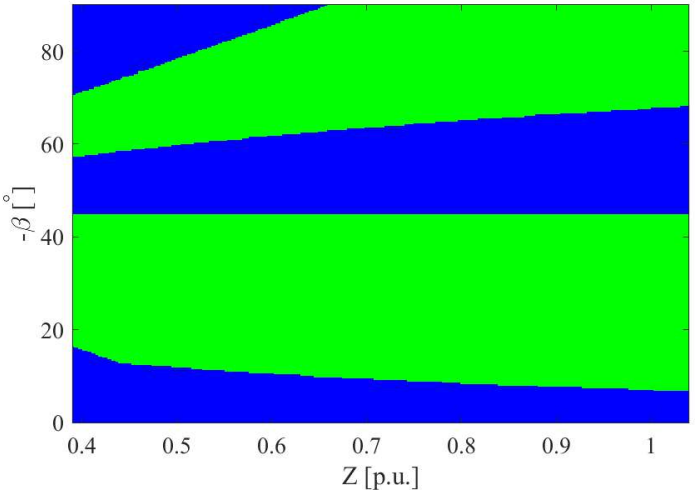


FIGURE 4.1: Numerically calculated set of angles of saturated current for which $\delta_s^{SE}(\beta) \in \mathcal{R}(\beta) - \mathcal{S}$ (green) and $\delta_s^{SE}(\beta) \notin \mathcal{R}(\beta) - \mathcal{S}$ (blue) for different values of the total impedance.

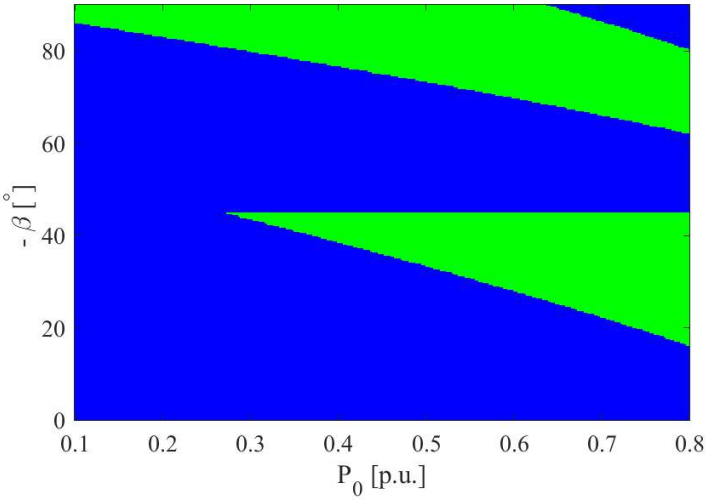


FIGURE 4.2: Numerically calculated set of angles of saturated current for which $\delta_s^{SE}(\beta) \in \mathcal{R}(\beta) - \mathcal{S}$ (green) and $\delta_s^{SE}(\beta) \notin \mathcal{R}(\beta) - \mathcal{S}$ (blue) for different power references.

In these situations, the exact solution for dynamic conditions $\mathcal{C}_{12}$, $\mathcal{C}_{22}$, $\mathcal{C}_{23}$ should be calculated to check convergence to the satSEP. In this thesis, those adverse situations are not investigated. It is assumed that there are a range of β for which $\delta_s^{SE}(\beta) \in \mathcal{R}(\beta) - \mathcal{S}$ has solutions. It is suggested as a future research to investigate transient stability behaviour in those adversary situations.

There might be a range of β for which the avoidance condition is true. This set is a function of the grid strength at the point of connection and the active power reference as depicted in Figures 4.1 and 4.2. In these figures, the area green represents the inclusion of β inside the set of avoidance. Since any selection of β inside the $\mathcal{B}$ prevents convergence to the satSEP, there is an opportunity to tune β for co-optimizing avoidance and other objectives. In this Chapter, the extra objective, which is co-optimized with inclusion in the avoidance set, is to minimize the voltage error upon returning to the normal operation mode. The initial value of the voltage error right after returning to the normal operation mode depends on β. It is discussed in the following section that the higher this voltage error, the larger the magnitude of the oscillations in the active power output (on top of the swing caused by the APC). Therefore, it is of high importance to minimize voltage errors.

4.1 Effect of Voltage Control Loop Error on Output Power

In the steady-state normal operation mode, in which the voltage controller tracks its reference $(V_d^{\text{ref}}, 0)$, the terminal voltage is on the d-axis of the local reference frame. Therefore, the angle between the terminal voltage and the Thevenin voltage of the grid is δ. Consequently, according to (3.1), the active power output follows

$$P^{\text{Unsat}} = \frac{(V_d^{\text{ref}})^2}{Z} \sin\alpha + \frac{V_g V_d^{\text{ref}}}{Z} \sin(\delta - \alpha), \tag{4.2}$$

where $\alpha = \arctan(R/X)$ is a small value for inductive grids.

On the other hand, the terminal voltage does not align with the d-axis before the voltage control loop settles in its steady-state, as shown in Figure 4.3. This misalignment occurs after the voltage controller is re-activated upon returning to the normal operation mode. In this situation, the angle between the terminal voltage and the Thevenin voltage is $\nu + \delta$,

and the active power output is calculated as

$$\tilde{P} = \frac{V^2}{Z}\sin\alpha + \frac{V_g V}{Z}\sin(\delta + \nu - \alpha), \tag{4.3}$$

where ν is the angle between the terminal voltage and the local reference frame. This equation is equivalent to

$$\tilde{P} = \frac{V_d^2 + V_q^2}{Z}\sin\alpha + \frac{V_g V_d}{Z}\sin(\delta - \alpha) + \frac{V_g V_q}{Z}\cos(\delta - \alpha). \tag{4.4}$$

Ignoring the difference between $\frac{V_d^2 + V_q^2}{Z}\sin\alpha$ and $\frac{(V_d^{\text{ref}})^2}{Z}\sin\alpha$, which is a small value for inductive grids, the error of the power output caused by the voltage controller error is

$$\Delta P = P^{\text{Unsat}} - \tilde{P} = \frac{V_g \Delta V_d}{Z}\sin(\delta - \alpha) + \frac{V_g \Delta V_q}{Z}\cos(\delta - \alpha), \tag{4.5}$$

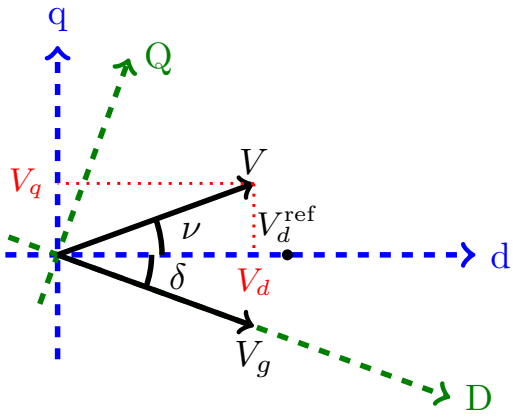


FIGURE 4.3: The GFM IBR's terminal voltage and grid Thevenin voltage phasor diagram in normal operation mode in the presence of the voltage control loop error.

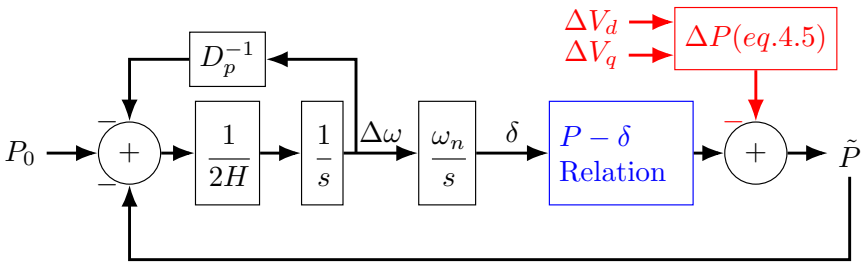


FIGURE 4.4: The equivalent block diagram of the APC loop including voltage-error induced power oscillation as disturbance.

where $\Delta V_d = V_d^{\text{ref}} - V_d$ and $\Delta V_q = 0 - V_q$.

According to (4.5), the power error caused by the voltage controller error is proportional to the voltage error in both d and q directions of the local reference frame. Since the voltage controller undergoes a transient until converging to $(V_d^{\text{ref}}, 0)$ after returning to the normal operation mode, this error is reflected as a power oscillation in the output power on top of the oscillations caused by the swing equation of the APC. This oscillation is an extra disturbance to the APC loop as shown in Figure 4.4, which induces unforeseen transient behaviour on the GFM IBR. To minimize this added oscillation, the voltage error upon returning to the normal operation mode should be minimized. This voltage error is modelled in the next section.

4.2 Voltage Transient After Transiting to the Normal Operation Mode

The voltage controller is deactivated while the GFM IBR is in its current-saturation operation mode. As soon as the GFM IBR returns to the normal operation mode, the voltage controller is re-activated. The terminal voltage goes through a transient until settling to the reference value $(V_d^{\text{ref}}, 0)$. Assuming the bandwidth of the current control loop is significantly high, the control block diagram of the voltage control loop is according to Figure 4.5 [1]. The voltage follows a second-order response. The shape of the voltage transient depends on the filter's capacitance and PI controllers' coefficients. Nevertheless, the magnitude of the transient depends on the initial voltage error, which is

$$\Delta V_d^0(\beta) = V_d^{\text{ref}} - V_g \cos\delta_r(\beta) - ZI_s^{\max} \sin(\alpha - \beta), \tag{4.6}$$

$$\Delta V_q^0(\beta) = V_g \sin\delta_r(\beta) - ZI_s^{\max} \cos(\alpha - \beta), \tag{4.7}$$

where $\delta_r(\beta)$ is the APC angle in which the GFM IBR returns to the normal operation mode. It is the minimum of δ_{sat} and $\delta_u(\beta)$, where $\delta_u(\beta)$ is the upper boundary of $\mathcal{R}(\beta)$.

To minimize the voltage transient, the magnitude of the error, which is $\sqrt{(\Delta V_d^0)^2 + (\Delta V_q^0)^2}$, is minimized. This error is minimum for $\beta = \beta_v$ such that

$$\tan(\alpha - \beta_v) = \frac{1 - \cos\delta_r}{\sin\delta_r}. \tag{4.8}$$

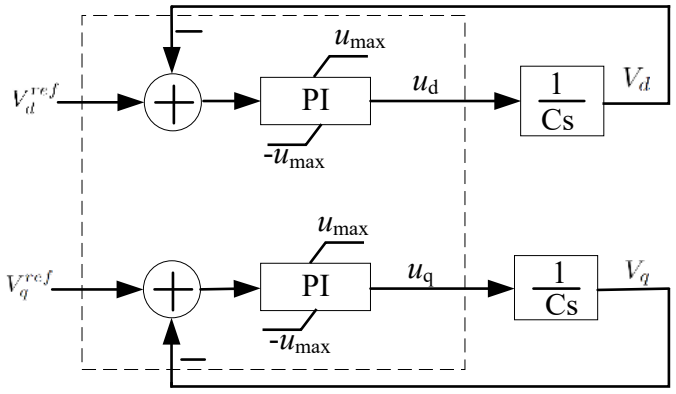


FIGURE 4.5: The equivalent block diagram of the voltage control loop, neglecting the dynamics of the current control loop [1].

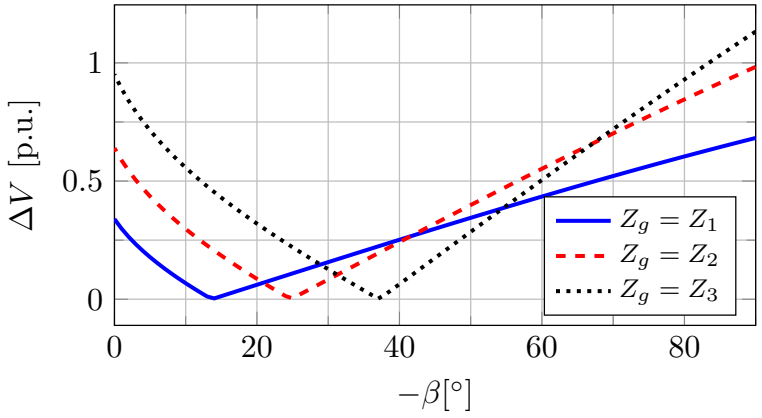


FIGURE 4.6: The variation of the initial transiting voltage error with the angle of the saturated current for different values of grid impedance ($Z_1 < Z_2 < Z_3$).

β_v depends on the impedance of the grid as shown in Figure 4.6. Therefore, an adaptive optimization is required to ensure the proximity of β to β_v (for minimizing voltage error) while $\beta \in \mathcal{B}$ (for avoiding convergence to satSEP) as explained later in this chapter.

4.3 Optimization Formulation

In this section, the proposed adaptive optimization for the angle of the saturated current is presented. This is a multi-objective optimization with the objectives of *a*) *keeping the*

angle of the satSEP in $\mathcal{R}(\beta) - \mathcal{S} = \mathcal{R}(\beta) \cap \overline{\mathcal{S}}$ while *b) minimizing the deviation of* β *from* β_v*, introduced in the Section 4.2.* Since this inclusion might be infeasible for any value of β in some scenarios, this constraint is modelled as a soft constraint from which the deviation is minimized. Therefore, the objective function is defined as

$$\min_{\mathcal{D}} \; K(\epsilon + \eta_1 + \eta_2) + (\beta - \beta_v)^2, \tag{4.9}$$

where the positive variable ϵ is the deviation of the angle of the satSEP from $\overline{\mathcal{S}}$, and the positive variables η_1 and η_2 are its deviation from $\mathcal{R}(\beta)$ when $\beta \in [-45°, 0°]$ and $\beta \in [-90°, -45°]$; respectively. The coefficient K is chosen as a big value to penalize deviation from $\mathcal{R} \cap \overline{\mathcal{S}}$. The set of decision variables $\mathcal{D}$ comprises β, β_v, ϵ, η_1, η_2 and all modelling variables, which are introduced in the following paragraphs. This optimization is subject to the modelling constraints, which are explained in detail in the following paragraphs.

β should be bounded within an upper limit and lower limit to prevent under-voltage and over-voltage during post-fault current saturation mode, i.e.,

$$\beta_{\min} \leq \beta \leq \beta_{\max}. \tag{4.10}$$

The angle of the satSEP should be in $\overline{\mathcal{S}}$, which is $[-\delta_{\text{sat}}, \delta_{\text{sat}}]$. This is formulated as

$$-(\epsilon + \delta_{\text{sat}} - \rho_1) \leq -\beta - \arccos \frac{P_0}{V_g.I_s^{\max}} \leq \epsilon + \delta_{\text{sat}} - \rho_1, \tag{4.11}$$

where ρ_1 is the margin from the boundary of $\overline{\mathcal{S}}$, and ϵ is the deviation from this soft constraint. This deviation is minimized as an objective of the optimization.

The boundaries of set $\mathcal{R}(\beta)$ depend on whether β is more or less than $-45°$ as explained in Chapter 3. To model this discontinuity in constraints, the binary variables a_1 and a_2 are introduced. a_1 is zero if β is more than $-45°$, and a_2 is zero if β is less than $-45°$. Accordingly, these two are formulated as

$$a_1 + a_2 \leq 1, \tag{4.12}$$

$$-M_1 a_2 \leq -\beta - 45°, \tag{4.13}$$

$$-\beta - 45^\circ \leq M_1 a_1, \tag{4.14}$$

where M_1 is a big parameter. The angle of the satSEP should be inside $\mathcal{R}(\beta)$ with the minimum deviations of η_1 and η_2 from its upper and lower boundaries, respectively. This is formulated as

$$-(\eta_1 + \delta_d^p + M_2 a_1 - \rho_2) \leq -\beta - \arccos \frac{P_0}{V_g.I_s^{\max}} \leq \eta_1 + \delta_d^p + M_2 a_1 - \rho_2, \tag{4.15}$$

$$-(\eta_2 + \delta_q^p + M_2 a_2 - \rho_2) \leq -\beta - \arccos \frac{P_0}{V_g.I_s^{\max}} \leq \eta_2 + 180^\circ - \delta_q^p + M_2 a_2 - \rho_2, \tag{4.16}$$

where M_2 is a big parameter, and ρ_2 is the margin from boundary. According to Chapter 3, δ_d^p and δ_q^p are formulated as

$$\delta_d^p = \arccos\left(\frac{V_d^{\text{ref}} - ZI_s^{\max}\sin(\alpha-\beta)}{V_g}\right), \tag{4.17}$$

$$\delta_q^p = \arcsin\left(\frac{ZI_s^{\max}\cos(\alpha-\beta)}{V_g}\right). \tag{4.18}$$

The second objective of this multi-objective optimization is to minimize the deviation of β from β_v. Therefore, β_v should be modelled in constraints. According to Section 4.2, β_v is assessed as

$$\tan(\alpha - \beta_v) = \frac{1-\cos\delta_r}{\sin\delta_r}. \tag{4.19}$$

δ_r, which is the angle of returning to the normal operation mode, is the lowest value among δ_{sat} and δ_u, defined in Section 4.2. Two auxiliary binary variables a_3 and a_4 are used to compare δ_u and δ_{sat} as

$$a_3 + a_4 \leq 1, \tag{4.20}$$

$$-M_2 a_4 \leq \delta_u - \delta_{\text{sat}} \leq M_2 a_3. \tag{4.21}$$

If δ_u is lower, a_3 becomes zero. Otherwise, a_4 becomes zero. Thus, δ_r is modelled as

$$-M_2 a_3 \leq \delta_r - \delta_u \leq M_2 a_3, \tag{4.22}$$

$$-M_2 a_4 \leq \delta_r - \delta_{\text{sat}} \leq M_2 a_4. \tag{4.23}$$

δ_u depends on whether β is more than -45° or less than -45°. Therefore, δ_u is modelled as

$$-M_2 a_1 \leq \delta_u - \delta_d^p \leq M_2 a_1, \tag{4.24}$$

$$-M_2 a_2 \leq \delta_u - (180^\circ - \delta_q^p) \leq M_2 a_2. \tag{4.25}$$

Since the functions in (4.19) are triangular, there are multiple solutions for β_v. However, only the solution which is between -90° and 0° is acceptable, i.e.,

$$-90^\circ \leq \beta_v \leq 0^\circ. \tag{4.26}$$

After running the optimization code with Artelys Knitro numerical solver [91], it is observed that the optimization struggles to find the solution if an additional constraint that bounds the lower value of δ_r to a small non-zero value is not added to the set of constraints, i.e.,

$$\zeta \leq \delta_r, \tag{4.27}$$

where ζ is a very small positive value. Since δ_r, which is the APC angle GFM IBR returns to normal operation mode, is positive, this constraint does not affect the final optimization solution. This constraint is added to prevent division by zero in (4.19) while the solver is looking for a numerical solution.

The aforementioned optimization is a mixed integer nonlinear program with nine continuous variables, four binary variables, twenty-eight inequality constraints, and three equality constraints.

Param.	*Values*	*Units*	*Descriptions*
S_b	310	MVA	Nominal apparent power
P_0	270	MW	Active power reference
V_b	400	V	Nominal Voltage
V_{dc}	1200	V	DC link voltage
n	816	-	Number of parallel GFM IBRs
f_n	60	Hz	Nominal frequency
D_p	0.03	p.u.	Active droop coefficient
H	2	p.u.	Virtual inertia
$\Delta\omega_{\max}$	0.0066	p.u.	Maximum frequency deviation
V_d^{ref}	1	p.u.	Voltage reference magnitude
$I_s^{\max}$	1.2	p.u.	Maximum allowed current
X_{tr}	0.16	p.u.	Total reactance of transformer windings

TABLE 4.1: Parameters of the simulated GFM farm.

4.4 Results and discussions

To examine the capability of the proposed method for preventing the GFM IBR from converging to the satSEP and soft transition to the normal operation mode, the system of Figure 2.7 with parameters of Table. 4.1 is simulated in MATLAB/Simulink [90]. Artelys Knitro solver, which is capable of solving mixed-integer nonlinear optimization problems, [91] is used to solve the optimization proposed in this chapter. Theoretical analysis and proofs in the previous subsections guarantee achieving the objectives. Therefore, unlike data-driven methods for which a vast range of scenarios should be simulated, simulating

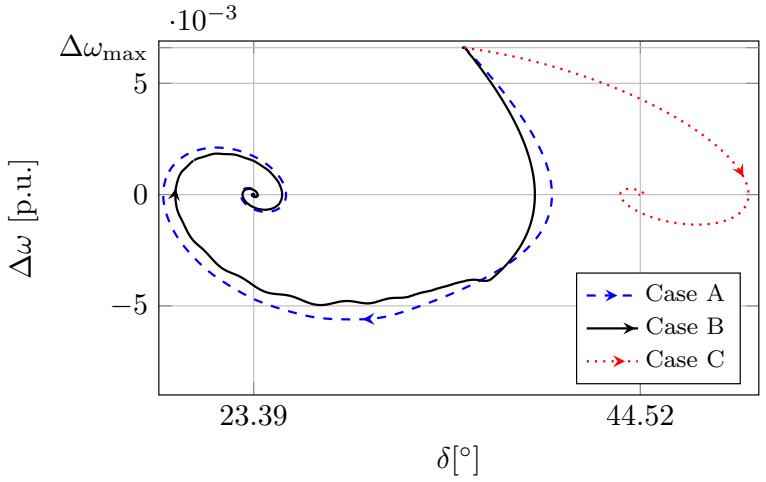


FIGURE 4.7: Post-fault trajectories in cases A, B, and C.

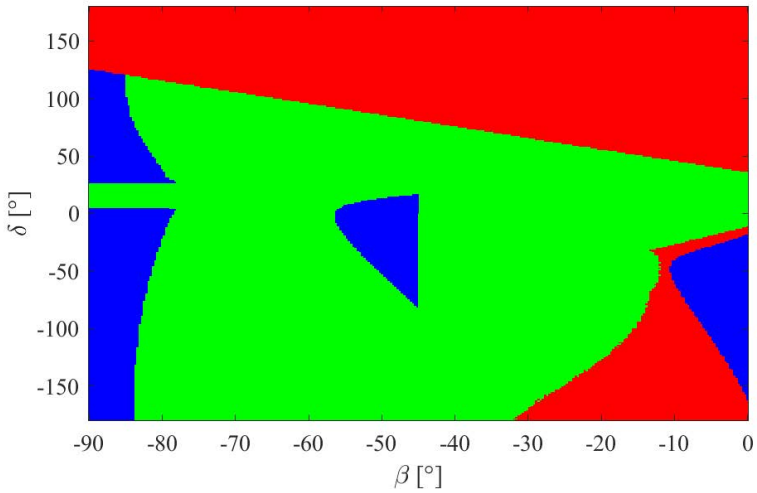


FIGURE 4.8: The APC angle for which the GFM IBR converges to SEP (green), converges to satSEP (blue), or becomes unstable (red) for different values of β in scenario 1.

multiple scenarios is not required. Two scenarios are simulated to compare the post-fault dynamics of the GFM IBR with optimal β and non-optimal β:

- Scenario 1: The GFM IBR is connected to a grid with the Thevenin impedance of 0.3 p.u. and X/R ratio of 20. In this situation, $\beta_v = -13.66°$. In this scenario, $\delta_s^{SE}(\beta_v) \in \mathcal{R}(\beta_v) - \mathcal{S}$. Therefore, the optimal angle of the proposed optimization is $\beta^* = \beta_v$, which is the numerically solved solution of the proposed optimization.

- Scenario 2: The GFM IBR is connected to a grid with the Thevenin impedance of 0.6 p.u. and X/R ratio of 20. In this scenario, $\beta_v = -24.57°$. In this scenario also, $\delta_s^{SE}(\beta_v) \in \mathcal{R}(\beta_v) - \mathcal{S}$. Hence, similarly, the optimal angle of the proposed optimization is $\beta^* = \beta_v$.

Three cases of A, B, and C, for which the angles of the saturated current are $\beta_A = \beta^*$ $(-13.66°)$, $\beta_B = -30°$, and $\beta_C = -90°$, are simulated for scenario 1. A three-phase short circuit fault with a duration of 0.1 s causes an increase in APC angle to 34.9° in these cases. This three-phase fault is modelled as a voltage drop of 0.95 p.u. The GFM IBR converges to SEP in cases A and B, and it converges to satSEP in case C as shown in Figure 4.7. In case C, the angle of satSEP, i.e. $\delta_s^{SE}(\beta_C) = 44.52°$, is in $\mathcal{S}$, and initial post-fault APC angle $\delta_{af} = 34.96°$ is inside its DOA. Therefore, it converges into satSEP through $\mathcal{C}_1$ explained in Chapter 3.

Figure 4.8 shows numerically calculated post-fault APC angles for which the GFM IBR converges to SEP (green), converges to satSEP (blue), or becomes unstable (red) under

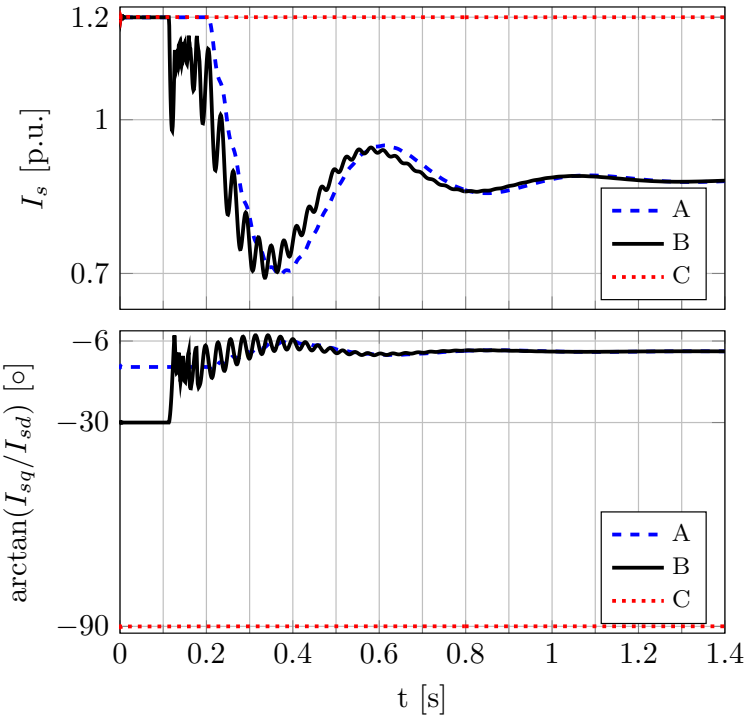


FIGURE 4.9: Post-fault currents in cases A, B, and C.

scenario 1. The trajectories are calculated based on *a*) the power-angle relation in normal operation and current-saturation operation modes and *b*) swing equation. The internal control loops are not considered in the numeric trajectory calculation of Figure 4.8. It can be observed that choosing $\beta_C = -90°$ causes converging to satSEP for a considerably big range of δ_{af}. However, the GFM IBR does not converge to the satSEP for $\beta_A = -13.66°$ and $\beta_B = -30°$. In case A, which is the optimal case, $\delta_s^{SE}(\beta^*) = -29.80° \in \mathcal{R}(\beta^*) - \mathcal{S} = [-32.0455°, 32.0455°]$. Hence, sufficient conditions are met to avoid converging into satSEP.

In order to expand the investigation beyond the numerically calculated trajectories, EMT simulations are conducted for these three scenarios in Simulink/MATLAB environment. Figure 4.9 shows that the GFM IBR returns to the normal operation mode around 0.2 s after clearing the fault. Since the angle of saturated current is β_v in case A, the post-fault voltage transient is small, as shown in Figure 4.10. In comparison, case B has a larger voltage transient. This voltage transient is reflected in a higher frequency oscillation in power transient as modelled in Section 4.1 and depicted in Figure 4.11.

To examine the method for a weak grid, three cases of D, E, and F for which the angles of the saturated current are $\beta_D = \beta^*$ $(-24.57°)$, $\beta_E = 0°$, and $\beta_F = -30°$ are simulated

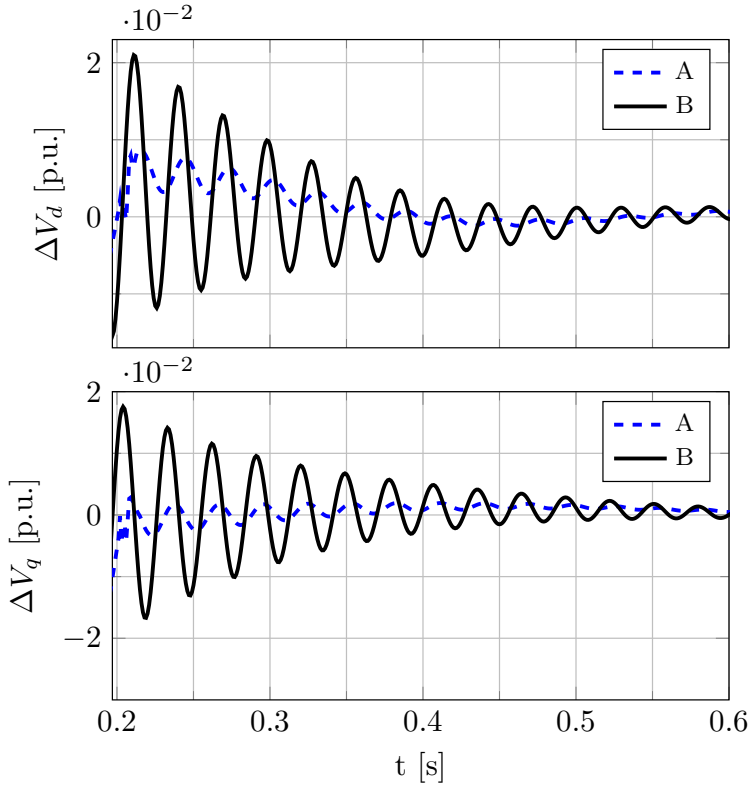


FIGURE 4.10: Terminal voltage of the GFM IBR after returning to the normal operation mode in cases A and B.

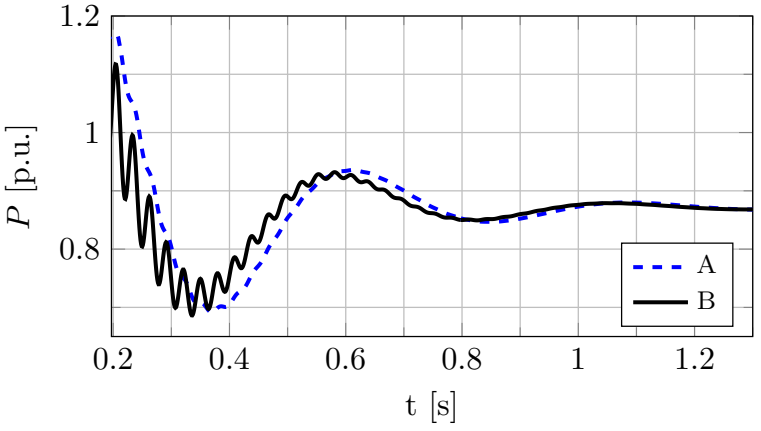


FIGURE 4.11: Active power output of the GFM IBR after returning to the normal operation mode in cases A and B.

under scenario 2. A three-phase short circuit fault with a duration of 0.1 s causes δ to increase to 52.1° for cases D, E, and F. Similar aspects that have been investigated for cases A, B, and C are being analyzed for cases D, E, and F. According to Figure 4.12,

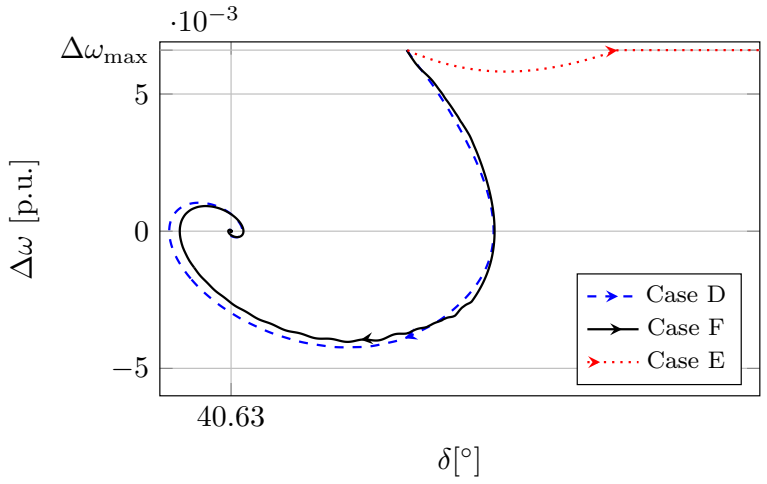


FIGURE 4.12: Post-fault trajectories in cases D, E, and F.

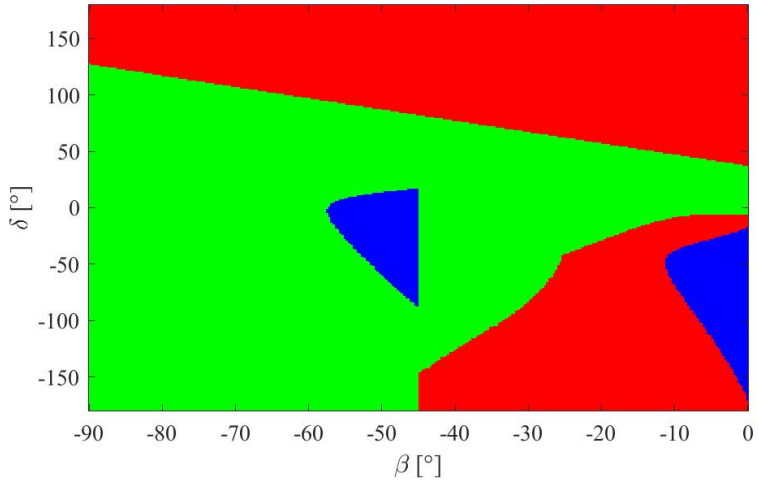


FIGURE 4.13: The APC angle for which the GFM IBR converges to SEP (green), converges to satSEP (blue), or becomes unstable (red) for different values of β in scenario 2.

the GFM IBR becomes unstable in case E because of insufficient deceleration when it is in current-saturation mode with $\beta_E = 0°$. The other two cases are stable and converge to the SEP.

Figure 4.13 shows numerically calculated post-fault APC angles for which the GFM IBR converges to the GFM IBR converges to the SEP (green), converges to the satSEP (blue), or becomes unstable (red) under scenario 2. The GFM IBR is either unstable or converges to satSEP for a big range of δ if $\beta = 0°$. For $\beta = \beta^* = -24.57°$ (case D) and $\beta = -30°$ (case F), the GFM IBR never converges to satSEP. The satSEP angle in the case of $\beta = \beta^*$

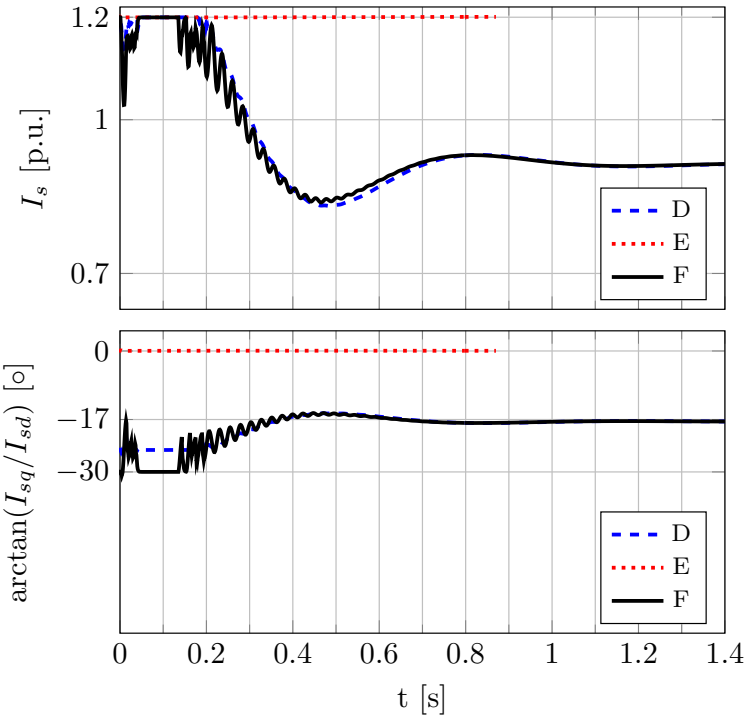


FIGURE 4.14: Post-fault currents in cases D, E, and F.

is $\delta_s^{SE}(\beta^*) = -18.90°$, which is in $\mathcal{R}(\beta^*) - \mathcal{S} = [-54.26°, 54.26°]$. Therefore, the sufficient condition for avoiding converging into satSEP is met.

According to Figure 4.14, the GFM returns to the normal operation mode around 0.2 s after clearing the fault for cases D and F. For case D, in which $\beta = \beta^* = \beta_v$, there is a small voltage transient after coming back to the normal operation mode. This is bigger for case F according to Figure 4.15.

4.5 Chapter Summary

In this chapter, a multi-objective optimization is proposed to find the optimal angle of the saturated current β for two purposes:

- Objective 1: Avoiding the convergence into the saturated stable equilibrium point.
- Objective 2: Minimizing the voltage transient after returning to the normal operation mode. This voltage transient is reflected in the output power as an extra oscillation on top of the APC power swing.

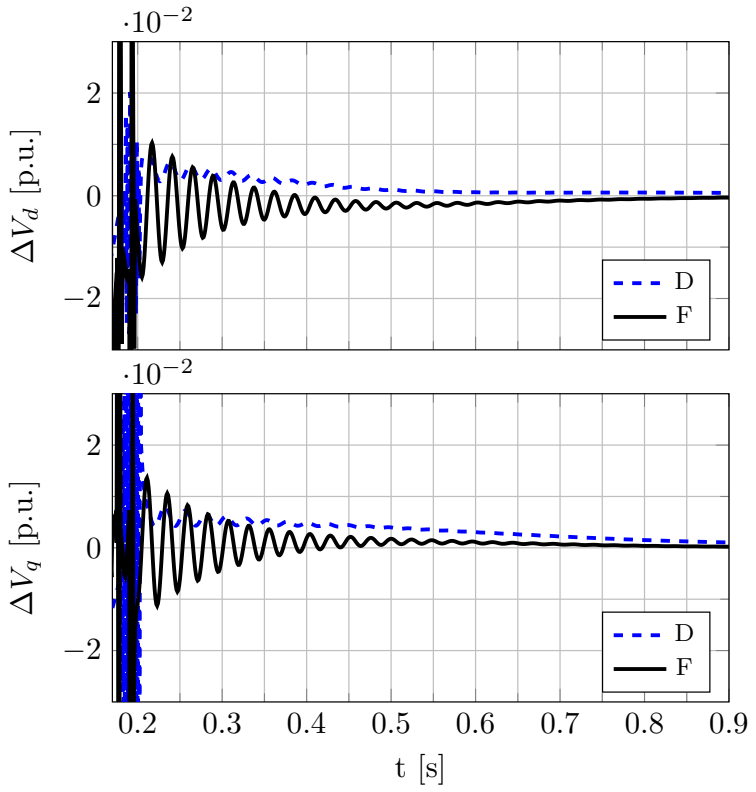


FIGURE 4.15: Terminal voltage of the GFM IBR after returning to the normal operation mode in cases D and F.

The sufficient condition for satisfying the first objective is that $\delta_s^{SE} \in \mathcal{R}(\beta) - \mathcal{S}$. There might be a range of angles for which this constraint is satisfied. Among this range, the angle which is closer to β_v is the optimal solution for objective 2. β_v is the angle of the saturated current for which the voltage error upon returning to the normal operation mode is minimized.

Even though the β tuned through this method ensures avoidance from converging into the satSEP, it does not guarantee stability (converging into the SEP). To increase the chance of stability, a model predictive control is proposed in Chapter 5.

Chapter 5

A Model Predictive Control for Enhancing Transient Stability of Grid-Forming Converter

Chapter 3 discussed that two main challenges are imposed by the current limitation on the transient stability of grid-forming (GFM) inverter-based resources (IBRs): (1) the possibility of convergence to the saturated stable equilibrium point, (2) shrinking the domain of attraction of the stable equilibrium point (SEP). Chapter 4 addressed the former challenge by proposing the selection of the angle of the saturated current (β) to avoid convergence to the saturated stable equilibrium point. This chapter aims to unfold the potential benefits of the flexibility of redesigning the software-defined dynamics of GFM IBRs to enhance their transient stability. To do so, two corrective signals, which are optimized through a model predictive control (MPC), are added to the active power controller (APC). This method is compared against two benchmarks of transient stability enhancement, which are briefly reviewed in the next subsection. Later in this chapter, the proposed MPC is structured and formulated. It is followed by a conservative estimation of the stability domain of attraction (DOA) of a GFM IBR equipped with the proposed control structure. After that, several case studies and sensitivity analyses are performed to test the ability of the proposed MPC to enhance the transient stability of grid-forming converters. Finally, this chapter is wrapped up with a summary.

5.1 Benchmark Methods in Transient Stability Enhancement

One of the effective ways to enhance the transient stability of GFM IBR is to limit the fault-on acceleration by bounding the frequency of the APC [4]. This method is called bounding the frequency (Strategy B) in the rest of this thesis. Not only does it cause less required post-fault deceleration to decrease the frequency to the nominal frequency, but it also limits the rate of the APC angle increment during the fault-on situation.

In order to support the claim that bounding the frequency during the fault reduces the required post-fault deceleration area, the equal area criterion is investigated for a GFM IBR equipped with this strategy. Consider the APC angle is δ_0 before the fault. It increases to δ_1 during the fault, and reaches the maximum APC angle δ_2 after the fault. The APC angular frequency reaches its maximum limit when the APC angle is δ'. Checking the equal area criteria [12],

$$\int_{\delta_0}^{\delta'} \frac{H}{\omega_n} \left(\frac{d\delta}{dt}\right)^2 d\delta = \int_{\delta_0}^{\delta'} (P_0 - P)\, d\delta, \tag{5.1}$$

$$\int_{\delta'}^{\delta_1} \frac{H}{\omega_n} \left(\frac{d\delta}{dt}\right)^2 d\delta = \frac{H}{\omega_n}(\delta_1 - \delta')\omega_{\max}^2, \tag{5.2}$$

$$\int_{\delta_1}^{\delta_2} \frac{H}{\omega_n} \left(\frac{d\delta}{dt}\right)^2 d\delta = \int_{\delta_1}^{\delta_2} (P_0 - P)\, d\delta. \tag{5.3}$$

Since $\frac{d\delta}{dt} = 0$ for both δ_0 and δ_2,

$$\int_{\delta_0}^{\delta'} \frac{H}{\omega_n} \left(\frac{d\delta}{dt}\right)^2 d\delta + \int_{\delta'}^{\delta_1} \frac{H}{\omega_n} \left(\frac{d\delta}{dt}\right)^2 d\delta + \int_{\delta_1}^{\delta_2} \frac{H}{\omega_n} \left(\frac{d\delta}{dt}\right)^2 d\delta = \int_{\delta_0}^{\delta_2} \frac{H}{\omega_n} \left(\frac{d\delta}{dt}\right)^2 d\delta = 0. \tag{5.4}$$

Thus, the summation of the right-hand sides of (5.1), (5.2), and (5.3) is also zero.

$$\int_{\delta_0}^{\delta'} (P_0 - P)\, d\delta + \frac{H}{\omega_n}(\delta_1 - \delta')\omega_{\max}^2 + \int_{\delta_1}^{\delta_2} (P_0 - P)\, d\delta = 0. \tag{5.5}$$

Therefore, the required deceleration is

$$DS_b = \int_{\delta_1}^{\delta_2} (P - P_0)\, d\delta = \int_{\delta_0}^{\delta'} (P_0 - P)\, d\delta + \frac{H}{\omega_n}(\delta_1 - \delta')\omega_{\max}^2. \tag{5.6}$$

In order to prove that the required deceleration area is smaller when the GFM IBR is equipped with the bounding frequency, the right-hand side of (5.6) should be compared with a GFM IBR not equipped with bounding the frequency. In the absence of bounding the frequency, the required deceleration is

$$DS_{nb} = \int_{\delta_0}^{\delta'} (P_0 - P)\, d\delta + \int_{\delta'}^{\delta_a} (P_0 - P)\, d\delta, \tag{5.7}$$

where δ_a is the clearing APC angle. For the same duration of fault, $\delta_1 \leq \delta_a$ because the GFM IBR has a higher APC angular frequency in absence of bounding the frequency. Thus, a lower limit for the required deceleration can be found according to

$$\int_{\delta_0}^{\delta'} (P_0 - P)\, d\delta + \int_{\delta'}^{\delta_1} (P_0 - P)\, d\delta \leq DS_{nb}, \tag{5.8}$$

Thus, if it is proven that

$$\frac{H}{\omega_n}(\delta_1 - \delta')\omega_{\max}^2 \leq \int_{\delta'}^{\delta_1} (P_0 - P) d\delta, \tag{5.9}$$

it will be also proven that $DS_b \leq DS_{nb}$. Since during the fault $P \leq P_0$, according to the swing equation ω increases during the fault. Thus, $\omega_{\max} \leq \frac{d\delta}{dt}$. Therefore,

$$\int_{\delta'}^{\delta 1} (P_0 - P)\, d\delta = \int_{\delta'}^{\delta_1} \frac{H}{\omega_n} \left(\frac{d\delta}{dt}\right)^2 d\delta \geq \int_{\delta'}^{\delta_1} \frac{H}{\omega_n}\omega_{\max}^2 d\delta. \tag{5.10}$$

Hence,

$$\frac{H}{\omega_n}(\delta_1 - \delta')\omega_{\max}^2 \leq \int_{\delta'}^{\delta_1} (P_0 - P) d\delta, \tag{5.11}$$

Therefore, the required post-fault deceleration is less if the GFM IBR is equipped with bounding the frequency.

Figure 5.1 visualizes two post-fault trajectories in cases of bounding and not bounding the frequency. This figure demonstrates that if the frequency is bounded to a sufficiently small value, the deviations of the APC angle and frequency from the stable equilibrium point are insignificant. However, if the fault is too long, even bounding the frequency might

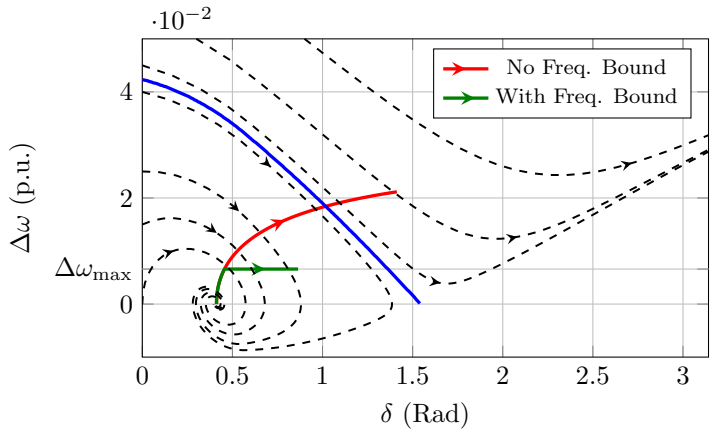


FIGURE 5.1: Fault-on trajectories of a GFM IBR (a) equipped and (b) not equipped with frequency bounding if $X = 0.46$ p.u. The blue line is the border of the DOA.

not be sufficient for stabilizing the system. Therefore, a corrective control for providing additional deceleration is required.

Another effective way to enhance the transient stability of GFM IBRs is to compensate for the difference between the unsaturated active power and saturated active power as an extra input to the APC. This strategy is denoted as Strategy C in the rest of this thesis. Reference [31] used the unsaturated reference current for calculating the unsaturated virtual power. Although the work in [31] is based on the circular current limiter in cascade with a virtual admittance voltage controller, it can be adapted to other implementations of the grid-forming control. This method provides additional deceleration in the post-fault current-saturation operation mode and decreases the fault-on acceleration in the current-saturation operation mode. However, the additional deceleration might be more or less than the required amount. Therefore, an optimal control strategy is required for this purpose. In the next section, an MPC strategy, which is proposed for controlling the post-fault trajectory, is introduced.

5.2 Structure and Formulation of the Proposed Model Predictive Control

The previous section discussed how bounding the frequency reduces the acceleration. Nevertheless, an additional post-fault control is required to ensure the transient stability of the GFM IBR in case of a long fault duration. Since the dynamics of GFM IBRs follow a software-defined behaviour, the control structure of the GFM IBR can be redesigned

for enhancing the transient stability. Nevertheless, restructuring the control architecture might adversely impact other stability phenomena. Therefore, this thesis proposes to provide the extra modifications only if an adverse situation is detected. More specifically, this adverse situation is the operation in post-fault current-saturation mode. In this case, two extra corrective signals, i.e., corrective power reference change and corrective phase jump, are added to the APC control structure according to Figure 5.2. These two corrective control signals provide direct controllability over the frequency and angle of APC, respectively. The trajectory modification rooted in these corrective signals follows

$$\Delta\omega_{\text{corr}}(k) = \frac{T_d}{2H}(\Delta P_{\text{ref}}(k)), \tag{5.12}$$

$$\Delta\delta_{\text{corr}}(k) = \Delta\delta_c(k) - \Delta\delta_c(k-1), \tag{5.13}$$

where T_d is the time step length, and $\Delta P_{\text{ref}}(k)$ and $\Delta\delta_c(k)$ are corrective power reference change and corrective phase jump at k_{th} time step.

To maximize the captured benefits from the corrective signals ΔP_{ref} and $\Delta\delta_c(k)$ while keeping the post-fault trajectory in a safe region, the value of these two corrective signals

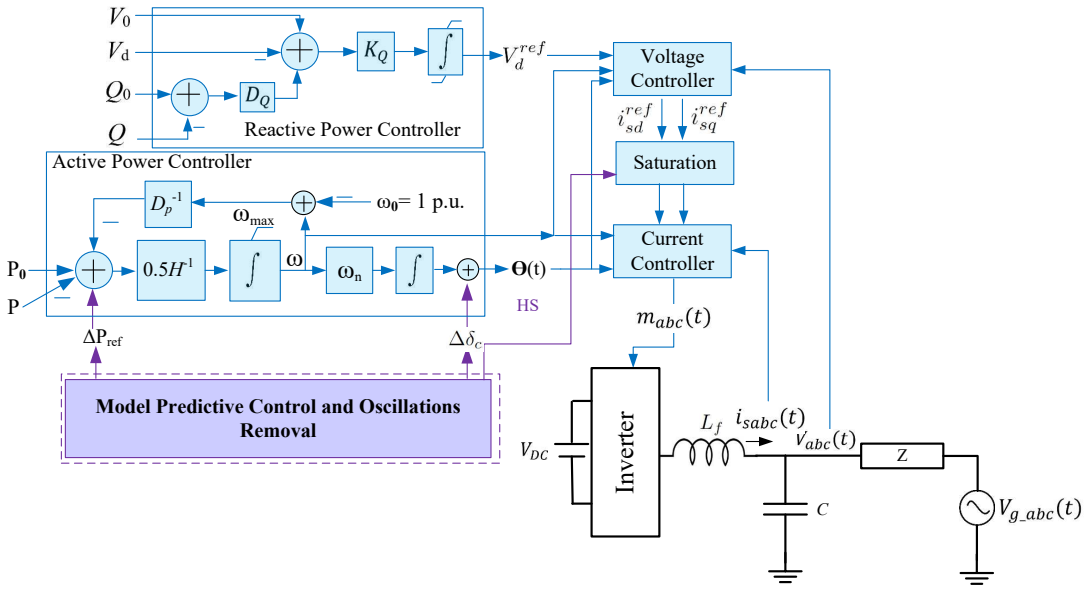


FIGURE 5.2: The general structure of VSG GFM IBRs [2, 3, 4] added with an MPC module to enhance the transient stability.

are optimized through an MPC. This MPC aims to minimize the deviation from the angle of SEP, subject to two sets of constraints:

- $\mathcal{G}_1$: The set of constraints that model the post-fault transient dynamics behaviour of a GFM IBR.
- $\mathcal{G}_2$: The set of constraints that put safety limitations on the post-fault trajectory of a GFM IBR.

The optimization formulation of the proposed MPC is explained in detail in the following subsection.

5.2.1 Optimization Formulation

This subsection formulates the proposed MPC method to enhance the post-disturbance stability of GFM IBRs. Throughout this subsection, the notion $k \in \{0, 1, \ldots, T/T_d - 1\}$ represents the time index. The length of the optimization horizon is T, and the time step size is T_d. In each time step, the optimization solver calculates the optimization solution if the adverse situation is still detected. The system is discretized using the Euler method [92]. The objective function of this optimization is to minimize the APC angle deviations from the SEP, which is formulated as

$$\min_{\mathcal{D}} \sum_{k=0}^{T/T_d-1} \left(\delta(k) - \arcsin\left(\frac{P_0 X}{V_g V_d^{\text{ref}}} \right) \right)^2 \tag{5.14}$$

subjected to the set of constraints $\mathcal{G} = \mathcal{G}_1 \cup \mathcal{G}_2$, where $\mathcal{G}_1$ models the post-fault dynamics of GFM IBRs, and $\mathcal{G}_2$ imposes safety limitations on the post-fault trajectory of the GFM IBR. These constraints are listed in the following paragraphs. The set of the decision variables $\mathcal{D}$ includes $\Delta P_{\text{ref}}(k)$ and $\Delta\delta_c(k)$ in addition to the variables that model the dynamics of the GFM IBR indexed by all time steps ($k \in \{0, 1, \ldots, T/T_d - 1\}$).

To begin with the list of $\mathcal{G}_1$ constraints, the most important variable whose dynamics should be modelled is the APC angle. This variable plays a prominent role in maintaining the transient [angle] stability. Considering the effect of the corrective power jump as in (5.13) into the discretized swing equation for angle [12], the APC angle is modelled as

$$\delta(k+1) - \delta(k) = \Delta\delta_c(k+1) - \Delta\delta_c(k) + T_d\omega_n(\omega(k) - \omega_0). \tag{5.15}$$

The constraints subset $\mathcal{G}_1$ also includes the discretized swing equation for the frequency. Since the corrective power reference change affects the APC frequency, equation (5.12) should be integrated into the swing equation for the frequency as

$$\omega(k+1) - \omega(k) = \frac{T_d}{2H}\left(P_0 + \Delta P_{\text{ref}}(k) - P(k) - \frac{1}{D_p}(\omega(k) - \omega_0)\right). \tag{5.16}$$

The active power output of the GFM IBR is a function of the APC angle and its operation mode. It is discussed in Chapter 3 that the active power-angle characteristics in normal operation and current-saturation operation modes are different. In order to model the operation mode of the GFM IBR, a binary variable $n(k)$ is introduced to the set of decision variables ($\mathcal{D}$). This variable is 0 if the GFM IBR is in the current-saturation mode, and it is 1 if it is in the normal operation mode. It is mentioned in Chapter 3 that the GFM IBR is in the current saturation mode if the APC angle is more than δ_{sat}, which is calculated according to (3.7)[1]. To provide a connection between this fact and the modelling of $n(k)$, the following equations are added to $\mathcal{G}_1$.

$$\delta_{\text{sat}} - \delta(k) \leq Mn(k) \tag{5.17}$$

$$-M(1 - n(k)) \leq \delta_{\text{sat}} - \delta(k), \tag{5.18}$$

where M is a sufficiently large parameter. In these equations, $n(k) = 1$ only if $\delta(k) \leq \delta_{\text{sat}}$. This binary variable enables including the comparison into the modelling, and in consequence, the active power output is modelled as

$$-Mn(k) \leq P(k) - \frac{V_g I_{sat} \cos\big(\delta(k) + \beta\big)}{1 - XC\omega\omega_n} \leq Mn(k) \tag{5.19}$$

$$-M(1 - n(k)) \leq P(k) - \frac{V_g V_d^{\text{ref}}}{X} \sin\big(\delta(k)\big) \leq M\big(1 - n(k)\big) \tag{5.20}$$

The constraints subset $\mathcal{G}_1$ comprises (5.15)-(5.20). The remainder of the expressions in this subsection form the subset $\mathcal{G}_2$, which bounds the variables inside their safe range. This set initially ensures that the corrective phase jumps do not cause excessive APC angle change,

[1] In this Chapter, it is assumed that $\mathcal{R} - \mathcal{S} = \overline{\mathcal{S}}$ and mode oscillations are mitigated.

i.e.,

$$\Delta\delta_{\min} \leq \delta(k+1) - \delta(k) \leq \Delta\delta_{\max} \,. \tag{5.21}$$

Furthermore, the proposed MPC should ensure that the frequency deviations are within an acceptable range through the following constraint.

$$\omega_{\min} \leq \omega \leq \omega_{\max}. \tag{5.22}$$

The GFM IBR should not absorb power from the grid. It can be formulated as bounding the APC range between zero and $\delta_{\text{zc}}^{\text{sat}}$. $\delta_{\text{zc}}^{\text{sat}}$ is the APC angle for which the saturated active power is zero. The saturated active power becomes negative upon passing this angle. Therefore, the following inequality is added to the constraints set.

$$0 \leq \delta(k) \leq \delta_{\text{zc}}^{\text{sat}}. \tag{5.23}$$

Upon returning to the normal operation mode, the corrective active power reference change signal is not fed to the APC. This essence is formulated as

$$-\Delta P_{\text{ref}}^{\max}\big(1 - n(k)\big) \leq \Delta P_{\text{ref}}(k) \leq \Delta P_{\text{ref}}^{\max}\big(1 - n(k)\big). \tag{5.24}$$

Besides, there should not be any further corrective phase jumps in the normal operation mode. Thus, $\Delta\delta_c$ should not change while the GFM IBR is in the normal operation mode, so

$$-\Delta\delta_c^{\text{chg,max}}\big(1 - n(k)\big) \leq \Delta\delta_c(k+1) - \Delta\delta_c(k) \leq 0. \tag{5.25}$$

Before mentioning the next constraint, it should be mentioned that the essence of the following constraint was realized after noticing that the optimization search space was considerably large and slowed the solver's performance. To limit the search space, an auxiliary constraint is added, implying that once the GFM IBR return to the normal operation mode, it does not re-enter the current saturation mode in its transient trajectory, i.e.,

$$n(k) \leq n(k+1). \tag{5.26}$$

The computation delay of the optimization is assumed to be less than a time step length. The MPC is initialized with the value of APC angle and corrective signals, which are noted as $\delta(0)$, $\Delta\delta_c(0)$ and $\Delta P_{\text{ref}}(0)$. The optimal value of $\Delta\delta_c(1)$ and $\Delta P_{\text{ref}}(1)$ are fed as the corrective signals to the APC after a time step. This process continues in a rolling manner if the detected adverse situation persists.

To summarize, this optimization minimizes the objective function 5.14 with the decision variables of $\mathcal{D} = \{\delta(k), \omega(k), \Delta\delta_c(k), \Delta P_{\text{ref}}, P(k), n(k) \mid k \in \{0, 1, \ldots, T/T_d - 1\}\}$. This optimization is subjected to $17N - 1$ constraints, including the initialization constraints, where N is the number of time steps.

5.3 Stability Boundary of a GFM IBR equipped with the Proposed MPC

The MPC proposed in the previous section enhances the chance of converging into SEP through a safe post-fault trajectory. Intuitively, the chance of convergence into SEP is increased by minimizing the deviation of the APC angle from the angle of SEP. In addition, the containment of the post-fault trajectory in a safe region is established by adding the constraints subset $\mathcal{G}_2$, which includes limiting APC angle below $\delta_{\text{zc}}^{\text{sat}}$ to prevent the GFM IBR from absorbing power from the grid. In this section, an estimation of the DOA expansion rooted in the proposed MPC is presented. Even though computing the exact DOA for the optimal control law of this mixed-integer nonlinear program is complex, a conservative estimation can be derived by computing the DOA of a feasible solution. Since the result of the optimal solution outperforms all feasible solutions in the sense of proximity to the angle of SEP (the objective function), the DOA of the proposed MPC contains the DOA of this specific feasible solution. The control law (CL_0) asserted in (5.27) is a feasible solution of the proposed MPC if constraints (5.21), (5.22), and (5.26) are neglected. These constraints either depend on the operator's preference or they are introduced to limit the optimization search space.

$$\Delta P_{\text{ref}}(k) = \begin{cases} -\Delta P_{\text{ref}}^{\max} & \text{if } n(k) = 0, \\ 0 & \text{if } n(k) = 1, \end{cases}$$
$$\Delta\delta_c(k) = 0, \quad \forall k \tag{5.27}$$

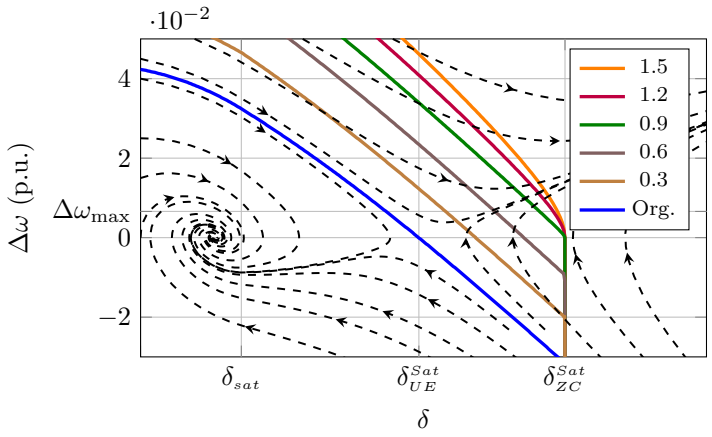


FIGURE 5.3: The numerically calculated boundary of DOA if the CL_0 is implemented for different values of maximum corrective active power reference change. Black dashed lines are post-fault trajectories in the absence of any corrective control in case of connection to a grid with $X = 0.46$ p.u.

The control law CL_0 neglects the opportunity of introducing a corrective phase jump to the grid. On the other hand, it increases the deceleration by introducing the maximum corrective active power reference change. Figure 5.3 shows the numerically calculated DOA for a GFM IBR equipped with CL_0 corrective control law in adverse situations. This DOA is, indeed, a conservative estimation of the DOA of a GFM IBR equipped with the MPC-fed corrective control. This figure shows that the maximum stable post-fault angle (critical clearing angle) is increased up to $\delta_{\text{zc}}^{\text{sat}}$ if the frequency is bounded to a small value and $\Delta P_{\text{ref}}^{\max}$ is sufficiently large. Increasing the critical clearing angle more than $\delta_{\text{zc}}^{\text{sat}}$ is not required because the GFM IBR absorbs active power from the grid for larger angles. Therefore, CL_0 sufficiently increases the transient stability DOA. Hence, the proposed MPC also increases the DOA up to the desired amount of enhancement.

5.4 Results and Discussions

This section examines the effectiveness of the proposed MPC for enhancing the transient stability of GFM IBRs. For this purpose, EMT simulations of the transient behaviour of the system of Figure 5.2 with the parameters of Table 5.1 have been conducted in Simulink/MATLAB environment [90]. The mixed-integer non-linear optimization is solved using the Artelys Knitro solver. The proposed method is compared with benchmarks. The MPC optimization's time step is 20 ms. The simulated system models a farm of parallel identical GFM IBRs. They are modelled as an equivalent GFM IBR [3].

Two scenarios of connection to strong and weak grids have been simulated to examine the transient stability enhancement offered by the proposed MPC. The grid Thevenin impedance is $Z_g = 0.3$ p.u. and $Z_g = 0.9$ p.u. for the former and latter scenarios, respectively. The proposed MPC is compared with the original control and two benchmarks. These two benchmarks are the frequency bounding approach (Strategy B) and compensating the difference between saturated and unsaturated active power output (Strategy C), which are explained in Section 5.1. After the detailed analyses of two cases of connection to weak and strong grids, robustness and sensitivity analyses are performed.

5.4.1 Tests Under the Strong Grid Condition

The simulated disturbance is a three-phase fault which occurs at $t_0 = 0.1$ s and lasts for 450 ms. It is modelled as the grid Thevenin voltage drop of 0.95 [p.u.]. This disturbance results in an increase in the APC angle from 0.407 Rad to 1.574 Rad, as shown in Figure 5.4. In the case of the original control, for which no corrective measure has been implemented, the APC angle surpasses the stability boundary. Even though the compensating control strategy (C) decreases the acceleration, this decrease in acceleration is not enough. Consequently, the GFM IBR still becomes unstable during this long fault because the APC angle surpasses the angle of the unstable equilibrium point. This is because the difference between on-fault saturated and unsaturated power is insignificant.

Param.	*Value*	*Unit*	*Description*
S_b	310	MVA	Nominal apparent power
P_0	270	MW	Reference active power
Q_0	20	MVAr	Reference reactive power
V_b	400	V	Nominal Voltage
V_{dc}	1200	V	DC link voltage
n	816	-	Number of parallel GFM IBRs
f_n	60	Hz	Nominal frequency
D_p	0.03	p.u.	Active droop coefficient
H	2	p.u.	Virtual inertia
D_q	0.1	p.u.	Reactive droop coefficient
V_0	1.01	p.u.	Set-point voltage of RPC
$I_s^{\max}$	1.2	p.u.	Maximum allowed current
β	$-\frac{\pi}{4}$	Rad	Angle of the saturated current
X_{tr}	0.16	p.u.	Total reactance of transformer windings

TABLE 5.1: Parameters describing the simulated GFM IBR farm.

Bounding the frequency (Strategy B) to the maximum of 1.0066 p.u. considerably helps to limit the acceleration and APC angle increment rate. However, The GFM IBR becomes unstable because of the insufficient post-fault deceleration. The post-fault APC angle passes the angle of the unstable equilibrium point shortly after clearing the fault, which is demonstrated as the transition from the light yellow area to the full yellow area in Figure 5.4. In this figure, colours represent the ranges of angles for which the GFM IBR exhibit particular post-fault characteristics. More specifically, each colour-coding expresses:

- Green: The set of the APC angles for which the grid-forming IBR (a) operates in its normal operation mode and (b) it injects active power into the grid.
- Light yellow: The set of the APC angles for which (a) the grid-forming IBR operates in the current-saturation operation mode, and (b) the APC angle is smaller than the angle of the unstable equilibrium point.

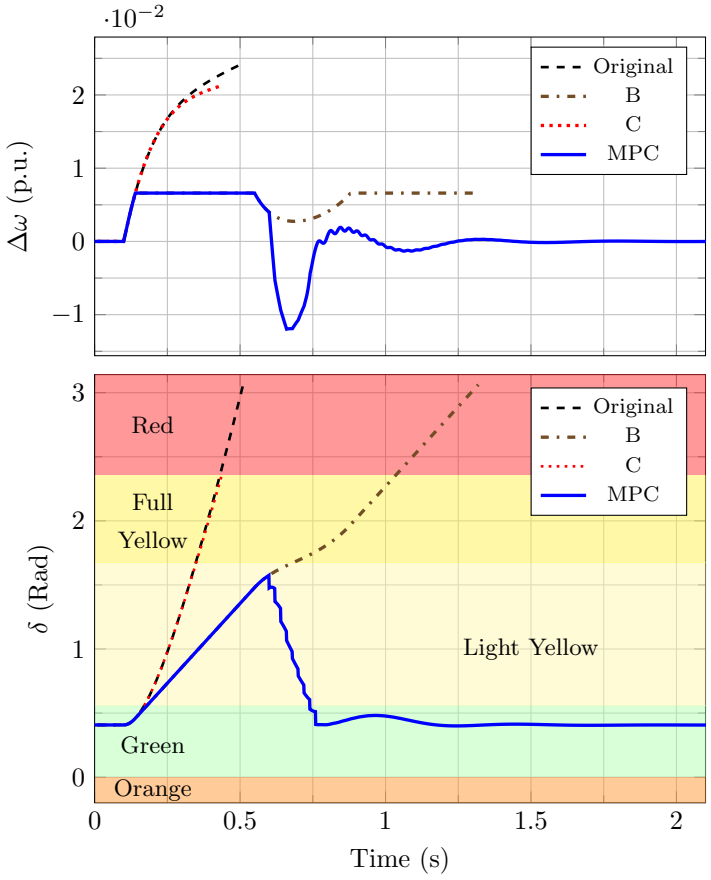


FIGURE 5.4: APC angle and frequency transient for different control strategies in the case of connection to the strong grid ($Z_g = 0.3$ p.u.).

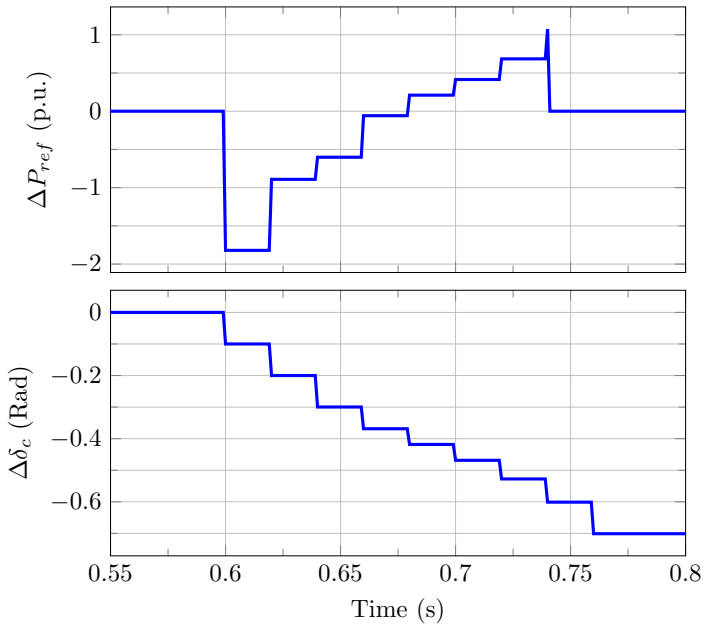


FIGURE 5.5: The optimal values for the corrective control law for the scenario where the GFM IBR is connected to the strong grid.

- Full yellow: the set of the APC angles which are (a) greater than the unstable equilibrium point. The GFM IBR becomes unstable in the absence of appropriate corrective actions.(b) However, there is a chance of returning to the normal operation mode through an appropriate corrective control.

- Red: the set of the APC angles for which (a) the active power output becomes negative, and (b) the GFM IBR operates in the current saturation mode. In this situation, the GFM IBR absorbs power from the grid, which is undesired. Even though it might be theoretically possible to make the GFM IBR stable through some corrective control measures, operating in this area is not safe. Therefore, it is not considered stable.

- Orange: the set of the negative APC angles for which (a) the GFM IBR is in the normal operation mode, and (b) the grid-forming converter absorbs power from the grid. Operating at this set of angles is not desired; however, a very brief entrance and then returning to the green area is acceptable.

Figure 5.4 shows that if the proposed MPC is implemented, the GFM IBR returns to the normal operation mode, and then the APC angle converges to SEP. The corrective signals, i.e. corrective power reference change and corrective phase jump, are shown in Figure 5.5. The corrective phase jump signal is utilized for the purpose of a fast return to the SEP.

On the other hand, the corrective power reference change damps the frequency deviations from the reference frequency. The negative optimal value of the corrective phase jump in Figure 5.5 brings the APC angle back to the green area. Meanwhile, the optimal value of the corrective power reference change is negative right after the fault to provide an extra deceleration. After a few moments, the corrective power reference change becomes positive to prevent an under-frequency below the value indicated as a constraint of the MPC.

5.4.1.1 Tests Under the Weak Grid Condition

The transient APC angle and frequency of a GFM IBR connected to the weak grid are shown in Figure 5.6. The GFM IBR is exposed to a three-phase short-circuit fault lasting for 250 ms. This fault does not cause the GFM IBR to enter the current-saturation mode. This is because the saturation threshold angle is higher for weak grids, according to Figure 3.7. As a result, the fault-on trajectory for strategy C remains the same as

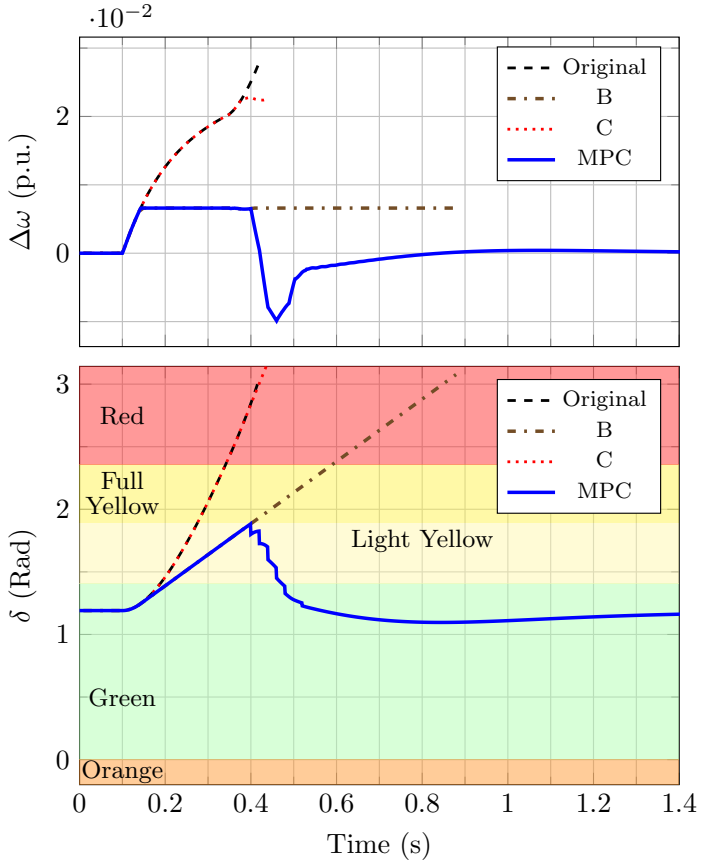


FIGURE 5.6: APC angle and frequency transient for different control strategies in the case of connection to the weak grid ($Z_g = 0.9$ p.u.).

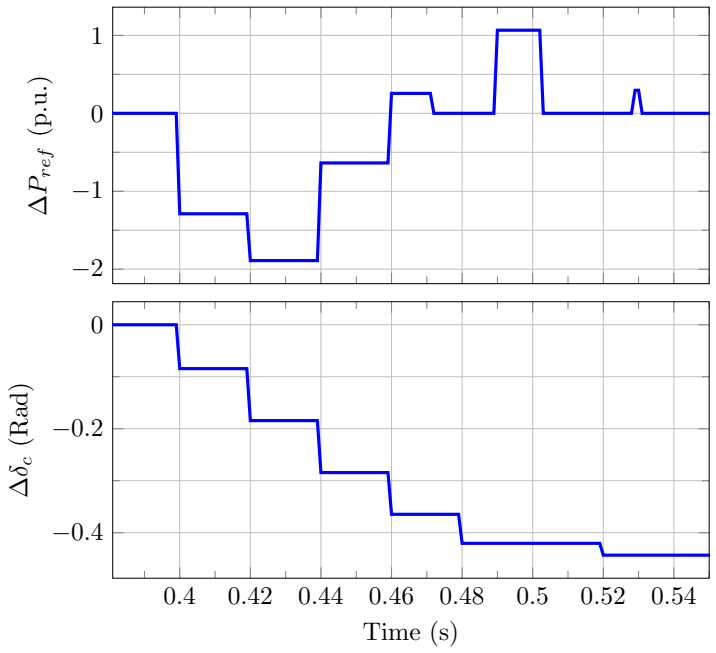


FIGURE 5.7: The optimal values for the corrective control law for the weak grid-connected GFM simulation.

the original control. Upon the fault clearance, the GFM IBR transitions to the current-saturation mode. Since the GFM IBR enters the red area before the fault clearance, strategy C is not sufficient for stabilizing the GFM IBR.

Strategy B bounds the frequency increase, which reduces the acceleration as a consequence. However, the post-disturbance deceleration is not sufficient. Therefore, strategy B is not enough to bring the APC angle to the SEP. As a result, the system transitions from the light yellow to the full yellow area and becomes unstable, as depicted in Figure 5.6. On the other hand, the proposed MPC is capable of providing extra deceleration through the corrective phase jumps and power reference change shown in Figure 5.7 to make the GFM IBR asymptotically stable, converging to the SEP, as depicted in Figure 5.6. These two scenarios provided insights into how the proposed MPC enhance transient stability. More cases are analyzed in the following subsections to ensure the proposed method enhances transient stability under different scenarios.

5.4.2 Sensitivity Analyses

This section studies several more cases to investigate further the proposed method's capabilities for enhancing the transient stability of GFM IBRs. These cases compromise the

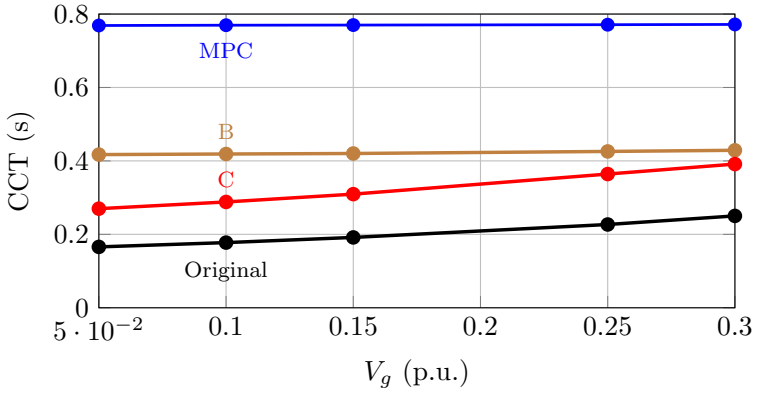


FIGURE 5.8: Variations of the CCT with the Thevenin's voltage for a GFM IBR connected to a strong grid ($Z_g = 0.3$ p.u.)

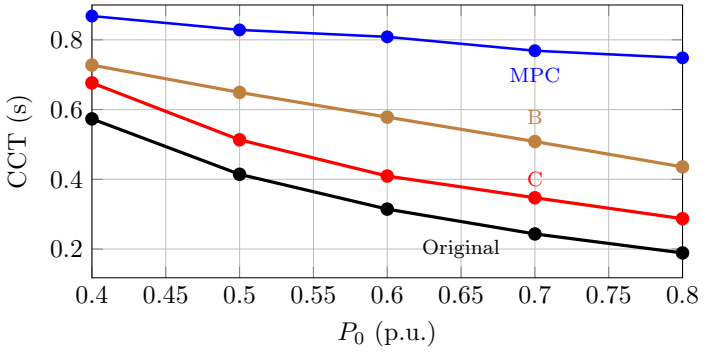


FIGURE 5.9: Variation of the CCT with the active power reference for a GFM IBR connected to a grid with $Z_g = 0.4$ p.u.

sensitivity analyses to the changes in active power reference and the fault-on Thevenin voltage, which represents the electrical proximity of the fault location to the GFM IBR.

Figure 5.8 depicts that the critical clearing time (CCT) considerably increases if the MPC is implemented. The CCT in the case of the MPC strategy implementation is around 770 ms. This is roughly the fault duration in which the APC angle increases from its initial value of 0.407 Rad to $\delta_{zc}^{sat} = 2.36$ Rad with the bounded frequency of 1.0066 p.u. The other sensitivity analyses were performed against the variations in active power reference. The active power changes from 0.4 [p.u.] to 0.8 [p.u.]. Since the IBR is operating in the grid-forming mode, its output power is derated. Therefore, the case of 1 [p.u.] active power reference is not simulated. The results demonstrated in Figure 5.9 indicate the enhancement brought by the MPC for different loading levels (active power references). These two sensitivity analyses imply that the proposed MPC outperformed the simulated benchmarks.

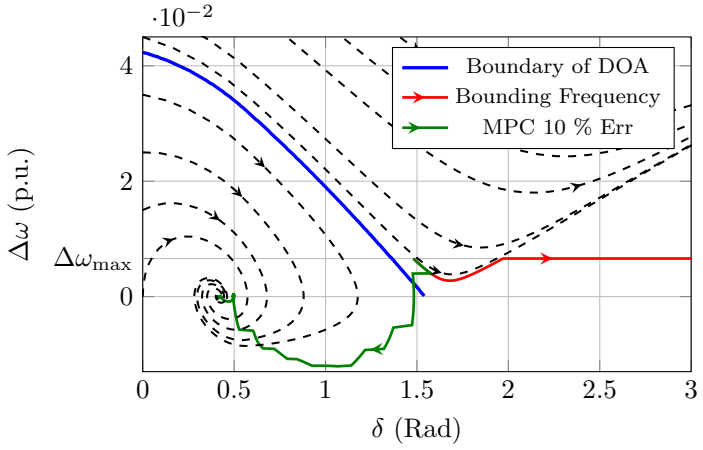


FIGURE 5.10: Post-fault APC angles for the proposed MPC with 10 % of impedance error.

5.4.3 Robustness to Parameter Estimation Error

All inputs of the MPC method proposed in this Chapter are measurements or the control parameters of the GFM IBR, except for the grid impedance value, which is estimated. In this section, the robustness of the proposed MPC method to the grid impedance estimation error is studied. The studied case includes the GFM IBR of Subsection 5.4.1 with 10 % of the impedance estimation error to a value more than its actual value. The voltage reference is also kept constant instead of following a voltage reference generated by RPC. Figure 5.10 depicts a stable APC angle trajectory despite the 10 % error in estimated grid impedance, which is considered a significant deviation.

5.5 Chapter Summary

In this chapter, two extra corrective signals are proposed to be added to the APC in order to modify the post-fault trajectory of GFM IBRs. These two corrective signals, which are

Chapter 6

Conclusions and Future Work

Deploying GFM IBRs in power grids is a promising solution for the emerging stability needs in IBR-dominant power systems. GFM IBRs follow a software-defined dynamics behaviour facing grid disturbances. This behaviour is is constrained by the current limitations. This thesis aims at modelling and enhancing the transient stability of GFM IBRs equipped with the constant angle current reference saturation. To realize this aim, the situations at which the GFM IBR transitions between the normal operation mode and current-saturation operation mode are investigated. Then, the impact of the current limitation on the transient stability is analysed. At this stage, the challenges associated with the current saturation are identified. This is followed by proposing methods to mitigate/compensate for these challenges. The detailed conclusions are listed in the following subsection.

6.1 Conclusions

1. The conditions at which a GFM IBR enters the current saturation mode are a function of the grid Thevenin voltage, grid strength and the APC angle, i.e., the angle between the local reference frame and the grid's Thevenin voltage angle. In addition to these parameters, details of the implemented current limitation mechanism play an important role in determining the necessary conditions for returning to the normal operation mode.

2. The conditions mentioned in the previous item can be expressed as two sets of APC angles, which are named the set of entering angles and the set of returning angles in this thesis. The former is independent of how the current limitation is implemented.

Nevertheless, the latter highly depends on the structure of the implemented current saturation method. More specifically, the set of returning angles is expressed as a function of the angle of the saturated current.

3. Details of the voltage control loop anti-windup algorithm design highly affect the set of returning angles. For example, A large maximum value for the PI controller in the voltage control loop shrinks the set of returning angles if the angle of the saturated current is around 45 degrees.

4. The complex transient stability behaviour of GFM IBRs cannot be simplified to the swing equation analyses. It is highly dependent on the set of entering angles and returning angles. Therefore, parameters that affect these two sets, including the angle of the saturated current and the maximum value for the PI controller in the voltage control loop, also affect the transient stability.

5. Not only is the transient stability of GFM IBRs compromised by current limitation due to the decreased post-fault deceleration, but also the introduction of the saturated stable equilibrium point imposes a new challenge to the transient stability. A wrong selection of the angle of the saturated current increases the risk of converging into satSEP.

6. The circumstances for the convergence to the satSEP are explored in this thesis. It has been demonstrated that two circumstances cause the convergence to satSEP: (1) Inclusion of the satSEP inside the set of entering angles causes the GFM IBR to converge to the satSEP if the DOA of the satSEP includes the post-fault angle (Circumstance $\mathcal{C}_1$), (2) The satSEP is outside of both sets of entering and returning angles, and the GFM IBR does not return to the normal operation mode after the fault clearance (Circumstance $\mathcal{C}_2$).

7. If the angle of the saturated current is poorly tuned, the faster fault clearance might result in a less desired consequence compared to a longer fault clearing time for a light loading operation. Therefore, the selection of the angle of the saturated current is crucial.

8. The angle of the saturated current might be tuned in a way that the angle of the satSEP is located inside the set of returning angles and outside the set of entering angles. There might be multiple angles for which this condition holds. Therefore, the selection of the exact angle can be co-optimized with minimizing the power oscillations induced by voltage error upon returning to the normal operation mode. An optimization for this purpose is formulated in this thesis. Since the angle of

the satSEP is a function of the active power reference, this optimization shall be re-performed when the active power reference changes.

9. The reduced deceleration is compensated by exploiting the fact that the dynamics of the GFM IBR are software-defined. For this purpose, two corrective signals, which are optimized through a model predictive control (MPC), are added to the APC. Extra constraints are incorporated into the MPC to ensure a safe post-fault trajectory.

10. The proposed MPC enhances the transient stability significantly. This hypothesis has been tested for multiple scenarios, and sensitivity analyses are performed for variations in the active power reference and the fault-on grid Thevenin voltage, representing the electrical proximity of the fault location.

6.2 Future Work

In this section, suggestions for future work to complete the contributions of this paper are provided. These suggestions are listed below:

- Even though the concepts of circumstances $\mathcal{C}_1$ and $\mathcal{C}_2$ for convergence to the satSEP are introduced in this thesis, the exact analytical method for calculating the sets of state variables for which these two circumstances happen is not derived. In order to derive this set, the differential equation of the dynamic conditions $\mathcal{C}_{12}$, $\mathcal{C}_{22}$, and $\mathcal{C}_{23}$, introduced in Chapter 3, should be solved in future work. The reason this thesis does not solve these equations is that it is proposed to avoid $\mathcal{C}_1$ and $\mathcal{C}_2$ through dismissing the static conditions $\mathcal{C}_{11}$ and $\mathcal{C}_{21}$ through the methodology of Chapter 4. Nevertheless, if these two conditions are inevitable for some specific scenarios, the exact calculation of the circumstances $\mathcal{C}_1$ and $\mathcal{C}_2$ is illustrative.

- The proposed methodology was specified for the constant angle current reference saturation as the implemented current limitation mechanism. Nevertheless, this methodology can be adapted for other types of current limitation mechanisms with some modifications.

- The effect of the proposed methodologies on the correct function of the protection system should be investigated. The voltage and current at the terminal of the GFM IBR are direct functions of the angle of the saturated current in addition to other

affecting parameters. Therefore, the protection implications from the angle of the saturated current optimization proposed in Chapter 4 are suggested to be analysed.

- Interactions between GFM IBRs and GFL IBRs might cause deviations in the large-signal response from the calculations conducted in this thesis. Therefore, extending the study to the interaction of multiple grid-forming and grid-following IBRs located in different locations is also suggested for future research.

Bibliography

[1] Amirnaser Yazdani and Reza Iravani. *Voltage-sourced converters in power systems: modeling, control, and applications*. John Wiley & Sons, 2010.

[2] Meng Chen, Dao Zhou, and Frede Blaabjerg. Enhanced transient angle stability control of grid-forming converter based on virtual synchronous generator. *IEEE Transactions on Industrial Electronics*, 69(9):9133–9144, 2021.

[3] Ali Tayyebi, Dominic Groß, Adolfo Anta, Friederich Kupzog, and Florian Dörfler. Frequency stability of synchronous machines and grid-forming power converters. *IEEE Journal of Emerging and Selected Topics in Power Electronics*, 8(2):1004–1018, 2020.

[4] Cheng Luo, Xikui Ma, Teng Liu, and Xiongfei Wang. Controller-saturation-based transient stability enhancement for grid-forming inverters. *IEEE Transactions on Power Electronics*, 38(2):2646–2657, 2022.

[5] Net zero strategy: Build back greener, october 2021. isbn 978-1-5286-2938-6.

[6] F. M. DArcangelo P. Lenain. A. Barker, H. Blake. Towards net zero emissions in denmark, oecd economics department working papers, no. 1705, oecd publishing, paris, 2022. URL `https://doi.org/10.1787/5b40df8f-en`.

[7] National low-carbon strategy (snbc), 2018. URL `https://www.ecologie.gouv.fr/politiques-publiques/strategie-nationale-bas-carbone-snbc`.

[8] Climate action plan 2050, principles and goals of the german government's climate policy, 2016. URL `https://www.bmuv.de/en/publication/climate-action-plan-2050-en`.

[9] National climate agreement, 2019. URL `https://www.klimaatakkoord.nl/documenten/publicaties/2019/06/28/national-climate-agreement-the-netherlands`.

[10] Dayan B Rathnayake, Milad Akrami, Chitaranjan Phurailatpam, Si Phu Me, Sajjad Hadavi, Gamini Jayasinghe, Sasan Zabihi, and Behrooz Bahrani. Grid forming inverter modeling, control, and applications. *IEEE Access*, 9:114781–114807, 2021.

[11] Nikos Hatziargyriou, JV Milanovic, Claudia Rahmann, Venkataramana Ajjarapu, Claudio Canizares, Istvan Erlich, David Hill, Ian Hiskens, Innocent Kamwa, Bikash Pal, et al. Definition and classification of power system stability revisited & extended. *IEEE Transactions on Power Systems*, 2020.

[12] Prabha Kundur, Neal J Balu, and Mark G Lauby. *Power system stability and control*, volume 7. McGraw-hill New York, United States, 1994.

[13] Yusheng Xue, Thierry Van Custem, and Mania Ribbens-Pavella. Extended equal area criterion justifications, generalizations, applications. *IEEE Transactions on Power Systems*, 4(1):44–52, 1989.

[14] Zhongtuo Shi, Wei Yao, Zhouping Li, Lingkang Zeng, Yifan Zhao, Runfeng Zhang, Yong Tang, and Jinyu Wen. Artificial intelligence techniques for stability analysis and control in smart grids: Methodologies, applications, challenges and future directions. *Applied Energy*, 278:115733, 2020.

[15] MM Adibi, PM Hirsch, and JA Jordan. Solution methods for transient and dynamic stability. *Proceedings of the IEEE*, 62(7):951–958, 1974.

[16] Qifan Chen, Nan Lin, Siqi Bu, Huaiyuan Wang, and Baohui Zhang. Interpretable time-adaptive transient stability assessment based on dual-stage attention mechanism. *IEEE Transactions on Power Systems*, 2022.

[17] Thanh Long Vu and Konstantin Turitsyn. Lyapunov functions family approach to transient stability assessment. *IEEE Transactions on Power Systems*, 31(2):1269–1277, 2015.

[18] Zitian Qiu, Chao Duan, Wei Yao, Pingliang Zeng, and Lin Jiang. Adaptive lyapunov function method for power system transient stability analysis. *IEEE Transactions on Power Systems*, 38(4):3331–3344, 2022.

[19] Peng Yang, Feng Liu, Wei Wei, and Zhaojian Wang. Approaching the transient stability boundary of a power system: Theory and applications. *IEEE Transactions on Automation Science and Engineering*, 20(4):2268–2279, 2022.

[20] Jianli Gao, Balarko Chaudhuri, and Alessandro Astolfi. A direct bounded control method for transient stability assessment. *IFAC-PapersOnLine*, 54(19):294–301, 2021.

[21] Zihao Xie, Zhaobin Du, Weixian Zhou, and Wenqian Zhang. A lyapunov approach based on gravitational search algorithm for transient stability assessment of ac/dc systems with wind power. *IET Generation, Transmission & Distribution*, 17(12): 2739–2756, 2023.

[22] Qiaomu Zhu, Jinfu Chen, Lin Zhu, Dongyuan Shi, Xiang Bai, Xianzhong Duan, and Yilu Liu. A deep end-to-end model for transient stability assessment with pmu data. *IEEE Access*, 6:65474–65487, 2018.

[23] Yunjie Gu and Timothy C Green. Power system stability with a high penetration of inverter-based resources. *Proceedings of the IEEE*, 111(7):832–853, 2022.

[24] Jintao Lei, Xin Xiang, Boxin Liu, Wuhua Li, and Xiangning He. Quantitative and intuitive vsg transient analysis with the concept of damping area approximation. *IEEE Transactions on Smart Grid*, 14(3):2477–2480, 2023.

[25] Xikun Fu, Jianjun Sun, Meng Huang, Zhen Tian, Han Yan, Herbert Ho-Ching Iu, Pan Hu, and Xiaoming Zha. Large-signal stability of grid-forming and grid-following controls in voltage source converter: A comparative study. *IEEE Transactions on Power Electronics*, 36(7):7832–7840, 2020.

[26] Feng Zhao, Zhikang Shuai, Wen Huang, Yang Shen, Z John Shen, and Chao Shen. A unified model of voltage-controlled inverter for transient angle stability analysis. *IEEE Transactions on Power Delivery*, 37(3):2275–2288, 2021.

[27] Jintao Lei, Xin Xiang, Wuhua Li, and Xiangning He. The analysis and calculation of power angle dynamics in grid forming converter under large disturbances based on kbm asymptotic method. *Ieee Transactions on Power Electronics*, 38(2):1494–1508, 2022.

[28] Xiuqiang He, Linbin Huang, Irina Subotić, Verena Häberle, and Florian Dörfler. Quantitative stability conditions for grid-forming converters with complex droop control. *IEEE Transactions on Power Electronics*, 2024.

[29] Jintao Lei, Xin Xiang, Boxin Liu, Wuhua Li, and Xiangning He. Transient stability analysis of grid forming converters based on damping energy visualization and geometry approximation. *IEEE Transactions on Industrial Electronics*, 71(3):2510–2521, 2023.

[30] Nazila Rajaei, Deepak Ramasubramanian, Jin Ma, and Behrooz Bahrani. Gpst topic 1: Advanced inverter applications (and requirements) for current-limited grid-forming inverters. 2023.

[31] Kanakesh Vatta Kkuni and Guangya Yang. Effects of current limit for grid forming converters on transient stability: analysis and solution. *International Journal of Electrical Power & Energy Systems*, 158:109919, 2024.

[32] Bo Fan, Teng Liu, Fangzhou Zhao, Heng Wu, and Xiongfei Wang. A review of current-limiting control of grid-forming inverters under symmetrical disturbances. *IEEE Open Journal of Power Electronics*, 3:955–969, 2022.

[33] Taoufik Qoria, François Gruson, Fréderic Colas, Xavier Kestelyn, and Xavier Guillaud. Current limiting algorithms and transient stability analysis of grid-forming vscs. *Electric Power Systems Research*, 189:106726, 2020.

[34] Siam Hasan Khan, Markel Zubiaga Lazkano, Pedro Izurza, Alain Sanchez-Ruiz, Javier Cañas Aceña, and Joseba Arza. Synchronization stability of a grid forming converter under the effect of current limit in voltage dips with vi based current limiting method: Analysis and solution. In *2022 24th European Conference on Power Electronics and Applications (EPE'22 ECCE Europe)*, pages P–1. IEEE, 2022.

[35] Taoufik Qoria, Francois Gruson, Frederic Colas, Guillaume Denis, Thibault Prevost, and Xavier Guillaud. Critical clearing time determination and enhancement of grid-forming converters embedding virtual impedance as current limitation algorithm. *IEEE Journal of Emerging and Selected Topics in Power Electronics*, 8(2): 1050–1061, 2019.

[36] Xiaoling Xiong, Chao Wu, and Frede Blaabjerg. Effects of virtual resistance on transient stability of virtual synchronous generators under grid voltage sag. *IEEE Transactions on Industrial Electronics*, 69(5):4754–4764, 2021.

[37] Yu Zhang, Chen Zhang, Renxin Yang, Marta Molinas, and Xu Cai. Current-constrained power-angle characterization method for transient stability analysis of grid-forming voltage source converters. *IEEE Transactions on Energy Conversion*, 38 (2):1338–1349, 2023.

[38] Bo Fan and Xiongfei Wang. Impact of circular current limiters on transient stability of grid-forming converters. In *2022 International Power Electronics Conference (IPEC-Himeji 2022-ECCE Asia)*, pages 429–434. IEEE, 2022.

[39] Xue Lyu, Wei Du, Sheik Mohammad Mohiuddin, Sai Pushpak Nandanoori, and Marcelo Elizondo. Improved transient stability analysis of multi-loop droop-controlled grid forming inverters with current limiter. In *2024 IEEE Power & Energy Society Innovative Smart Grid Technologies Conference (ISGT)*, pages 1–5. IEEE, 2024.

[40] Amro Quedan, Wenzong Wang, Deepak Ramasubramanian, Evangelos Farantatos, and Sohrab Asgarpoor. Dynamic behavior of combined 100% ibr transmission and distribution networks with grid-forming and grid-following inverters. In *2023 IEEE Power & Energy Society Innovative Smart Grid Technologies Conference (ISGT)*, pages 1–5. IEEE, 2023.

[41] Taoufik Qoria, Ebrahim Rokrok, Antoine Bruyere, Bruno François, and Xavier Guillaud. A pll-free grid-forming control with decoupled functionalities for high-power transmission system applications. *IEEE access*, 8:197363–197378, 2020.

[42] Linbin Huang, Huanhai Xin, Zhen Wang, Leiqi Zhang, Kuayu Wu, and Jiabing Hu. Transient stability analysis and control design of droop-controlled voltage source converters considering current limitation. *IEEE Transactions on Smart Grid*, 10(1): 578–591, 2017.

[43] Guangyu Wang, Lijun Fu, Qi Hu, Chenruiyang Liu, and Yanhong Ma. Transient synchronization stability of grid-forming converter during grid fault considering transient switched operation mode. *IEEE Transactions on Sustainable Energy*, 14(3): 1504–1515, 2023.

[44] Si Phu Me, Mohammad Hasan Ravanji, Bruno Leonardi, Deepak Ramasubramanian, Jin Ma, Sasan Zabihi, and Behrooz Bahrani. Transient stability analysis of virtual synchronous generator equipped with quadrature-prioritized current limiter. *IEEE Transactions on Power Electronics*, 38(9):10547–10553, 2023.

[45] Kourosh Gharouni Saffar, Sina Driss, and Firouz Badrkhani Ajaei. Impacts of current limiting on the transient stability of the virtual synchronous generator. *IEEE Transactions on Power Electronics*, 38(2):1509–1521, 2022.

[46] Yujun Li, Jingrui Liu, Yonghui Liu, Songhao Yang, and Zhengchun Du. Transient stability analysis of virtual synchronous generator with current saturation by multiple lyapunov functions method. *IET Generation, Transmission & Distribution*, 18(5): 1014–1025, 2024.

[47] Yiyuan Lu, Yujun Li, Tongpeng Mu, Chong Shao, Jingrui Liu, Dongmei Yang, and Zhengchun Du. Segmental equal area criterion for grid forming converter with current saturation. *International Journal of Electrical Power & Energy Systems*, 159:110015, 2024.

[48] Yujun Li, Yiyuan Lu, Jialun Yang, Xiaotian Yuan, Rui Yang, Songhao Yang, Hua Ye, and Zhengchun Du. Transient stability of power synchronization loop based grid forming converter. *IEEE Transactions on Energy Conversion*, 38(4):2843–2859, 2023.

[49] Ebrahim Rokrok, Taoufik Qoria, Antoine Bruyere, Bruno Francois, and Xavier Guillaud. Transient stability assessment and enhancement of grid-forming converters embedding current reference saturation as current limiting strategy. *IEEE Transactions on Power Systems*, 37(2):1519–1531, 2021.

[50] Bo Fan and Xiongfei Wang. Fault recovery analysis of grid-forming inverters with priority-based current limiters. *IEEE Transactions on Power Systems*, 38(6):5102–5112, 2022.

[51] Yushuang Liu, Hua Geng, Meng Huang, and Xiaoming Zha. Dynamic current limiting of grid-forming converters for transient synchronization stability enhancement. *IEEE Transactions on Industry Applications*, 2023.

[52] Ju Liu, Dongjun Yang, Wei Yao, Rengcun Fang, Hongsheng Zhao, and Bo Wang. Pv-based virtual synchronous generator with variable inertia to enhance power system transient stability utilizing the energy storage system. *Protection and Control of Modern Power Systems*, 2(1):1–8, 2017.

[53] Shimiao Chen, Yao Sun, Xiaochao Hou, Hua Han, Siqi Fu, and Mei Su. Quantitative parameters design of vsg oriented to transient synchronization stability. *IEEE Transactions on Power Systems*, 2023.

[54] Pingjuan Ge, Chunming Tu, Fan Xiao, Qi Guo, and Jiayuan Gao. Design-oriented analysis and transient stability enhancement control for a virtual synchronous generator. *IEEE Transactions on Industrial Electronics*, 70(3):2675–2684, 2022.

[55] Andong Liu and Jun Liu. Improved transient stability of virtual synchronous generators for grid voltage cascading faults. *Electric Power Systems Research*, 213:108661, 2022.

[56] Kongyuan Li, Peng Cheng, Letian Wang, Xinshou Tian, Jing Ma, and Limin Jia. Improved active power control of virtual synchronous generator for enhancing transient stability. *IET Power Electronics*, 16(1):157–167, 2023.

[57] Khalid Mehmood Cheema, Ahmad H Milyani, Ahmed M El-Sherbeeny, and Mohammad A El-Meligy. Modification in active power-frequency loop of virtual synchronous generator to improve the transient stability. *International Journal of Electrical Power & Energy Systems*, 128:106668, 2021.

[58] Xiaoling Xiong, Chao Wu, Bin Hu, Donghua Pan, and Frede Blaabjerg. Transient damping method for improving the synchronization stability of virtual synchronous generators. *IEEE Transactions on Power Electronics*, 36(7):7820–7831, 2020.

[59] Xiaoling Xiong, Chao Wu, Peng Cheng, and Frede Blaabjerg. An optimal damping design of virtual synchronous generators for transient stability enhancement. *IEEE Transactions on Power Electronics*, 36(10):11026–11030, 2021.

[60] Shitao Sun, Yu Lei, Guowen Hao, Yi Lu, Jindong Liu, Zhaoxin Song, and Jie Zhang. Transient damping of virtual synchronous generator for enhancing synchronization stability during voltage dips. *CES Transactions on Electrical Machines and Systems*, 8(2):143–151, 2024.

[61] Teng Liu and Xiongfei Wang. Physical insight into hybrid-synchronization-controlled grid-forming inverters under large disturbances. *IEEE Transactions on Power Electronics*, 37(10):11475–11480, 2022.

[62] Huangqing Xiao, Hongliang He, Lidong Zhang, and Teng Liu. Adaptive grid-synchronization based grid-forming control for voltage source converters. *IEEE Transactions on Power Systems*, 2023.

[63] Zhe Li, Zhen Xie, Shang Xu, and Xing Zhang. Improving transient stability of grid-forming dfig based on enhanced hybrid synchronization control. *IEEE Transactions on Industrial Electronics*, 2024.

[64] Heng Wu and Xiongfei Wang. A mode-adaptive power-angle control method for transient stability enhancement of virtual synchronous generators. *IEEE journal of emerging and selected topics in power electronics*, 8(2):1034–1049, 2020.

[65] Wenjia Si and Jingyang Fang. Transient stability improvement of grid-forming converters through voltage amplitude regulation and reactive power injection. *IEEE Transactions on Power Electronics*, 2023.

[66] Mingxuan Li, Sirui Shu, Yue Wang, Peng Yu, Yonghui Liu, Zhenyuan Zhang, Weihao Hu, and Frede Blaabjerg. Analysis and improvement of large-disturbance stability for grid-connected vsg based on output impedance optimization. *IEEE Transactions on Power Electronics*, 37(8):9807–9826, 2022.

[67] Zheming Jin and Xiongfei Wang. A dq-frame asymmetrical virtual impedance control for enhancing transient stability of grid-forming inverters. *IEEE Transactions on Power Electronics*, 37(4):4535–4544, 2021.

[68] Zhaoyue Zou, Chao Wu, Yong Wang, Yu Lu, Qiang Zou, and Nannan Wang. Asymmetric virtual impedance for improving transient stability of grid-forming inverters based on virtual reluctance torque. In *2023 11th International Conference on Power Electronics and ECCE Asia (ICPE 2023-ECCE Asia)*, pages 1167–1172. IEEE, 2023.

[69] Yiwei Ma, Fred Wang, and Leon M Tolbert. Virtual synchronous generator with limited current–impact on system transient stability and its mitigation. In *2020 IEEE Energy Conversion Congress and Exposition (ECCE)*, pages 2773–2778. IEEE, 2020.

[70] Kun Sun, Wei Yao, Jinyu Wen, and Lin Jiang. A two-stage simultaneous control scheme for the transient angle stability of vsg considering current limitation and voltage support. *IEEE Transactions on Power Systems*, 37(3):2137–2150, 2021.

[71] Pingjuan Ge, Fan Xiao, Chunming Tu, Qi Guo, Jiayuan Gao, and Yufei Song. Comprehensive transient stability enhancement control of a vsg considering power angle stability and fault current limitation. *CSEE Journal of Power and Energy Systems*, 2022.

[72] Yang Shen, Quan Zhou, Yang Li, and Zhikang Shuai. Data-driven predictive control for grid-forming converter stability enhancement in island microgrids. In *2022 IEEE/IAS Industrial and Commercial Power System Asia (I&CPS Asia)*, pages 1292–1297. IEEE, 2022.

[73] Pengfei Sun, Zhen Tian, Meng Huang, Xiaoming Zha, Xilin Li, and Wei Wang. Additional kinetic energy injection and piecewise damping based postfault anti-windup and transient stability enhanced control for grid-forming inverter. *IEEE Transactions on Power Electronics*, 2024.

[74] Joseba Erdocia, Andoni Urtasun, and Luis Marroyo. Power angle–frequency droop control to enhance transient stability of grid-forming inverters under voltage dips. *IEEE Journal of Emerging and Selected Topics in Power Electronics*, 11(4):3751–3764, 2022.

[75] Liang Huang, Chao Wu, Dao Zhou, and Frede Blaabjerg. A power-angle-based adaptive overcurrent protection scheme for grid-forming inverter under large grid disturbances. *IEEE Transactions on Industrial Electronics*, 70(6):5927–5936, 2022.

[76] Julia Matevosyan, Jason MacDowell, B Badrzadeh, C Cheng, S Dutta, SD Rao, V Gevorgian, T Green, D Howard, D Kong, et al. Grid-forming technology in energy systems integration. *ESIG High Share of Inverter-Based Generation Task Force: Report. Available online: https://www. esig. energy/wp-content/uploads/2022/03/ESIG-GFM-report-2022. pdf (accessed on 20 June 2022)*, 2022.

[77] Balarko Chaudhuri, Deepak Ramasubramanian, Julia Matevosyan, Mark OMalley, Nick Miller, Tim Green, and Xiaoyao Zhou. Rebalancing needs and services for future grids: System needs and service provisions with increasing shares of inverter-based resources. *IEEE Power and Energy Magazine*, 22(2):30–41, 2024.

[78] Roy Billinton. *Power system reliability evaluation*. Taylor & Francis, 1970.

[79] Grid forming technology bulk power system reliability considerations. *North American Electric Reliability Corporation: Report. Available online: Available: https://www.nerc.com/comm/RSTC$_R$eliability$_G$uidelines/White$_P$aper$_G$rid$_F$orming$_T$echnology.pd*

[80] Teng Liu, Xiongfei Wang, Fangcheng Liu, Kai Xin, and Yunfeng Liu. A current limiting method for single-loop voltage-magnitude controlled grid-forming converters during symmetrical faults. *IEEE Transactions on Power Electronics*, 37(4):4751–4763, 2021.

[81] Macit Tozak, Sezai Taskin, Ibrahim Sengor, and Barry P Hayes. Modelling and control of grid forming converters: A systematic review. *IEEE Access*, 2024.

[82] Simon Eberlein and Krzysztof Rudion. Impact of inner control loops on small-signal stability and model-order reduction of grid-forming converters. *IEEE Transactions on Smart Grid*, 14(4):2812–2824, 2022.

[83] Prabha Kundur. Power system stability. *Power system stability and control*, 10:7–1, 2007.

[84] Weihua Zhou, Nabil Mohammed, and Behrooz Bahrani. Comprehensive modeling, analysis, and comparison of state-space and admittance models of pll-based grid-following inverters considering different outer control modes. *IEEE Access*, 10:30109–30146, 2022.

[85] Yitong Li, Yunjie Gu, and Timothy C Green. Revisiting grid-forming and grid-following inverters: A duality theory. *IEEE Transactions on Power Systems*, 37(6): 4541–4554, 2022.

[86] Zhangxin Zhou, Wenzong Wang, Tian Lan, and Garng M Huang. Dynamic performance evaluation of grid-following and grid-forming inverters for frequency support in low inertia transmission grids. In *2021 IEEE PES Innovative Smart Grid Technologies Europe (ISGT Europe)*, pages 01–05. IEEE, 2021.

[87] Mohammad Hasan Ravanji, Dayan B Rathnayake, Milad Zarif Mansour, and Behrooz Bahrani. Impact of voltage-loop feedforward terms on the stability of grid-forming inverters and remedial actions. *IEEE Transactions on Energy Conversion*, 38(3): 1554–1565, 2023.

[88] Shimiao Chen, Yao Sun, Hua Han, Siqi Fu, Shihan Luo, and Guangze Shi. A modified vsg control scheme with virtual resistance to enhance both small-signal stability and transient synchronization stability. *IEEE Transactions on Power Electronics*, 38(5): 6005–6014, 2023.

[89] Babak Badrzadeh, Zia Emin, and Yunjie Gu. Changing power systems and impact on power system dynamic phenomena and analysis methods. In *Power System Dynamic Modelling and Analysis in Evolving Networks*, pages 3–53. Springer, 2024.

[90] The MathWorks Inc. Matlab simulink r2021b, 2021. URL `https://www.mathworks.com`.

[91] Artelys. Artelys knitro optimization solve.

[92] Richard L Burden and J Douglas Faires. Numerical analysis, brooks, 2011.